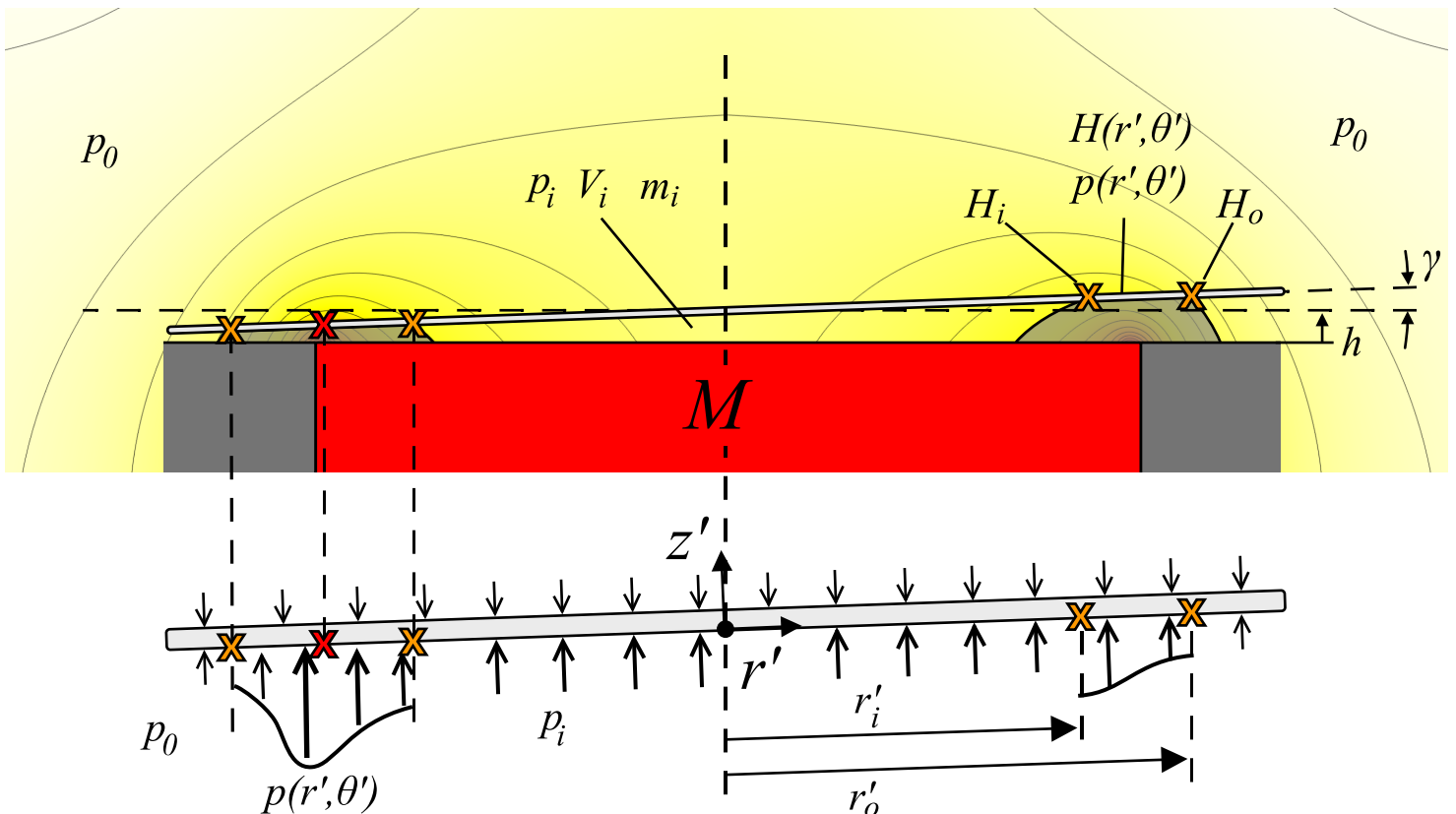# Department of Precision and Microsystems Engineering

Operational range of a ferrofluid pocket bearing

A.S.T. Boots

Report no : 2018.037
Coach : S.G.E. Lampaert
Professor : J.W. Spronck and R.A.J. van Ostayen
Specialisation : Mechatronic System Design
Type of report : Master of Science Thesis
Date : 12 November 2018

Operational range of a ferrofluid pocket bearing

by

A.S.T. Boots

to obtain the degree of Master of Science
at the Delft University of Technology,
to be defended publicly on Monday November 12, 2018 at 12:45 AM.

Student number: 4295102
Project duration: September, 2017 – November 12, 2018
Thesis committee: Dr. ir. R.A.J. van Ostayen, TU Delft
ir. J.W. Spronck, TU Delft
ir. S.G.E. Lampaert, TU Delft, supervisor
Dr. ir. J.F.L. Goosen, TU Delft
Dr. R. Delfos, TU Delft

An electronic version of this thesis is available at http://repository.tudelft.nl/.

TUDelft Delft University of Technology

TUDelft
Delft
University of
Technology

Nomenclature

List of symbols: Chapter 2

α	Tilt angle	rad
β	Size of a single partition	rad
Γ	Set of coordinates used to distinguish air and ferrofluid	-
γ	Tilt angle at angular coordinate θ	rad
μ_0	Vacuum permeability	$4\pi \times 10^{-7}\,N\,A^{-2}$
Ω	Set of coordinates that defines ferrofluid	-
Ω_1	Subset of Ω	-
Ω_2	Subset of Ω	-
$\overline{R}$	Universal gas constant	$8.314\,J\,K^{-1}\,mol^{-1}$
ϕ	Angular coordinate around y-axis	rad
ρ	Density	$kg\,m^{-3}$
θ	Angular coordinate around z-axis	rad
θ'	Angular coordinate around z'-axis (body fixed frame of reference)	rad
$\theta_{l,k}$	Lower boundary of partition k	rad
$\theta_{u,k}$	Upper boundary of partition k	rad
A_p	Surface area pocket	m^2
A_s	Surface area ferrofluid seal	m^2
F_L	Load capacity	N
F_L'	Load capacity in z'-direction	N
H	Magnetic field strength	$A\,m^{-1}$
h	Fly height	m
H_i	Magnetic field at inner interface	$A\,m^{-1}$
H_o	Magnetic field at outer interface	$A\,m^{-1}$
h_0	Height at which the plate makes initial contact with the ferrofluid	m

H_{max}	Maximum magnetic field strength	$A\,m^{-1}$
k	Index variable for the discretization	-
k_ϕ	Tilt stiffness of the bearing around y-axis	$N\,m\,rad^{-1}$
k_z	Stiffness of the bearing in z-direction	$N\,m^{-1}$
M	Magnetization	$A\,m^{-1}$
m_i	Air mass inside the pocket	kg
M_s	Saturation magnetization of ferrofluid	$A\,m^{-1}$
M_y	Torque that acts on the plate around y-axis	$N\,m$
M_{Air}	Molar mass air	$28.97\,g\,mol^{-1}$
$m_{i,0}$	Air mass inside the pocket when the plate is at h_0	kg
$m_{i,max}$	Air mass inside pocket when pressure inside is maximum	kg
$m_{i,min}$	Air mass inside pocket when pressure inside is minimum	kg
N	Number of discretizations	-
p	Pressure	Pa
p_0	Ambient pressure	$10^5\,Pa$
p_i	Pressure inside the pocket	Pa
$p_{i,max}$	Maximum pressure inside the pocket	Pa
$p_{i,min}$	Minimum pressure inside the pocket	Pa
R	Radius magnet	m
r	Radial distance	m
r'	Radial distance (body fixed frame of reference)	m
r_i	Inner radius ferrofluid seal	m
r_i'	Inner radius ferrofluid seal (body fixed frame of reference)	m
r_o	Outer radius ferrofluid seal	m
r_o'	Outer radius ferrofluid seal (body fixed frame of reference)	m
T	Temperature	K
V_{ff}	Volume of ferrofluid	m^3
V_i	Volume of the pocket	m^3
$V_{i,0}$	Volume of pocket when the plate is at h_0	m^3
$V_{i,max}$	Volume of pocket when pressure inside is maximum	m^3
$V_{i,min}$	Volume of pocket when pressure inside is minimum	m^3
x	Horizontal coordinate	m
y	Horizontal coordinate	m
z	Vertical coordinate	m
z'	Vertical coordinate (body fixed frame of reference)	m

Abstract

Ferrofluid bearings provide a cheap and passive alternative to contactless bearings, such as magnetic bearings and fluid bearings. The absence of stick-slip and the low viscous friction make them interesting for high precision applications. Despite the theoretical models available in literature, the number of design rules for ferrofluid bearings is fairly limited, making it difficult to compare ferrofluid bearings to other bearing concepts. The goal of this thesis project is to develop new design rules for ferrofluid pocket bearings and to model ferrofluid in FEM software.

This thesis presents a (FEM) model, in which the equilibrium position of the bearing is dependent on the air mass inside the pocket and the strength of the ferrofluid seal. The model was experimentally validated by measuring the force and displacement of a ferrofluid pocket bearing with the use of a tensile testing machine. Overcompression of the bearing caused air to escape out of the pocket, while overdecompression resulted in mass gain. The behaviour of the bearing was repeatable as long as the air mass inside the pocket remained unaltered. In practice, this is the operational range of the bearing and can simply be determined from the mass versus fly height diagram of te bearing.

The results of the sensitivity analysis show how various errors affect the overall performance of the ferrofluid pocket bearing. Tilt decreases the load capacity and operational range of the bearing, whereas increasing the amount of ferrofluid increases both. The sensitivity analysis also shows that ferrofluid pocket bearings are always self-aligning.

Table of Contents

Acknowledgements

First of all, I would like to thank Stefan Lampaert for his enthusiastic and inspirational guidance during my thesis project. The interesting and helpful discussions in combination with the occasional fresh look and good times really helped me the past year.

I would like to thank Jo Spronck for the in-depth discussions, the weekly meetings, including the "tegeltjeswijsheden", and for his supervision and out-of-the-box ideas.

I would like to thank Ron van Ostayen for all the helpful tips and lessons on how to model different physical phenomena, for the weekly meetings, for his supervision and for being the chairman of my exam committee.

René Delfos and Hans Goosen for being interested in my thesis project and for making time to be part of my exam committee.

The entire technical support staff of PME. Patrick van Holst and Harry Jansen for their assistance and expertise during the construction of the measurements setup. Rob Luttjeboer and Spiridon van Veldhoven for helping me with 3D printing and ordering parts for my test setup. Jos van Driel for helping me to improve my test setup by additional sensors.

All the people present during the weekly meetings of both the Thin Film Lubrication and Mechatronic System Design group.

Everyone at "the office"!

Bram and Laurens for kick-starting my thesis project by publishing a paper together, thank you guys!

Last but definitely not least, I would like to thank my parents, my sister and my friends for the good times and the support they gave me during my studies.

Delft, University of Technology   A.S.T. Boots

November 12, 2018

Chapter 1

Introduction

1-1 Background

An essential part in the development of precision positioning systems is the bearing system (Chapter I). Solid contact bearings, such as ball bearings, have a high load capacity and stiffness, but suffer from stick-slip, possible backlash, friction and wear [43]. Flexure based mechanisms are free of these disadvantages [13], but are generally limited in their range of motion [6][11]. Other bearing concepts that are free of stick slip and wear, are magnetic and fluid bearings. Fluid bearings often need sealing, whereas magnetic bearings are inherently unstable and need therefore high frequency control systems [43]. An interesting and cheap alternative might be a ferrofluid bearing. Ferrofluid bearings are free of stick-slip and do not require sealing or pumps, since the magnetic fluid is held in place by a simple permanent magnet. Two different types of ferrofluid bearings can be identified in literature, namely ferrofluid pocket bearings and ferrofluid pressure bearings [46].

Theoretical models describing the performance and behaviour of ferrofluid pocket bearings were developed recently. Lampaert et al. [23] [24] [25] developed (semi-)analytical models for calculation of the load capacity (F_L), the out-of-plane stiffness (k_z), the in-plane damping (c_{ff}) and the friction force (F_{fric}). The result was the formulation of some general design rules for ferrofluid bearings. (1) High load capacity and stiffness are obtained by decreasing the fly height of the bearing, since the magnetic field is stronger near the magnet. (2) Designing the bearing symmetrically increases the load capacity, stiffness and repeatability. (3) Ferrofluid pocket bearings have with respect to ferrofluid pressure bearings, higher load capacity and stiffness for a comparable volume of ferrofluid, due to the encapsulated and pressurized air pocket.

1-2 Project objective

Figure 1-1 presents an example of a simple design process (including the scope of this thesis project), starting from the functional requirements. The second step in the design process is to conceptualize different solutions. For example, concepts for a bearing system might be ferrofluid, magnetic and ball bearings. Next, the different concepts will be compared based on their expected performance. Generally, rules of thumb (design rules) will be used to make the initial comparison, after which the most promising concept(s) will be designed in detail. **Since the number of design rules for ferrofluid bearings is still fairly limited, comparing ferrofluid bearings to other bearing concepts remains difficult.**

A couple of interesting design variables can already be identified in literature, which subsequently may result in new design rules (Figure 1-1). It was observed that over(de)compression of ferrofluid pocket bearings decreases the mass and volume of the air pocket, but increases

the load capacity and stiffness [24]. This behaviour is not properly modelled yet. Moreover, currently there is not much literature available on modelling ferrofluid in FEM packages. **This results in the main goals of this thesis project:**

- model the behaviour of ferrofluid pocket bearings after over(de)compression and
- model ferrofluid in a finite element analysis (FEM), such that additional design rules can be formulated.
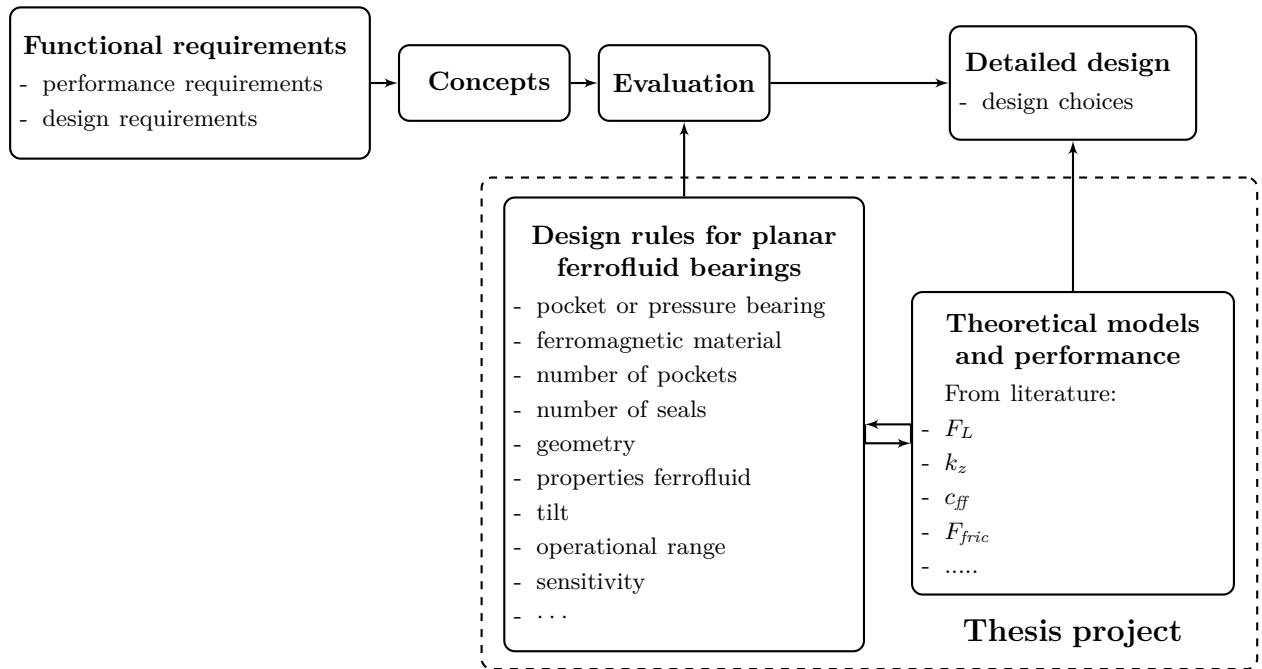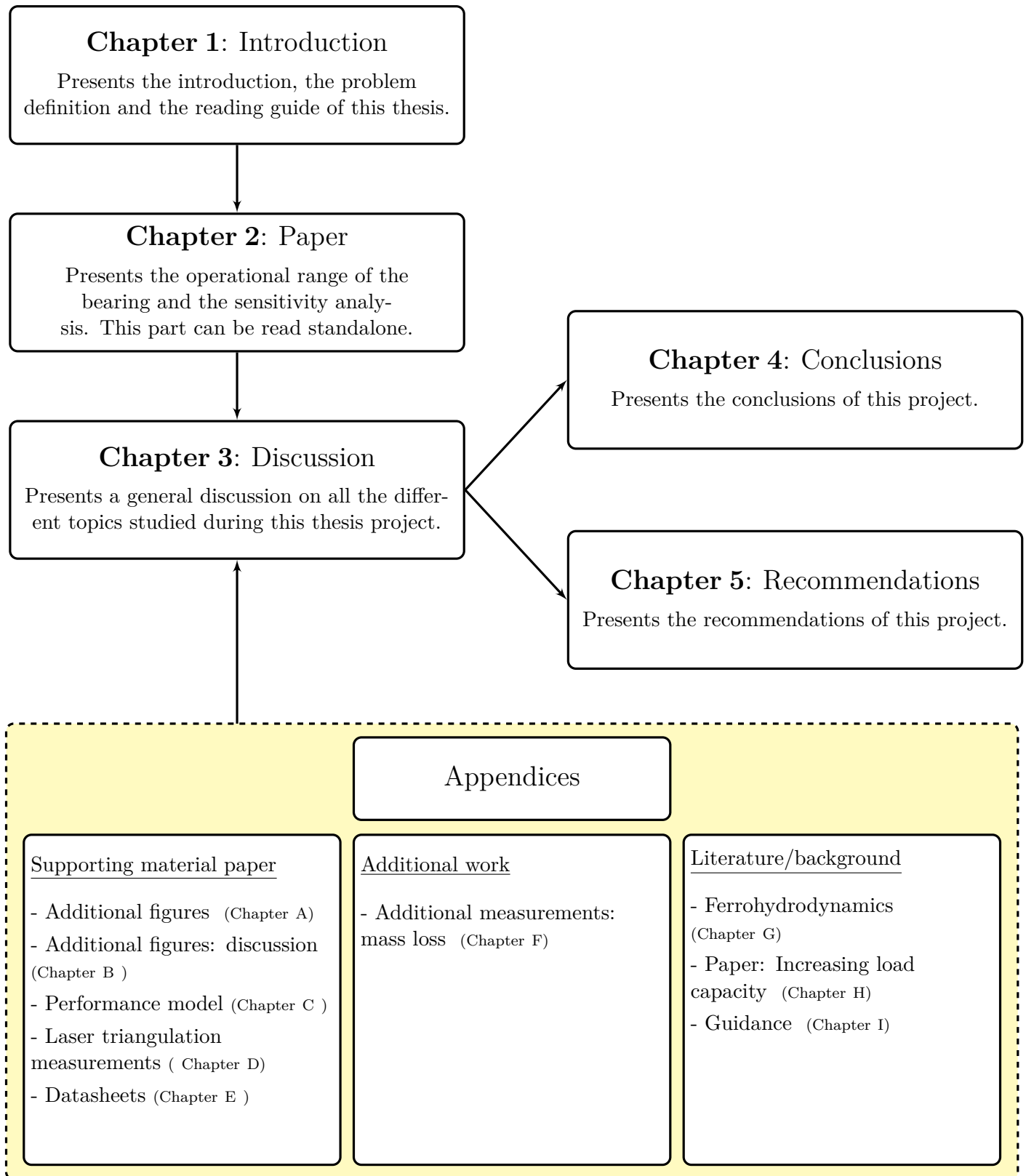

Figure 1-1: An overview of a simple design process for a bearing system.

1-3 Thesis overview

The overview presented on the next page shows how the different sections of this thesis are interconnected. Chapter 2 presents the main body of this project in a (yet to publish) paper: "Operational range of a ferrofluid pocket bearing". In this paper, the behaviour of ferrofluid pocket bearings after over(de)compression is modelled in a FEM package. The air mass inside the pocket is combined with a mathematical description for the strength of a ferrofluid seal. The paper can be read standalone. All the other work done during this project project can be found in different appendices. Additional material regarding the paper can be found in the first part of the appendices (Chapters A-E). The velocity dependency of the escaping air mass is presented in Chapter F. The equations governing the physics of magnetic fluids (Ferrohydrodynamics) are given in Chapter G. A general overview of the advantages and disadvantages of different bearing concepts is given in Chapter I. During my literature study, I had the privilege to help publishing the paper: "Increasing the load capacity of planar ferrofluid bearings by the addition of ferromagnetic material" (Chapter H). The paper formulates design rules for increasing the load capacity. All these different parts are linked together in the discussion in Chapter 3. Finally, the overall conclusions and recommendations of this thesis project are given in Chapter 4 and Chapter 5.

Chapter 1: Introduction

Presents the introduction, the problem definition and the reading guide of this thesis.

Chapter 2: Paper

Presents the operational range of the bearing and the sensitivity analysis. This part can be read standalone.

Chapter 3: Discussion

Presents a general discussion on all the different topics studied during this thesis project.

Chapter 4: Conclusions

Presents the conclusions of this project.

Chapter 5: Recommendations

Presents the recommendations of this project.

Appendices

Supporting material paper

- Additional figures (Chapter A)
- Additional figures: discussion (Chapter B)
- Performance model (Chapter C)
- Laser triangulation measurements (Chapter D)
- Datasheets (Chapter E)

Additional work

- Additional measurements: mass loss (Chapter F)

Literature/background

- Ferrohydrodynamics (Chapter G)
- Paper: Increasing load capacity (Chapter H)
- Guidance (Chapter I)

Chapter 2

Paper

Operational range of a ferrofluid pocket bearing

A.S.T. Boots, S.G.E. Lampaert, J.W. Spronck, and R.A.J van Ostayen
Department of Precision and Microsystems Engineering, Delft University of Technology, Mekelweg 2, 2628CD, Delft, The Netherlands

Ferrofluid pocket bearings are interesting for fast and precise positioning systems thank to the absence of stick-slip, the low viscous friction and their cost-effective nature. However, the characteristics of the bearing change due to over(de)compression since air escapes out of the enclosed pocket. This article presents an experimentally validated model that includes the air mass inside the pocket in the calculation of the equilibrium position of the ferrofluid bearing. Moreover, a simple and efficient way to obtain the operational range of the bearing is presented and a sensitivity analysis was performed. The sensitivity analysis showed that ferrofluid pocket bearings are always self-aligning and that the tilt stiffness increases when the fly height decreases or the tilt angle increases.

Keywords: Precision engineering, FEM modelling, mathematical modelling, hydrostatic bearing, magnetics, sensitivity analysis

I. INTRODUCTION

A ferrofluid is a colloidal suspension of small magnetic particles inside a carrier fluid. The magnetic particles $(3-15nm)$, often covered with a layer of dispersant, give the fluid paramagnetic properties[1–3].

Numerous applications have been suggested for ferrofluids over the years[4–7], ranging from sensors[8,9] and actuators[10–14] to the use of ferrofluid as a lubricant[15] or an energy harvester[16]. Another frequently suggested application is to make staged[17] and non-bursting[18] ferrofluidic seals. This enables rotary shafts to be sealed without the common disadvantage of wear[19,20], like in vacuum feedthrough[21] or aqueous environments[22]. Ferrofluid bearings and seals can be optimized by maximizing the magnetic force generated by permanent magnets using ferromagnetic material[23–25]. The absence of stick-slip also makes ferrofluid bearings useful in high precision systems[26–30].

Ferrofluid bearings can be classified as either pressure bearings or pocket bearings[31]. Ferrofluid pressure bearings only rely on the pressure inside the ferrofluid to carry a load. Pocket bearings on the other hand rely on both the pressurized air pocket, which is encapsulated by the ferrofluid seal, and the pressure inside the seal itself. The pressure is a result of the magnetic body force which depends on the external magnetic field and the boundary condition of the magnetic fluid[32,33].

Lampaert et al.[34] presented a mathematical model to calculate the maximum load capacity of ferrofluid pocket bearings. Over(de)compression of a ferrofluid pocket bearing resulted in air escaping in and out of the pocket which subsequently changed the behaviour of the bearing. However, the bearing also showed good repeatability over multiple compression-decompression cycles when the mass inside the pocket is unaltered. In practice, this is the operational range of the bearing.

In this article, the behaviour of the bearing after over(de)compression is modelled to determine its operational range. First, an experimentally validated model

is presented to calculate the position of the ferrofluid seal depending on the air mass inside the pocket. Next, this position will be used to calculate the load capacity of the ferrofluid bearing according to literature. Moreover, a simple and efficient way to obtain the operational range is presented based on only the strength of a ferrofluid seal and the mass inside the pocket. Finally, a sensitivity study was performed in order to see how different variables affect the load capacity and operational range of the bearing.
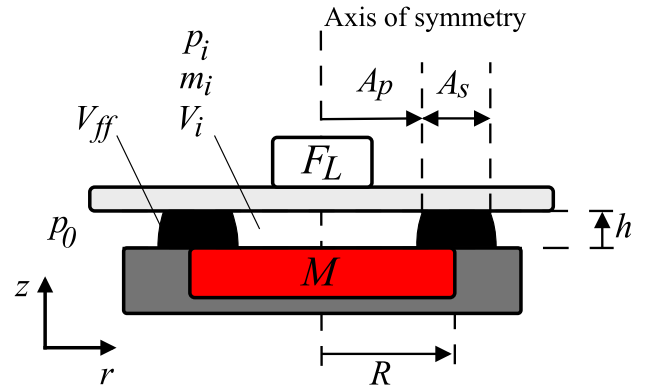

FIG. 1. A cross-section of the ferrofluid pocket bearing defines the parameters used in this article. The cylindrical magnet, with magnetization M, is placed in a non-ferromagnetic base (grey).

II. METHODS

First, the calculation of the strength of a ferrofluid seal in the presence of an external magnetic field is described. Subsequently, the load capacity of the bearing is derived and the sensitivity of the load capacity with respect to tilt is analysed. The ideal gas law is introduced to calculate the air mass enclosed by the ferrofluid seal. Next,

the Finite Element Method (FEM) model is introduced, which will be used to calculate the positions of the interfaces between ferrofluid and air. The magnitude and positions of the interfaces will subsequently be used to calculate the load capacity and torque of the bearing. The load capacity is calculated according to Lampaert et al.[34]. Finally, the experimental set-up that was used to validate the predicted load capacity of the bearing is introduced. Fig. 1 shows the schematic of the bearing including all the important parameters.

A. Mathematical model

1. Ferrofluid seal

The pressure inside a stationary ferrofluid seal can be derived from the Ferrohydrodynamic Navier-Stokes equations for incompressible Newtonian fluids[2,35]. In the derivation, it is assumed that the ferrofluid is completely saturated and that the only body force present is the magnetic body force. The result is Eq. (1) for the pressure distribution inside a ferrofluid[24,34]. In this equation, the pressure ($p(r)$) inside the ferrofluid at a specific radial position (r) and fly height (h), is dependent on the magnetic field intensity ($H(r)$) at that specific location and the magnetic field intensity of the outer fluid-air interface (H_o). Moreover, μ_0 is the permeability of vacuum and M_s the saturation magnetization of the ferrofluid.

$$p(r) - p_0 = \mu_0 M_s \left(H(r) - H_o \right) \qquad (1)$$

Eq. (1) can be used to calculate the pressure difference over a ferrofluid seal (Δp or $p_i - p_0$) by evaluating the magnetic field intensity at the inner interface (H_i) and at the outer interface (H_o), Eq. (2). Fig. 2 shows the location and shape of the ferrofluid seal for an arbitrary H_i and H_o at h. The figure also shows the resulting pressure distribution.

Next, Eq. (2) can be used to calculate the maximum pressure difference that a ferrofluid seal can withstand. The maximum pressure difference ($p_{i,max} - p_0$) is determined by the maximum difference in magnetic field intensity that can be achieved across the ferrofluid seal (ΔH or $H_i - H_o$). This maximum is obtained when the inner ferrofluid interface is located at the maximum magnetic field intensity at that specific fly height, thus when $H_i = H_{max}$. This results in Eq. (4) for the calculation of the maximum strength of the seal. Note that the value of H_{max} is dependent on the the magnetic field generated by the permanent magnet and the fly height. The value of H_o is dependent on the amount of ferrofluid present in the system (V_{ff}). Fig. 3 shows the corresponding location and shape of the seal, the pressure distribution and magnetic field intensity over the seal.

The same reasoning applies to the calculation of the minimum pocket pressure, given in Eq. (6). In that case, the magnetic field intensity at the outer interface equals
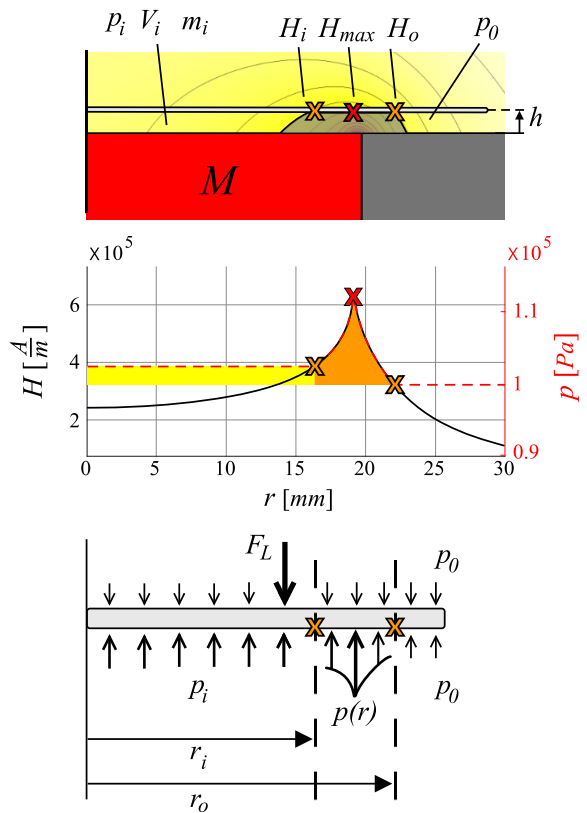

FIG. 2. The pressure distribution (middle figure), acting on the plate above the bearing (bottom figure), is a result of the shape and placement of the ferrofluid seal (top figure). The total load capacity is obtained by integrating the pressure distributions given in the bottom figure. The coloured areas in the middle figure represent visually the contributions of the seal and pocket to the total load capacity of the bearing.

$$p_i - p_0 = \mu_0 M_s \left(H_i - H_o \right) \qquad (2)$$

$$m_i = p_i V_i \frac{M_{air}}{RT} \qquad (3)$$

the maximum magnetic field intensity at that fly height ($H_o = H_{max}$). This results in a negative pressure drop over the seal, since $H_o > H_i$. Fig. 4 shows the shape of the ferrofluid seal for a minimum pressure inside the pocket and once again the pressure distribution and magnetic field for that specific configuration. Note that the pressure inside the pocket is lower than the ambient pressure. The corresponding pressure difference the seal has to withstand is referred to as the minimum strength of the ferrofluid seal.

2. Load Capacity

Integration of all the different forces that act on the plate (Fig. 2) results in the total load capacity of the
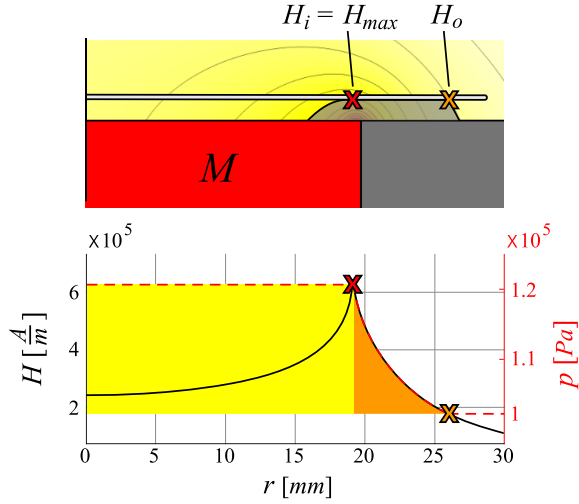
FIG. 3. The shape of the ferrofluid seal and the resulting pressure distribution over the seal for a maximum pressurized pocket at a height h. The corresponding load capacity of the seal and the pocket are indicated in orange and yellow.

$$p_{i,max} - p_0 = \mu_0 M_s \left(H_{max} - H_o \right) \tag{4}$$

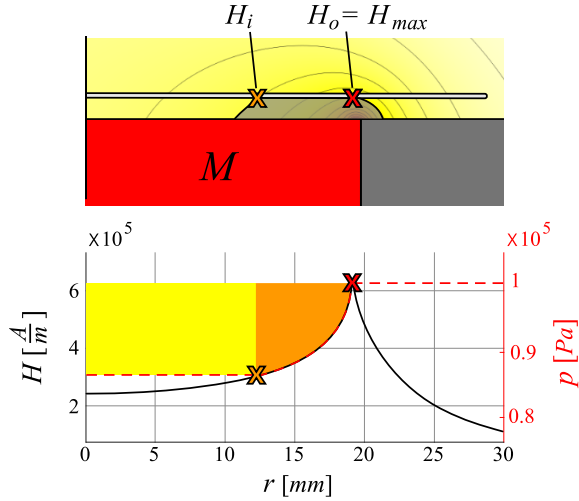$$m_{i,max} = p_{i,max} V_{i,max} \frac{M_{air}}{RT} \tag{5}$$

FIG. 4. The shape of the ferrofluid seal and the resulting pressure distribution over the seal for a minimum pressurized pocket at a height h. The corresponding load capacity of the seal and the pocket are indicated in orange and yellow.

$$p_{i,min} - p_0 = \mu_0 M_s \left(H_i - H_{max} \right) \tag{6}$$

$$m_{i,min} = p_{i,min} V_{i,min} \frac{M_{air}}{RT} \tag{7}$$

bearing (F_L), Eq. (8). Combining Eq. (2) and Eq. (8) results in Eq. (9) for the load capacity expressed in a cylindrical coordinate system. The total load capacity is made up of the contribution of the air pocket and the contribution of the ferrofluid seal. The radial position of the inner interface is denoted by r_i and the outer interface by r_o.

$$F_L = \int_0^{2\pi} \int_0^{r_o} \left(p(r) - p_0 \right) r\, dr\, d\theta \tag{8}$$

$$F_L = \underbrace{\mu_0 M_s \left(H_i - H_o \right) \pi r_i^{\,2}}_{\text{Air pocket}} + \underbrace{2\pi \mu_0 M_s \int_{r_i}^{r_o} \left(H(r) - H_o \right) r\, dr}_{\text{Ferrofluid seal}} \tag{9}$$

Fig. 2, Fig. 3 and Fig. 4 visually show how the load capacity is calculated using Eq. (8) or Eq. (9). The contribution of the pocket to the total load capacity is indicated by the yellow marked area, while that of the seal is marked orange.

The stiffness of the ferrofluid bearing can be calculated by taking the derivative of the load capacity with respect to the vertical position, Eq. (10).

$$k_z = -\frac{dF_L}{dh} \tag{10}$$

3. Tilt error

The plate at height h above the magnet is now tilted around the y-axis in clockwise direction by a tilt angle α, Fig. 5. The tilt angles are assumed to be small ($\alpha \leq 1°$), therefore at an angle θ, α is reduced to γ according to Eq. (11). A cross-section of the bearing at angle θ is given in Fig. 6. This figure presents the pressure distribution that acts on the plate. Moreover, a body fixed frame of reference (r', θ', z') is introduced which will be used to calculate the load capacity and torque.

In contrast to Eq. (8), the pressure is now dependent on the angular coordinate θ', since the system is not axisymmetric any more. The total load capacity of the bearing perpendicular to the surface of the plate is obtained by combining Eq. (2) and Eq. (12), Eq. (13). The load capacity in vertical direction is approximately the same as the load capacity perpendicular to the surface of the plate for small tilt angles ($F_L \approx F_L'$). Note that in this analysis, part of the resultant force F_L', acting in r-direction due to the tilt, is neglected. This force accelerates the plate and possibly results in the plate gliding off the ferrofluid.

$$\gamma = \alpha \cos(\theta) \tag{11}$$

$$F_L' = \int_0^{2\pi} \int_0^{r_o'(\theta')} \left(p(r', \theta') - p_0 \right) r'\, dr'\, d\theta' \tag{12}$$
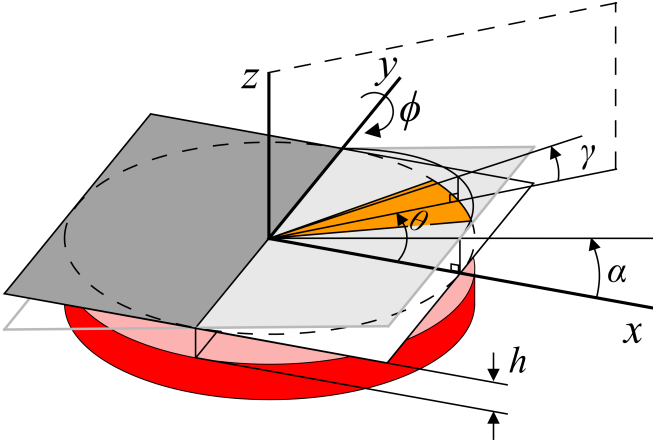
FIG. 5. Schematic representation of the tilted bearing. The plate is tilted around the y-axis by an angle α. A cross-section of the bearing at the angle θ is shown in Fig. 6.
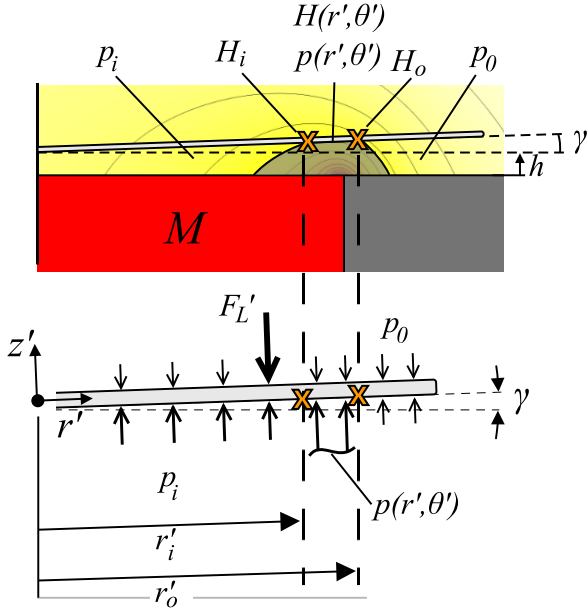

FIG. 6. The shape of the ferrofluid seal and the resulting pressure distribution over the seal for a tilted bearing. Note that a body fixed frame of reference is introduced in the center of mass of the plate and that the tilt angle γ is introduced.

$$F_L' = \mu_0 M_s \left(H_i - H_o \right) \int_0^{2\pi} \int_0^{r_i'(\theta')} r' dr' d\theta' \qquad (13)$$

$$+ \mu_0 M_s \int_0^{2\pi} \int_{r_i'(\theta')}^{r_o'(\theta')} \left(H(r', \theta') - H_o \right) r' dr' d\theta'$$

Next, the torque that acts on the plate around the y-axis (M_y) can be calculated by multiplying the pressure distribution with its lever arm and integrating it over the entire area of the bearing, Eq. (14). Note that this is easily done in the body fixed frame of reference since the pressure distribution acts normal to the plate. Due to symmetry the resulting torque around the x-axis is zero.

$$M_y = \iint -(p(r',\theta') - p_0) r' cos(\theta') r' dr' d\theta' \qquad (14)$$

Finally, the tilt stiffness of the bearing (k_ϕ) around the y-axis (ϕ-direction) can be calculated by taking the derivative of the torque with respect to the tilt angle, Eq. (15). The negative sign is missing since the angle α is defined in the negative ϕ-direction.

$$k_\phi = \frac{dM_y}{d\alpha} \qquad (15)$$

The sensitivity of the load capacity and operational range with respect to tilt will be included in the sensitivity analyses. Moreover, the effects of the saturation magnetization and the applied volume of ferrofluid are included, see the results in Section III B.

4. Mass inside pocket

If the pressure inside the pocket exceeds the maximum pressure the seal can withstand with respect to ambient pressure (Eq. (4) and Eq. (16a)), the seal breaks, air escapes and the bearing loses mass until equilibrium can be obtained again (Fig. 3 and Eq. (5)), as observed by Lampaert et al.[34]. Consequently, this mass loss changes the characteristics of the bearing, namely the load capacity and stiffness. Mass gain also changes the characteristics. When the pressure difference over the seal exceeds the minimum strength of the seal (Eq. (6) and Eq. (16c)), mass is gained until equilibrium can be obtained again, (Fig. 4 and Eq. (7)).

By introducing the ideal gas law in the calculations, the equilibrium position of the seal becomes dependent on the air mass enclosed by the ferrofluid seal, Eq. (3) and Eq. (16b). Compression and decompression of the bearing are assumed to be done in a slow fashion, such that the system can continuously adjust itself to the temperature of the surroundings. Therefore, it is reasonable to assume an isothermal process, $\overline{R}T = $ Constant, with the temperature assumed to be room temperature, $T = 293K$. The molar mass of air is denoted by M_{air} and the universal gas constant by $\overline{R}$. Initially, the mass of air inside the pocket is $m_{i,0}$, which is defined as the mass encapsulated by the seal at the fly height h_0, Fig. 7.

$$\begin{array}{rll} p_i > p_{i,max} & \text{Loosing mass} & (16a) \\ p_{i,min} \leq p_i \leq p_{i,max} & \text{Constant mass} & (16b) \\ p_i < p_{i,min} & \text{Gaining mass} & (16c) \end{array}$$

B. FEM implementation

The goal of the FEM is to calculate the magnetic field produced by the magnet and subsequently to calculate

the equilibrium position of the ferrofluid seal for varying m_i, V_{ff}, α, M_s and h. Using the position of the seal, the load capacity and torque can be calculated and the total behaviour of the bearing is obtained.

The shape and position of the ferrofluid seal for an arbitrary fly height h, is completely defined by the two variables H_i and H_o, Fig. 8. Therefore, an additional formulation (Γ), dependent on these variables, is introduced in the FEM, in order to distinguish air and ferrofluid, Fig. 7 and Eq. (17). $\Gamma = 1$ for all the coordinates which are part of the union of the sets Ω_1 and Ω_2 and indicates ferrofluid. Air is defined by $\Gamma = 0$, therefore volume integration of Γ results in the total amount of ferrofluid present in the system, equation 18. Next, the solving strategies for a perfectly aligned bearing as well as a tilted bearing will be discussed.
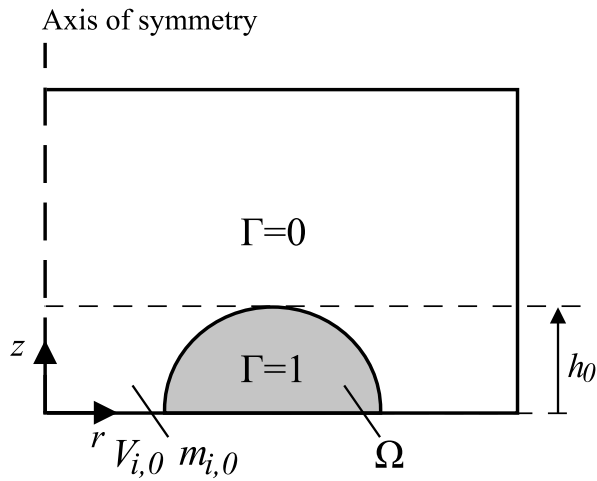

FIG. 8. The ferrofluid domain ($\Gamma = 1$) is divided into the sets Ω_1 and Ω_2, which are defined by H_i, H_o, H_{max} and h.

equations are implemented using *Global ODEs*. The calculations start from the fly height h_0 with the initial mass $m_{i,0}$ inside the pocket with volume $V_{i,0}$, Fig. 7. The characteristic of the aligned bearing is obtained by calculating the position of the ferrofluid for different fly heights. An overview of the solving strategy is given in Fig. 9.

FIG. 7. Air and ferrofluid are distinguished by the function Γ in the FEM.

$$\Gamma(r, z, \theta) = \begin{cases} 1 & \text{if } (r, z, \theta) \in (\Omega_1 \cup \Omega_2) \quad \text{Ferrofluid} \\ 0 & \text{if } (r, z, \theta) \notin (\Omega_1 \cup \Omega_2) \quad \text{Air} \end{cases}$$
(17)

$$V_{ff} = \iiint \Gamma(r, z, \theta) dV$$
(18)

1. Perfect alignment

When there is no tilt error, the system is axisymmetric which simplifies Γ to $\Gamma(r, z)$. Therefore, the system is modelled in COMSOL Multiphysics®[36] as 2D axisymmetric. First, the magnetic field generated by the magnet is calculated using the *Magnetic fields, No current physics*. Subsequently, the equilibrium position of the ferrofluid seal is calculated by combining all the different forces (Eq. (2) and Eq. (3)) with the description for the ferrofluid (Eq. (17) and Eq. (18)). These additional
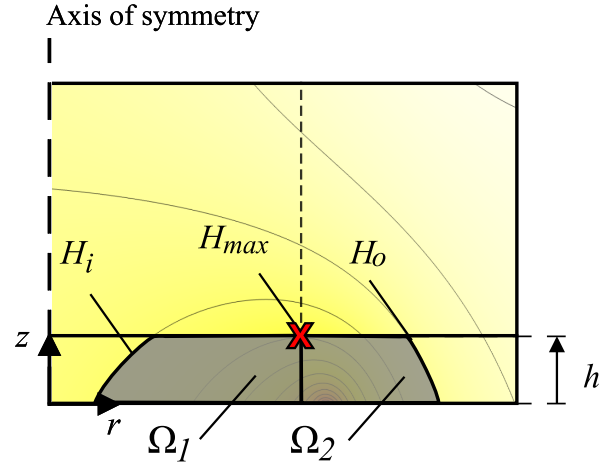

FIG. 9. The solving strategy for the aligned ferrofluid bearing.

represents the pressure distribution of that entire part. The interval and size β of each partition is determined by the number of subdivisions N, Fig. 11 and Eq. (21).

To illustrate this, the pressure distribution of partition k simplifies from $p(r', \theta')$ to $p(r', \theta = \beta k)$ on the interval between its lower boundary $(\theta_{l,k})$ and upper boundary $(\theta_{u,k})$. Note that the tilt angles are small $(\alpha \ll 1°)$, therefore the angular coordinate θ is approximately the same in the global and body fixed frame of reference $(\theta' \approx \theta)$. The cross-section presented in Fig. 6 corresponds to the centerline of the orange partition presented in Fig. 5 and Fig. 11. Note that increasing the number of elements increases the accuracy of the approximation but also increases computational time. In the calculations $N = 16$.

The advantage of the discretization is that each partition can be modelled using a 2D axisymmetric model, each with a slightly different tilt angle $(\gamma_k \approx \alpha \cos(\theta = \beta k)$, Eq. (11)). The disadvantage is that N calculations are needed. The model is solved for static equilibrium in an iterative fashion for the variables H_i and H_o, Fig. 10. The fminbnd algorithm in the Matlab® R2018a optimization toolbox[37] is used in combination with the Livelink for the finite element calculations in COMSOL Multiphysics®[36]. When H_i and H_o are known, both the load capacity and torque of the tilted bearing (Eq. (13) and Eq. (14)) can be calculated using the discretization, Eq. (22) and Eq. (23). Note that the lever arm of the pressure distribution can be approximated as $r'cos(\theta)$ for small tilt angles.

$$\beta = \frac{2\pi}{N} \tag{21}$$

$$F_L \approx \sum_{k=1}^{N} \int_{\theta_{l,k}}^{\theta_{u,k}} \int_{0}^{r'_o(\theta=\beta k)} (p(r', \theta = \beta k) - p_0)\, r' dr' d\theta \tag{22}$$

$$M_y \approx \sum_{k=1}^{N} \int_{\theta_{l,k}}^{\theta_{u,k}} \int_{0}^{r'_o(\theta=\beta k)} -(p(r', \theta = \beta k) - p_0)\, r'\, cos(\theta) r' dr' d\theta \tag{23}$$

FIG. 10. The solving strategy for the tilted ferrofluid bearing.

C. Experimental set-up

The presented model was validated by comparing the results of the theoretical model and the experiments that were performed as described below. In the validation, both the load capacity and stiffness were compared and discussed.

Experiments were performed using a test set-up as shown Fig. 12. A Zwick/Roell Z005 was used to measure the force over displacement behaviour of the bearing. The relative accuracy of the force measurement is 0.21%, whereas the repeatability has an accuracy below 0.33%. For the displacement measurement, the repeatability is $0.3\mu m$ and the accuracy is $0.6\mu m$.

2. Tilt error

Due to the tilt error, the system is not axisymmetric any more, Fig. 5. Therefore, the previously described solving strategy cannot be used any more. The problem can still be solved by modelling it in 3D, however this becomes computational expensive when more accuracy is needed. In order to reduce computational cost, the tilted bearing will be approximated by implementing a 2D (middle) Riemann sum, in which the pressure distribution at the centerline of each individual part k,
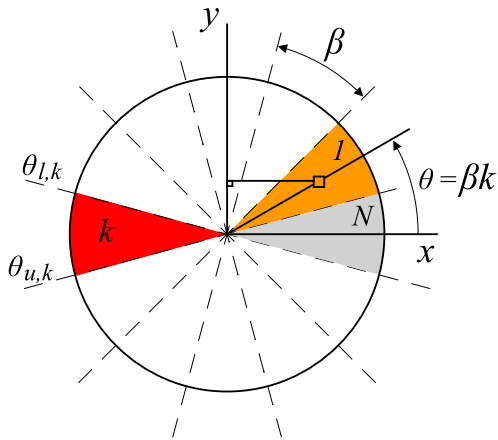
FIG. 11. The discretization of the tilted bearing (Fig. 5) in a top view. The lever arm around the y-axis of a small pressure element is displayed.

The ferrofluid bearing under testing consisted of a cylinder magnet, HKCM 9961-835, with a radius of $40mm$, a height of $10mm$ and a remanent flux density of $1.28T$, placed in an aluminium casing. Next, the magnet attached to the aluminium casing, chosen for its non-ferromagnetic properties, was placed onto a low-grade steel plate. This is convenient since no glue or other connections were needed for the connection of the base plate and magnet. Finally, the magnet was mounted onto the testing machine using stainless steel bolts and aluminium clamps, Fig. 12. It is important to note that the head of the tensile testing machine was made of aluminium. If the material would be ferromagnetic, the force measurement would be errored, since the magnet would attract the head of the machine.

1. Initialization

Before the measurement started, the test set-up had to be prepared properly, meaning alignment of the machine and bearing, application of the ferrofluid and determination of the position of the surface of the bearing. This was done in the following manner: the head of the tensile tester was pressed onto the bearing with a force of $100N$, in order to determine the position of the surface of the bearing, $h = 0mm$, and the stiffness of the test set-up, approximately $2 \cdot 10^6 N/m$. At $h = 0mm$, the surface of the head was aligned to the surface of the bearing using the nuts and bolts, red marking in Fig. 12.

Next, the head was retracted and ferrofluid was applied to the system using a pipette. The pipette is slightly inaccurate, since the ferrofluid was pulled out of the nozzle due to the magnetic attraction of the magnet onto the ferrofluid. Therefore, the mass of the pipette filled with ferrofluid was measured before and after application of the ferrofluid, using a weigh scale with an uncertainty of $0.005g$. By combining the density of the ferrofluid,

$\rho = 1380kg/m^3$, and the difference in mass, which corresponds to the applied mass of ferrofluid, the applied volume could be calculated.

The ferrofluid used in the measurements is the Ferrotec APG 513A, which has a saturation magnetization of $M_s = 32kA/m$ at a temperature of $300K$. The applied volume of ferrofluid in the measurements was $0.38ml$.

2. Measurements

Before the actual measurements, an initial pre-wetting step was performed. This means compressing the bearing maximally until the head reaches $h = 0mm$. This was done in order to apply a thin film of ferrofluid onto the head of the tensile testing machine, such that the experiments performed afterwards were repeatable. The thin film of ferrofluid only has to be applied once. Effectively, this means that the applied volume of $0.38ml$ is slightly decreased.

After the pre-wetting step, three different measurements were performed, Fig. 13. First, the maximum load capacity of the bearing was measured by completely compressing the bearing until $h = 0mm$. During the second and third measurement, the bearing was compressed until heights of $0.1mm$ and $0.35mm$ respectively, after which the bearing was fully decompressed. All the measurements were performed with a speed of $0.3mm/min$.
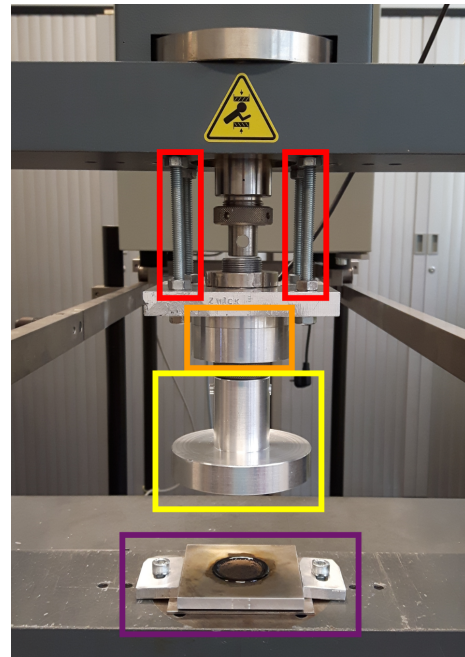

FIG. 12. The test set-up consists of: the ferrofluid bearing (purple), the head of the tensile testing machine (yellow) and the load cell (orange). The stiffness of the test set-up is approximately $2 \cdot 10^6 N/m$.
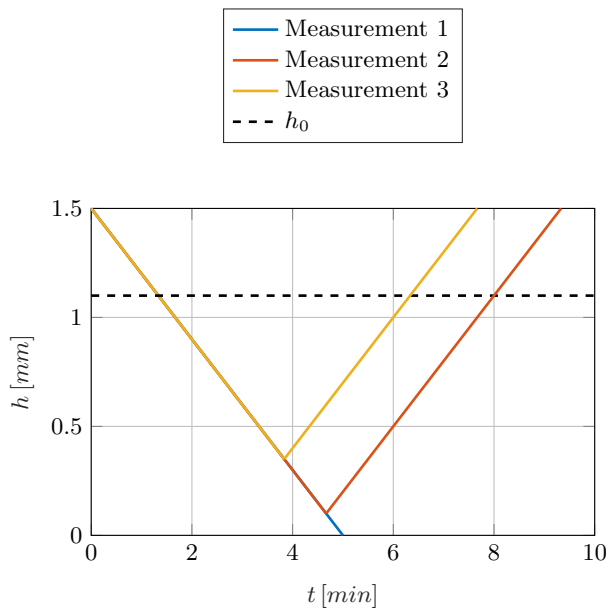
FIG. 13. The position of the tensile testing machine (fly height h) versus the time for the different measurements. All three measurements start $1.5mm$ above the surface of the magnet. h_0 indicates the height of the ferrofluid seal.

III. RESULTS

A. Model validation: load capacity and operational range

The results of the measurements described in Section II C 2 are given in Fig. 14. In this figure, the load capacity of the ferrofluid pocket bearing is shown versus the fly height for both the measurements and the model. The expected load capacity, calculated using the suggested model, is shown with black markers, while the different measurements are indicated with continuous lines.
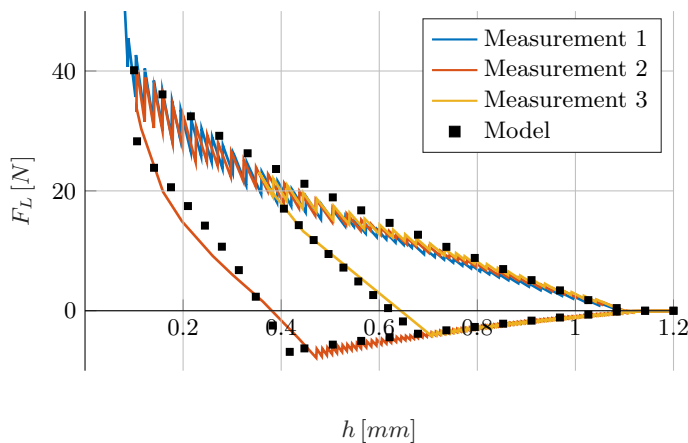

FIG. 14. The modelled load capacity is compared to the measurement results. The maximum load capacity is given in blue, while red and yellow indicate two different compression and decompression cycles.

Fig. 15 shows the pressure and mass inside the pocket of the ferrofluid bearing versus the fly height. Note that the values correspond to the values of the model given in Fig. 14. These results are used to explain and interpret the behaviour of the bearing, namely the mass loss and operational range. In the top figure, the blue colour indicates the maximum pressure that the ferrofluid seal can withstand at that fly height, see also Fig. 3. The corresponding mass inside the pocket at maximum pressure is given in the bottom figure in blue. Note that the mass is normalized with respect to the initial mass $m_{i,0}$, Fig. 7. The red colour indicates the minimum pressure that the seal can withstand, see also Fig. 4. The corresponding mass inside the pocket is given in the bottom figure in red. The black lines correspond to measurements 2 and 3 of Fig. 14. The operational range of the ferrofluid pocket bearing is coloured green.
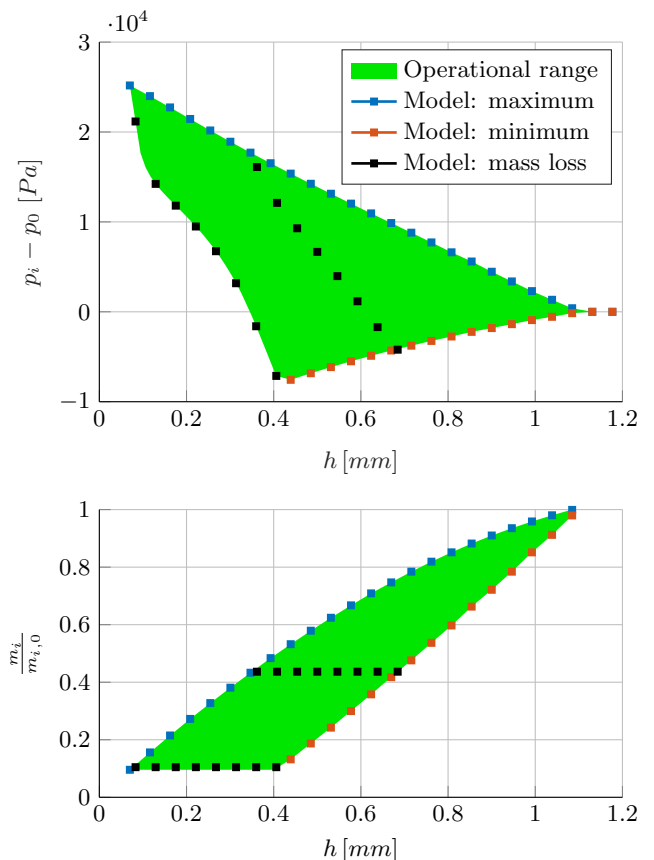
FIG. 15. The pressure difference the ferrofluid seal can withstand (top figure) determines the operational range of the ferrofluid pocket bearing (bottom figure). Decreasing the fly height increases the maximum and minimum strength of the ferrofluid seal, but decreases the air mass inside the pocket. The black markers correspond to measurements 2 and 3 from Fig. 14.

In the top figure of Fig. 16, the part of measurement 3 (Fig. 14) that is located in the operational range of the bearing according to Fig. 15, is presented. The bottom figure of Fig. 16 shows both the stiffness of the bearing

derived from the load capacity measurements, as well as the stiffness derived from the load capacity predicted by the model.

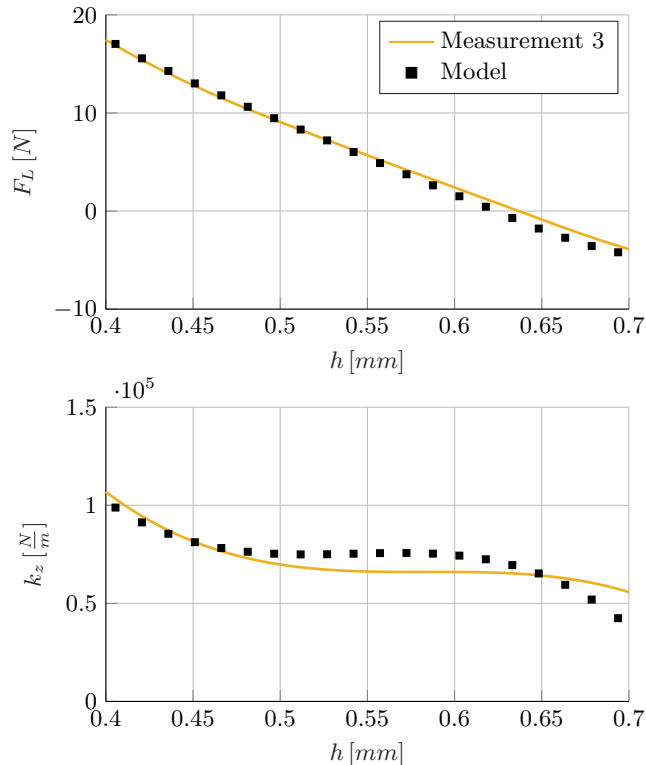FIG. 16. The load capacity (top figure) and stiffness (bottom figure) of the bearing, in the operational range of measurement 3 (Fig. 14), are compared to the model.

B. Sensitivity analysis

In this section, the sensitivity of the load capacity and operational range with respect to the saturation magnetization of the ferrofluid (Fig. 17), the applied volume of ferrofluid (Fig. 18) and the tilt error (Fig. 19) are given. The load capacity of the bearing significantly increased when the saturation magnetization increased. The operational range did not change significantly when the saturation magnetization was increased from $20kA/m$ to $40kA/m$. Fig. 18 shows that increasing the amount of ferrofluid increases both the load capacity and operational range. In contrast, Fig. 19 shows that tilt decreases both.

Fig. 20 and Fig. 21 present the torque and the tilt stiffness with respect to the tilt angle for both the maximally and minimally pressurized pockets. Both figures globally show the same behaviour. When the tilt angle is positive, the torque and tilt stiffness are positive for all the different fly heights. The torque and tilt stiffness increase when the fly height is decreased or when the tilt angle is increased. When the pocket of the bearing was minimally pressurized, the magnitude of both the torque and

tilt stiffness are lower when compared to the maximally pressurized pocket.

IV. DISCUSSION

A. Model validation: load capacity and operational range

All three measurements given in Fig. 14 show a zig-zag pattern, indicating s that the mass of air inside the pocket changes. Either mass is gained or mass is lost. When the bearing is compressed, the pressure inside the pocket increases and the load capacity increases. When the pressure increases such that the strength of the ferrofluid seal gets exceeded, mass escapes out of the pocket, as described in Section II A 4. During decompression, the pressure inside the pocket decreases. When the ferrofluid seal cannot withstand the pressure difference any more, mass is gained. Thus, the strength of the ferrofluid seal defines the maximum and minimum load capacity of the bearing, which increase when the fly height is decreased. Overall, both the load capacity and stiffness of the ferrofluid pocket bearing seem to be accurately described by the suggested model, Fig. 14 and Fig. 16.

Measurements 2 and 3 showed that the behaviour of the bearing during decompression differs from the behaviour found during the initial compression. This phenomenon can be explained by the fact that mass is lost during the initial compression, which changes the system and therefore its characteristics. The zig-zag pattern is not present in the measurements during decompression of the bearing, indicating constant mass. After the minimum strength of the seal gets exceeded, or minimum load capacity, mass is gained and the system changes again. The behaviour of the bearing is repeatable and predictable in the operational range.

The operational range of measurement 3 is well described by the model. In contrast, measurement 2 shows that decompression of the bearing, after almost maximum compression, is less accurately described by the model. Therefore, the assumption that both compression and decompression are isothermal processes seems to be a reasonable assumption.

Inaccuracy of the model at these low fly heights could possibly be explained by the neglected surface effects, like capillary effects and surface tension. Also, the FEM model neglects magnetization of the ferrofluid in the calculations. Moreover, the FEM model is sensitive to extraordinary boundary effects and the size of the fillets of the magnet at low fly heights. The measurement itself can also be errored at low fly heights due to for example a damaged magnet. Dents in the magnet result in magnetic field concentrations near the magnet. This effect becomes less pronounced further away from the magnet.

The stiffness of the test set-up is approximately 10 times the stiffness of the bearing. A force of $40N$, which is the approximately the load capacity of the bearing at a fly height of $0.1mm$, results in a displacement error
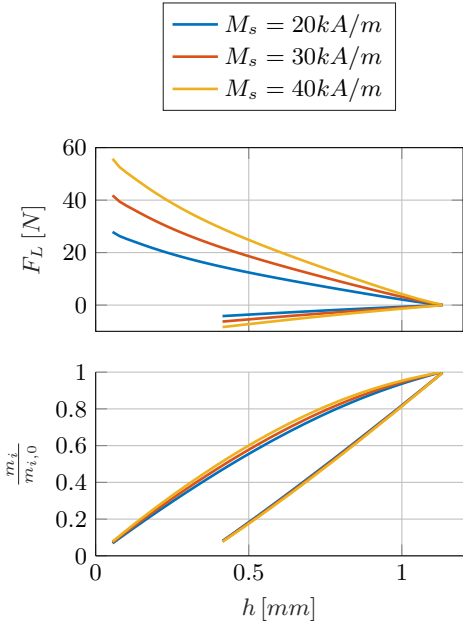
FIG. 17. The modelled sensitivity of the load capacity (top figure) and the operational range (bottom figure), with respect to the saturation magnetization. The other parameters correspond to the measurements, $V_{ff} = 0.38ml$ and $\alpha = 0°$.
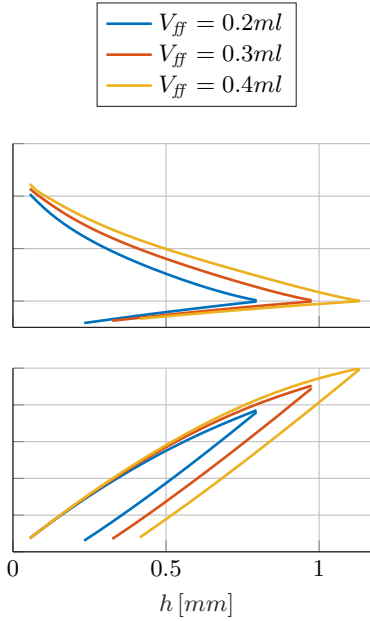
FIG. 18. The modelled sensitivity of the load capacity (top figure) and the operational range (bottom figure), with respect to the applied volume of ferrofluid. The other parameters correspond to the measurements, namely $M_s = 0.32kA/m$ and $\alpha = 0°$.
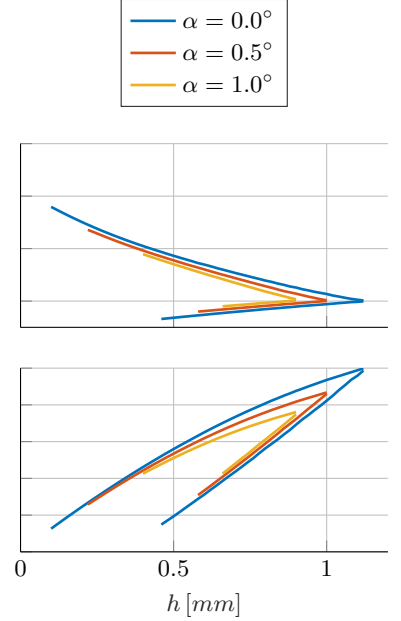
FIG. 19. The modelled sensitivity of the load capacity (top figure) and the operational range (bottom figure), with respect to the tilting of the bearing. The other parameters correspond to the measurements, namely $V_{ff} = 0.38ml$ and $M_s = 0.32kA/m$.

of maximally $20\mu m$. Other uncertainties in the model are the saturation magnetization of the steel base plate and the temperature of the environment. The temperature was not measured during the experiments, but is assumed to be approximately $293K$.

A big disadvantage of the presented FEM model is that only static and quasi static problems can be solved, not dynamic problems. This is because the FEM finds the positions of the interfaces between ferrofluid and air by solving for static equilibrium. In contrast, the FEM description makes it possible to include other forces, like capillary forces and surface tension, and to include magnetization of the ferrofluid.

Fig. 15 will be used to illustrate and explain the behaviour of Fig. 14 and to determine the operational range of the bearing. The operational range is indicated in green and is determined by the minimum and maximum pressure difference that the ferrofluid seal can withstand. When the fly height is decreased, the ferrofluid is pushed radially outwards causing ΔH to increase subsequently increasing the strength of the seal. Moreover, the magnetic field is stronger near the magnet thus compression of the bearing will also result in an increased ΔH. The combination of these two effects explains the increase in strength of the ferrofluid seal given in the top figure of Fig. 15.

The operational range of the bearing can easily be determined from Fig. 15, by looking at different con-

stant mass lines or horizontal lines in the bottom figure. The intersection between a constant mass line and the green area indicates the operational range for that specific mass. Two examples are given with two sets of black markers. If the fly height is decreased beyond the operational range, mass is lost according to the set of blue markers. Afterwards, the new constant mass line can be used to determine the new operational range of the bearing. If the fly height is increased beyond the operational range, mass is gained according to the set of red markers. Thus, the operational range and behaviour of the bearing is determined by the initial compression, during which mass is squeezed out of the pocket. Note that ferrofluid bearings can easily be reset by separating the bearing and the plate.

It can be concluded that the model properly describes the behaviour of the bearing, except at very low fly heights. It might be interesting for further research to model and measure the behaviour of multiple seals and pockets, or to use an incompressible fluid instead of air inside the pocket. In both cases, it might be convenient to measure the actual pressure inside the pocket instead of only measuring the force and displacement.
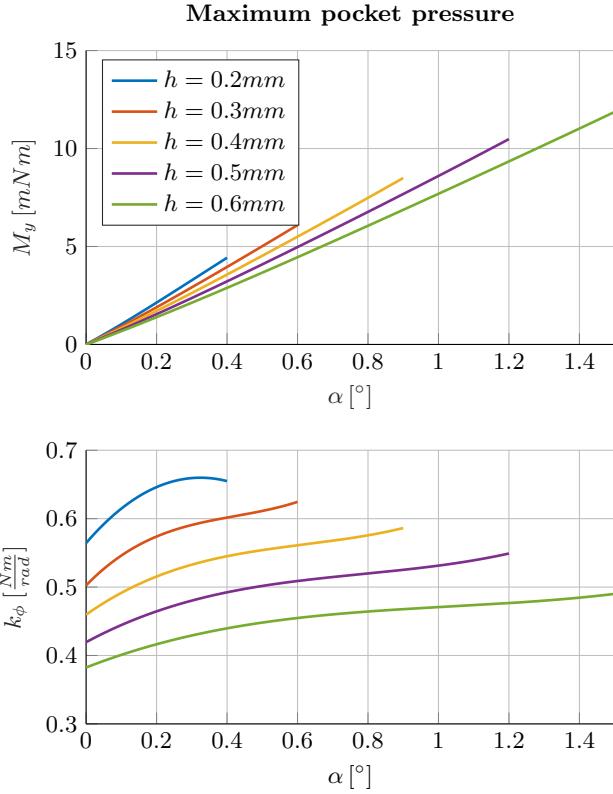
Maximum pocket pressure

Minimum pocket pressure

FIG. 20. The tilt stiffness (bottom figure) of a maximally pressurized ferrofluid pocket bearing is a result of the torque around the y-axis (top figure), Eq. (15)
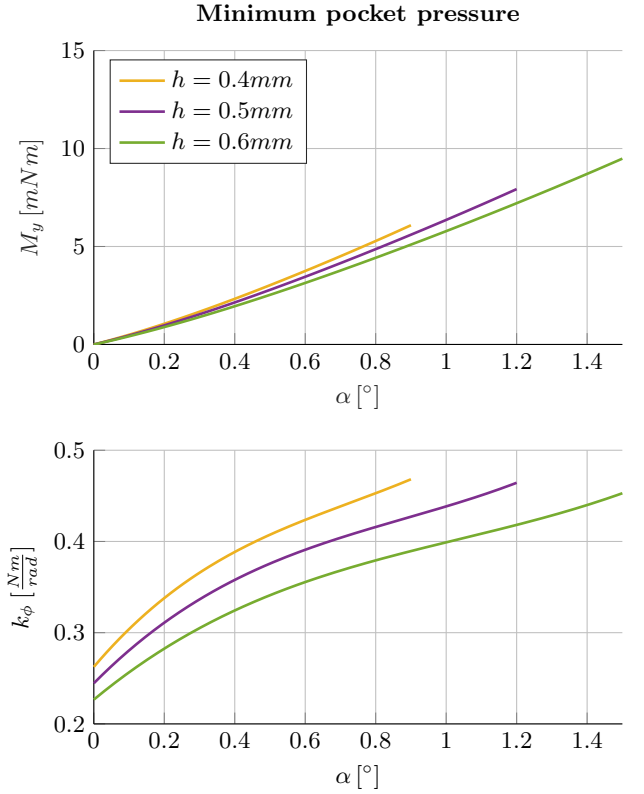
FIG. 21. The tilt stiffness (bottom figure) of a maximally pressurized ferrofluid pocket bearing is a result of the torque around the y-axis (top figure), Eq. (15)

B.   Sensitivity analysis

Only the three variables that are assumed to be the most erroneous during the actual measurements are discussed in the sensitivity analysis. Other variables, for example surface effects, are neglected in the sensitivity analysis, since they are either neglected or included in the derivation of the model on which the rest of the analysis is based on. The presented values in Fig. 17, Fig. 18 and Fig. 19 are a bit exaggerated for errors that might occur in practice. However, this way the effect of the different errors becomes clearly visible.

Both tilt and the applied volume of ferrofluid have a significant influence on both the load capacity and the operational range. In contrast to increasing the tilt angle, increasing the amount of ferrofluid increases the operational range and load capacity. Addition of more ferrofluid increases the height of the ferrofluid ring, thus results in earlier contact and establishment of both the seal and air pocket. However, the effect of adding more ferrofluid decreases at low fly heights. When the bearing is almost entirely compressed, the outer interface H_o is nearing zero, so addition of more ferrofluid does not increase ΔH significantly any more. In contrast, both saturation magnetization and tilt change the behaviour of the bearing at every fly height. The load capacity of

the bearing significantly increases when the saturation magnetization increases. This increase is linear according to Eq. (1) and Eq. (9). It is also worth noticing that the operational range of the bearing is limited by tilting of the plate. Higher tilt angles result in earlier contact of the plate with the bearing surface, thus limiting the operational range. Moreover, tilt decreases the height at which the enclosed air pocket is established, resulting in a decreased load capacity and operational range.

The small difference between the measured and the predicted load capacity can possibly be explained by the errors discussed here. Since only three possible errors are discussed, no conclusions can be drawn regarding which set of errors was present in the measurements. However, slight overestimation of the amount of ferrofluid is likely, since a ferrofluid trail is left behind on the head of the testing machine after the initial compression.

Fig. 20 and Fig. 21 show that the tilt stiffness of the bearing is positive for positive tilt angles, for both maximum and minimum pressure inside the pocket. Since the system is symmetric, the tilt stiffness is also positive for negative tilt angles. Therefore, due to the positive tilt stiffness, it can be concluded that the ferrofluid bearing is self-aligning regardless of the pressure inside the pocket. However, in order to be certain that the described behaviour of the ferrofluid bearing is indeed correct, it is

recommended that for future work the load capacity and torque of the bearing are actually measured for different tilt angles.

V. CONCLUSION

This article provides a simple and efficient way to obtain the operational range of a ferrofluid pocket bearing from only the mass versus fly height diagram. The operational range is only dependent on the magnetic field produced by the magnet and the amount of ferrofluid present in the system.

The experimentally validated model accurately describes the load characteristic of a ferrofluid pocket bearing. The model includes the air mass inside the pocket, since both the load capacity and stiffness of the bearing change when the mass changes. Overcompression of the bearing results in mass loss and overdecompression in mass gain. The bearing shows repeatable and predictable behaviour when the mass inside the pocket does not change. In practice, this is the operational range of the bearing.

The operational range of the bearing is sensitive to errors such as tilt or uncertainty in the applied volume of ferrofluid. The sensitivity analysis shows that tilt decreases both the load capacity and operational range of the bearing. Independent of the pressure inside the pocket, both the torque acting on the plate above the bearing and the resulting tilt stiffness are always positive when tilted. It can be concluded that ferrofluid pocket bearings are always self-aligning. The tilt stiffness increases when the fly height decreases or when the tilt angle increases. Increasing the amount of ferrofluid increases the operational range of the bearing significantly while the load capacity is only increased for higher fly heights.

[1] R. E. R. Rosensweig, *Ferrohydrodynamics* (Dover Publications Inc, 2013) p. 368.

[2] M. I. Shliomis, "Magnetic Fluids," Sov. Phys. Usp. **17**, 153 (1974).

[3] C. Scherer and A. Figueiredo Neto, "Ferrofluids: Properties and Applications," Brazilian Journal of Physics **35**, 718–727 (2005).

[4] K. Raj, B. Moskowitz, and R. Casciari, "Advances in ferrofluid technology," Journal of Magnetism and Magnetic Materials **149**, 174–180 (1995).

[5] K. Raj and R. Moskowitz, "Commercial applications of ferrofluids," Journal of Magnetism and Magnetic Materials **85**, 233–245 (1990).

[6] C. Rinaldi, A. Chaves, S. Elborai, X. He, and M. Zahn, "Magnetic fluid rheology and flows," Current Opinion in Colloid and Interface Science **10**, 141–157 (2005).

[7] H. Urreta, G. Aguirre, P. Kuzhir, and L. N. Lopez de Lacalle, "Seals Based on Magnetic Fluids for High Precision Spindles of Machine Tools," International Journal of Precision Engineering and Manufacturing **19**, 495–503 (2018).

[8] I. Torres-Díaz and C. Rinaldi, "Recent progress in ferrofluids research: novel applications of magnetically controllable and tunable fluids," Soft Matter **10**, 8584–8602 (2014).

[9] R.-J. Yang, H.-H. Hou, Y.-N. Wang, and L.-M. Fu, "Micromagnetofluidics in microfluidic systems: A review," Sensors and Actuators B: Chemical **224**, 1–15 (2016).

[10] H. C. Cheng, S. Xu, Y. Liu, S. Levi, and S. T. Wu, "Adaptive mechanical-wetting lens actuated by ferrofluids," Optics Communications **284**, 2118–2121 (2011).

[11] S. M. H. Jayhooni, B. Assadsangabi, and K. Takahata, "A stepping micromotor based on ferrofluid bearing for side-viewing microendoscope applications," Sensors and Actuators, A: Physical **269**, 258–268 (2018).

[12] R. Olaru, C. Petrescu, and R. Hertanu, "A novel double-action actuator based on ferrofluid and permanent magnets," Journal of Intelligent Material Systems and Structures **23**, 1623–1630 (2012).

[13] S. Sudo, Y. Takaki, Y. Hashiguchi, and H. Nishiyama, "Magnetic Fluid Devices for Driving Micro Machines," JSME International Journal Series B **48**, 464–470 (2005).

[14] E. Uhlmann and N. Bayat, "High precision positioning with ferrofluids as an active medium," CIRP Annals - Manufacturing Technology **55**, 415–418 (2006).

[15] N. Tipei, "Theory of Lubrication With Ferrofluids: Application to Short Bearings," Journal of Lubrication Technology **104**, 510–515 (1982).

[16] Q. Liu, S. F. Alazemi, M. F. Daqaq, and G. Li, "A ferrofluid based energy harvester: Computational modeling, analysis, and experimental validation," Journal of Magnetism and Magnetic Materials **449**, 105–118 (2018).

[17] R. Rosensweig, "Magnetic fluid seals," (1970).

[18] R. E. Rosensweig, K. Raj, and T. J. Black, "Non-bursting ferrofluid seal," (2003).

[19] Y. Mitamura, S. Takahashi, S. Amari, E. Okamoto, S. Murabayashi, and I. Nishimura, "A magnetic fluid seal for rotary blood pumps: Effects of seal structure on long-term performance in liquid," Journal of Artificial Organs (2011), 10.1007/s10047-010-0526-8.

[20] R. Ravaud, G. Lemarquand, and V. Lemarquand, "Mechanical properties of ferrofluid applications: Centering effect and capacity of a seal," Tribology International (2010), 10.1016/j.triboint.2009.04.050.

[21] R. Rosensweig, "Magnetic fluids," Annual Review of Fluid Mechanics **19**, 437–461 (1987).

[22] O.G.R. Potma, *Designs for rotary shaft fluid seals in an aqueous environment using ferrofluid*, Msc thesis, Technical University Delft (2017).

[23] A. Arcire, R. Olaru, and C. Petrescu, "Study of the influence of ferromagnetic material on the characteristics of an actuator based on ferrofluid and permanent magnets," EPE 2012 - Proceedings of the 2012 International Conference and Exposition on Electrical and Power Engineering , 776–780 (2012).

[24] A. Boots, L. Krijgsman, B. de Ruiter, S. Lampaert, and J. Spronck, "Increasing the load capacity of planar ferrofluid bearings by the addition of ferromagnetic material," Tribology International **129** (2019), 10.1016/j.triboint.2018.07.048.

[25] R. Olaru, C. Petrescu, and A. Arcire, "Maximizing the magnetic force generated by an actuator with non-magnetic body in a ferrofluid pre-magnetized by permanent magnets," International Review of Electrical Engineering **8**, 904–911 (2013).

[26] A. Alvarez-Aguirre, G. Mok, S. H. HosseinNia, and J. Spronck, "Performance improvement of optical mouse sensors: Application in a precision planar stage," 2016 International Conference on Manipulation, Automation and Robotics at Small Scales, MARSS 2016 (2016), 10.1109/MARSS.2016.7561698.

[27] R. Deng, S. van Veen, M. Café, J. W. Spronck, and R. H. M. Schmidt, "Linear Nano-Positioning Stage using Ferrofluid Bearings," in *euspen international Conference*, June (2014) p. 4.

[28] S. Lampaert, J. Spronck, R. van Ostayen, and M. Café, "(2 + 4) DOF precision motion stage with ferrofluid bearings," **301681701**, 5–8 (2014).

[29] S. Lampaert, J. Spronck, R. van Ostayen, and H. Habib, "XY360 planar positioning stage with ferrofluid bearings," DSPE-Conference 2016 , 57–61 (2016).

[30] G. Millet and A. Hubert, "Design of a 3 DOF displacement stage based on ferrofluids." Actuators'06 , 656–659 (2006).

[31]S. Lampaert, B. J. Fellinger, J. W. Spronck, and R. A. J. V. Ostayen, "In-plane friction behaviour of a ferrofluid bearing," Precision Engineering (2017), 10.1016/j.precisioneng.2018.05.013.

[32]M. Petit, A. Kedous-Lebouc, and Y. Avenas, "Calculation and analysis of local magnetic forces in ferrofluids," Przegląd Elektrotechniczny , 115–119 (2011).

[33]J. Yu, X. He, D. Li, and W. Li, "Boundary interface condition of magnetic fluid determines the magnetic levitation force experienced by a permanent magnet suspended in the magnetic fluid,"

Physics of Fluids **30**, 092004 (2018).

[34]S. Lampaert, J. Spronck, and R. van Ostayen, "Load and stiffness of a planar ferrofluid pocket bearing," Proceedings of the Institution of Mechanical Engineers, Part J: Journal of Engineering Tribology , 135065011773920 (2017).

[35]J. L. Neuringer and R. E. Rosensweig, "Ferrohydrodynamics," Physics of Fluids **7**, 1927–1937 (1964).

[36]COMSOL, "COMSOL Multiphysics," (2018).

[37]MathWorks, "MATLAB,".

Chapter 3

Discussion

The overall goal of this thesis project was to develop new design rules for ferrofluid bearings, such that ferrofluid bearings can become a serious contender for implementation in bearing systems, Figure 1-1 in Chapter 1. First, the main findings of the paper (Chapter 2) will be discussed, after which the different appendices will be discussed. Finally, a brief overview of this project is given, including a couple of future challenges and opportunities.

3-1 Paper

The paper presents a (FEM) model which calculates the equilibrium position of the bearing, based on the air mass inside the pocket, assumed to be an ideal gas, and the strength of the ferrofluid seal. Aligned bearings can simply be modelled axisymmetrically, whereas tilted bearings cannot. In order to avoid full 3D modelling of the tilted bearing, a discretization (2D middle Riemann sum) was implemented, such that the bearing could be approximated using N axisymmetric calculations. It was found that a discretization of at least $N \geq 16$ is required, in order to calculate the performance of the bearing within 0.5% accuracy (Figure C-2). The model was experimentally validated by measuring the force and displacement of a ferrofluid pocket bearing with the use of a tensile testing machine.

Overcompressing the bearing resulted in mass loss out of the air pocket and overdecompressing in mass gain. As long as the mass did not change by an over(de)compression, the behaviour of the bearing showed to be repeatable (operational range). The observed behaviour was successfully described by the FEM model, thereby partly completing the goals of this thesis project (Chapter 1). The model was subsequently used to present a method that obtains the operational range of the bearing from only the mass versus fly height diagram.

Finally, a sensitivity analysis showed how the performance of the bearing was affected by different errors. Tilt decreases the load capacity and operational range of the bearing, whereas increasing the amount of ferrofluid increases both. Moreover, the sensitivity analysis showed that (tilted) ferrofluid pocket bearings are always self-aligning, due to the positive tilt stiffness. These results led to the formulation of new design rules, Section 3-3.

An option that was not discussed in the paper, is to fill the pocket with water or any other incompressible fluid that is compatible with the chosen ferrofluid. This increases the stiffness of the bearing in the operational range. The maximum and minimum load capacity will not change. This behaviour can easily be implemented in the presented FEM model. Instead of keeping the mass inside the pocket constant, the volume needs to be kept constant. Another interesting step might be to include the magnetization of the ferrofluid and the surface tension in the FEM model.

3-2 Appendices

3-2-1 Supporting material paper

Part of the results presented in Chapter A were interpreted in Section B-3, using a self-defined (normalized) eccentricity, Eq. (B-1) and Eq. (B-2). This length scale indicates to what extent a ferrofluid pocket bearing can handle an off-center applied load. Initially, when the ferrofluid encloses the air pocket, the normalized eccentricity is high. The bearing can handle a relative big displacement error. Decreasing the fly height decreases the eccentricity. When the plate is near the magnet, the normalized eccentricity reduces to almost zero. Thus, the bearing can only handle a very small off-center applied load.

3-2-2 Additional work

The results in Chapter F suggest that the air mass that escapes out of the pocket due to overcompression is constant. Moreover, the mass loss seems to be independent of the velocity when the velocity stays below $0.1mm/min$. It was also observed that fast compression results in almost continuous mass loss. For future research, it is highly recommended to measure the pressure inside the pocket, in order to conclude whether the mass loss is indeed constant for ferrofluid pocket bearings.

3-2-3 Literature/background

The goal of the research presented in Chapter H was to increase the load capacity of ferrofluid pocket bearings, since it was observed that they have limited load capacity. Ferromagnetic material, in this case low graded steel, has the ability to concentrate the magnetic field and therefore to increase the load capacity of the bearing [2]. The research was structured as follows: The mathematical model presented by Lampaert et al. [24] was extended, such that it could used to calculate the load capacity of ferrofluid bearings with two pockets instead of only one. Next, the model was used to calculate the load capacity of the bearing with additional steel rings. The experimental validation showed that the model and measurements were in good accordance with each other and that the load capacity of the bearing was successfully increased by approximately a factor four. Subsequently, the validated model was used to optimize the dimensions of the steel rings for maximum load capacity.

It was found that the addition of the steel rings approximately doubled the load capacity of the bearing. The steel rings also established the second air pocket, which approximately doubled the load capacity once more. Therefore, the total load capacity was almost quadrupled. The optimization showed that the height of the steel rings should be matched to the height of the magnet. Moreover, a minimum width of the steel rings is required in order to prevent early saturation of the steel. The research resulted in the formulation of a new design rule in Chapter 3-3.

3-3 General overview

The contributions of this thesis project to the overall understanding of ferrofluid bearings are summarized in Figure 3-1. Finally, different guidelines and design rules can be formulated:

(1) Both the addition of ferromagnetic material next to the magnet, and the addition of a second pocket and seal, increase the load capacity of the ferrofluid pocket bearing by approximately a factor two. Note that this is geometry dependent.

(2) The behaviour of ferrofluid pocket bearings is repeatable when used in their operational range. The operational range can be determined from the mass versus fly height diagram.
(3) Tilt of either the plate or the bearing should be minimized, since tilt decreases the load capacity and the operational range.
(4) Increasing the volume of ferrofluid increases the load capacity and operational range. Ferrofluid should therefore be added to the system, until the point of diminishing returns.

These design rules are a result of the implementation of existing theoretical models in FEM software, but note that the presented model is limited. Dynamics cannot be calculated. Therefore, it is recommended for future research to model the interface between fluid, magnetic and solid in a different way. Doing this, possibly allows to model viscous losses, the escaping mass and the observed trail formation. Despite its limitations, the presented model is able to calculate quasi-static behaviour of the bearing, for example the sensitivity and the operational range. The results of these calculations were used to formulate the new design rules.

Now that many aspect of the overall performance of ferrofluid bearings can be calculated, it might be interesting to compare the actual performance of ferrofluid bearings and other bearing concepts in detail. Suggested is to specify some functional requirements, either design requirements or performance requirements, and to subsequently design, build, measure and compare the performance of the different bearings. To get a better understanding of the performance differences, perhaps only design requirements should be specified. An example can be to only constrain the dimensions of the bearing system and its main function.

During this thesis project, the presented models were only used to calculate the behaviour and sensitivity of planar ferrofluid bearings. However, they are (easily) applicable to ferrofluid seals as well. After modelling and understanding the behaviour of a single seal, an interesting step is to model and understand the interaction between multiple pockets and seals, for both compressible and incompressible fluids inside the pockets. The enhanced understanding can subsequently be used to design (staged) ferrofluid seals for vacuum or aqueous applications.
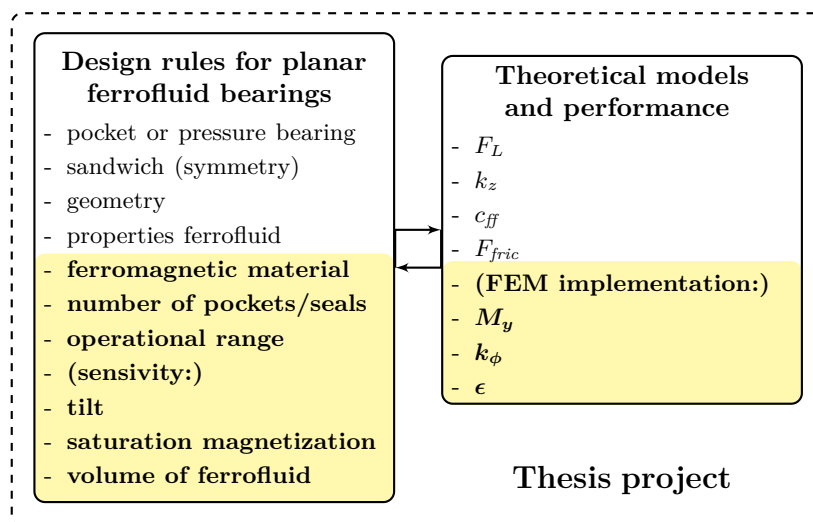

Figure 3-1: The contributions of this thesis project to the design rules, models and overall understanding of ferrofluid bearings.

Chapter 4

Conclusions

The goals of this thesis project were to develop new design rules for ferrofluid bearings and to model ferrofluid in a FEM analysis. Chapter 2 presented an experimentally validated (FEM) model to describe the behaviour of ferrofluid pocket bearings after over(de)compression. Subsequently, the model was used to determine the operational range and the sensitivity of the ferrofluid pocket bearing. Moreover, some additional work was done. For example, the load capacity of planar ferrofluid pocket bearings was optimized by addition of ferromagnetic material (team effort). The most important conclusions of this thesis project are summarized in this section according to the flowchart in Chapter 1. First, the conclusions of the main body of this thesis are presented, subsequently the conclusions of the appendices.

4-1 Paper

4-1-1 Model validation: load capacity and operational range

- The load capacity calculated using the suggested model, based on the ideal gas law and strength of the ferrofluid seal, is in good accordance with the measurement data.
- The observed behaviour of the bearing during compression-decompression cycles, can be explained by the air mass inside the pocket and the strength of the ferrofluid seal.
- The behaviour of the bearing is repeatable and predictable as long as the mass inside the pocket is unaltered. In practice, this is the operational range.
- The operational range can be determined in a simple and efficient way from the mass versus fly height diagram of the bearing.

4-1-2 Sensitivity analysis

- Increasing the saturation magnetization of the ferrofluid increases the maximum and minimum load capacity. The effect on the operational range is negligible.
- Adding more ferrofluid increases the maximum load capacity significantly. The increase is more significant at higher fly heights.
- The operational range increases significantly when more ferrofluid is added. More ferrofluid results in earlier contact of the plate with the seal. Therefore, the pocket is established at a higher fly height, resulting in load capacity and operational range.
- Tilt decreases the maximum and minimum load capacity of the bearing. A ferrofluid seal is as strong as its weakest link, which is the part furthest away from the magnet.
- Due to tilt, the pocket is established at a lower fly height. This decreases the operational range of the bearing mainly at higher fly heights.
- Tilt limits the achievable fly heights. Higher tilt angles result in earlier contact of the plate with the bearing surface.

- The resultant torque acts opposite to the tilt for maximum and minimum pressurized pockets. Therefore, a ferrofluid pocket bearing is always self-aligning.
- The tilt stiffness of a bearing with a maximum pressurized pocket is higher than a minimum pressurized pocket.
- The tilt stiffness increases when the fly height decreases or when the tilt increases.

4-2   Appendices

4-2-1   Supporting material paper

- The stiffness of the bearing increases when the air mass inside the pocket decreases.
- The eccentricity decreases when the fly height is decreased. Thus, the capacity of the bearing to handle an off-center applied load decreases.
- The eccentricity is negative for maximum pressure inside the pocket and positive for minimum pressure.
- The optimum discretization and mesh size for the tilted bearing is found to be: $N = 16$ and a physics-controlled mesh size of 5. This is a trade-off between calculation time and accuracy.

4-2-2   Additional work

- The number of zig-zags during compression increases when the speed decreases. When the speed becomes less than $0.1 mm/min$, the increase stagnates.
- Size of the zig-zags (ΔF) increases when the fly height decreases. Moreover, the size seems to be independent of velocity except for relative high speeds.
- The results suggest that the mass escaping out of the pocket is constant when the compressions are done in a relative slow fashion.

4-2-3   Literature/background

- The low viscous friction and the absence of stick-slip make ferrofluid bearings interesting for high precision system.
- The measurement data shows that the suggested model for calculation of the load capacity of a ferrofluid bearing with two air pockets is correct.
- Adding two steel rings next to the axially magnetized ring magnet increases the load capacity of the bearing approximately 3 to 4 times, depending on the fly height.
- Concentrating the magnetic field near the magnet using steel rings increases the load capacity by a factor two.
- Sandwiching the ring magnet between two steel rings creates a second air pocket that approximately doubles the load capacity.
- Placing the bearing on top of a steel plate increases the load capacity approximately 10%
- A minimum width of the steel rings is required to prevent early saturation of the ferromagnetic material. The optimum width is found to be approximately 1/3 of the width of the ring magnet.
- Maximum load capacity is obtained when the height of the steel rings equals the height of the magnet.

Chapter 5

Recommendations

This section presents a couple recommendations, ideas and tips for potential future research. General recommendations are given in the first section. Thereafter, recommendations regarding the model and experimental setup are summarized. Finally, some potential applications of ferrofluid pocket bearings are given.

5-1   General recommendations

- Try to find an energy description for the ferrofluid bearing. The assumptions made in the derivation of the load capacity by Lampaert et al. [24] result in a purely conservative system. Therefore, Lagrangian mechanics can (perhaps) be used. The system in motion is not conservative since there is viscous dissipation (hysteresis), however this can also be included in an extended Lagrangian model.

- Simplify the bearing model using an analytical approximation for the magnetic field produced by the magnet, either 1D or 2D. This reduces the calculation time significantly which makes the model suitable for optimization. This approach can also be combined with the proposed energy description.

- Develop design rules for ferrofluid bearings. Some recommended design variables are: pocket bearing, pressure bearing, number of pockets, number of seals, steel, geometry, (in)compressible fluid.

- In this thesis, the behaviour of the bearing is explained with respect to the fly height. For design rules, explore if the bearing is better described using other diagrams and representations. For example, a pressure versus mass diagram with isolines for the different fly heights.

- Model or measure the lifetime expectancy of a ferrofluid (seal). How much air or water diffuses through the seal over time. Are the magnetic nanoparticles a perfect colloidal suspension or do they sediment over time. When become surface instabilities important.

- Investigate the hysteresis observed during compression and decompression of the bearing in the operational range [24].

- Find solutions for the trail formation. Suggestions are: smart design, surface treatments and/or refill the ferrofluid or carrier liquid.

- Investigate the physics involved in the escaping air. Is it constant mass loss, constant volume loss or perhaps neither. The results (Chapter F) suggest that it is constant mass loss with respect to different fly heights and pressures, however it cannot be concluded with certainty.

- Compare the performance of ferrofluid bearings to other bearing concepts. For example, design and build a linear bearing system using ferrofluid bearings. Compare its performance to a market available air bearing system of approximately the same size.

5-2   Modelling

- Model the interaction between multiple (in)compressible pockets and seals. The seals can be concentric (planar ferrofluid bearing) or parallel (seals around axle). Can be combined with the energy or simplified description.
- Include the magnetization of the ferrofluid and the surface tension in the (quasi static) FEM model.
- Model the interface between fluid, magnetic and solid in a different way. The suggested model is not able to calculate dynamics, for example flow profiles or trail formation.
- The maximum load capacity decreases with velocity [24]. Calculate and validate the effect of the velocity on the load capacity of the bearing in the operational range.

5-3   Experimental setup

- Implement a torque transducer or a multi-DOF load cell in order to measure the torque of the bearing for various tilt angles. The goal is to validate the calculated torque and resulting tilt stiffness.
- Measure the pressure inside the pocket.
- Measure the temperature of the environment during the measurements.
- Check the uniformity of the magnetic field produced by the magnet using a Hall sensor.
- Redo the measurements and calculations with an incompressible fluid inside the pocket. Noteworthy, check the fluid-ferrofluid compatibility.

5-4   Potential applications

- Apply the presented models onto ferrofluid seals. Calculate the stationary strength of (staged) ferrofluid seals and the sensitivity to tilt.
- Control the position of the plate on top of the ferrofluid bearing by actively controlling the pressure inside the pocket, (thus controlling the load capacity and torque of the bearing).
- Use the ferrofluid seal as a passive valve by only controlling the pressure inside the pocket. (Depending on the physics involved, control the resulting volume or mass flow)

Additional figures paper
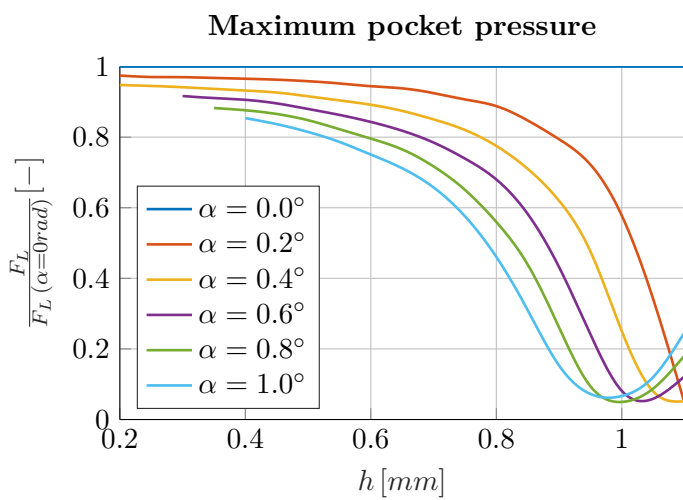
A-1 Data versus fly height

Figure A-1: This figure presents the calculated load capacity of the ferrofluid bearing at maximum pocket pressure for different tilt angles, α. The load capacity is scaled with respect to the load capacity at perfect alignment, $\alpha = 0°$.

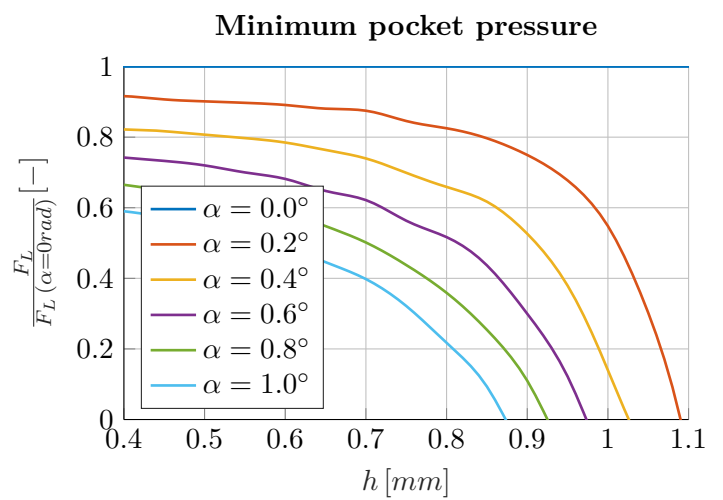**Figure A-2:** This figure presents the calculated load capacity of the ferrofluid bearing at minimum pocket pressure for different tilt angles, α. The load capacity is scaled with respect to the load capacity at perfect alignment, $\alpha = 0°$.

Figure A-3: This figure presents the load capacity, torque and eccentricity of the bearing for varying tilt angles and fly heights at maximum pocket pressure. The data corresponds to the data shown in Figure A-11, Figure A-12 and Chapter 2.
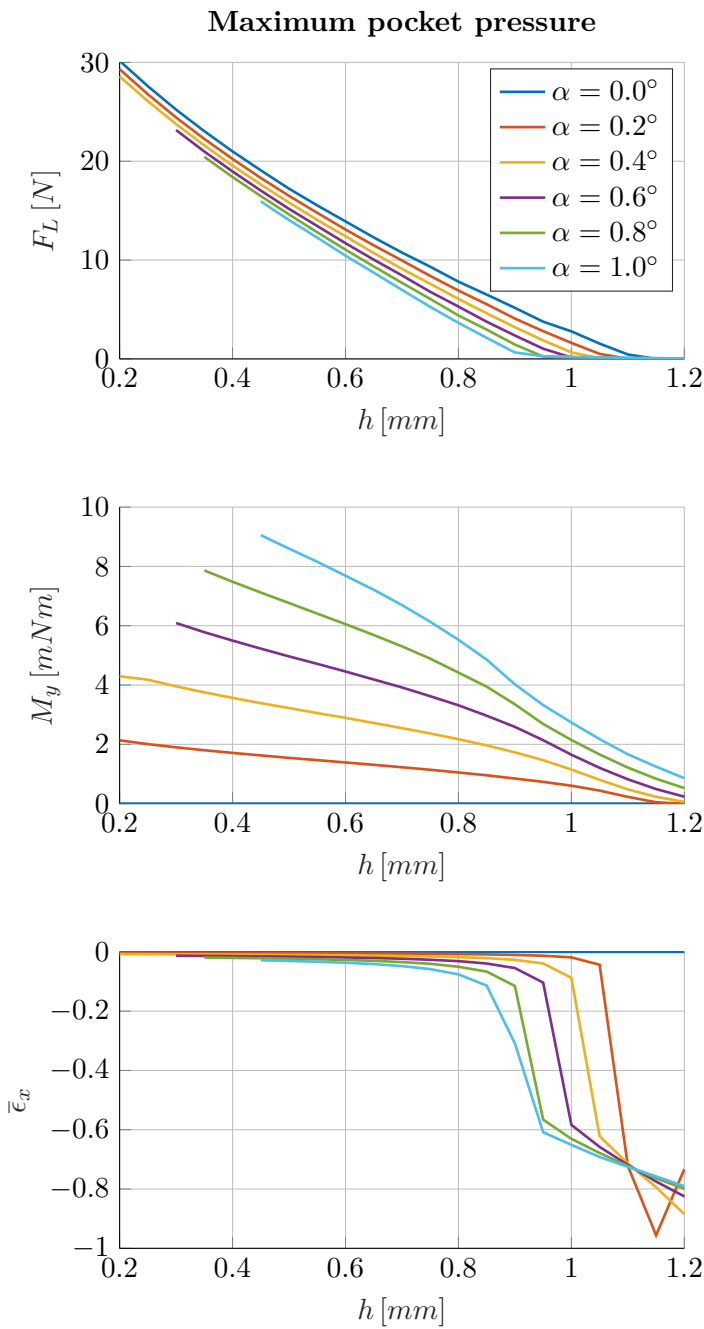
Figure A-4: This figure presents the load capacity, torque and eccentricity of the bearing for varying tilt angles and fly heights at minimum pocket pressure. The data corresponds to the data shown in Figure A-13, Figure A-14 and Chapter 2.

Figure A-5: This figure presents the pressure, volume and mass inside the pocket for varying tilt angles and fly heights at maximum pocket pressure. The data corresponds to the data shown in Figure A-11, Figure A-12 and Chapter 2.

Figure A-6: This figure presents the pressure, volume and mass inside the pocket for varying tilt angles and fly heights at minimum pocket pressure. The data corresponds to the data shown in Figure A-13, Figure A-14 and Chapter 2.
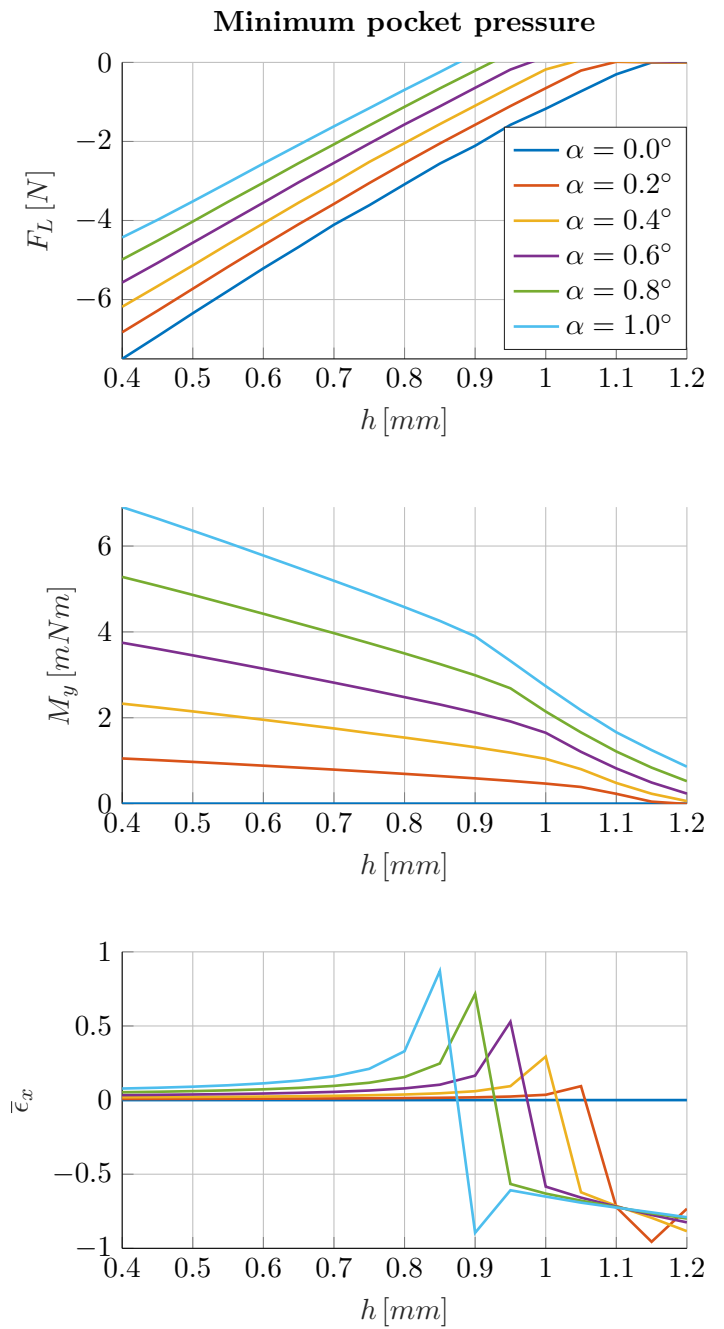
A-2   Data versus tilt angle

Figure A-7: This figure presents the load capacity, torque and eccentricity of the bearing for varying tilt angles and fly heights at maximum pocket pressure. The data corresponds to the data shown in Figure A-11, Figure A-12 and Chapter 2.
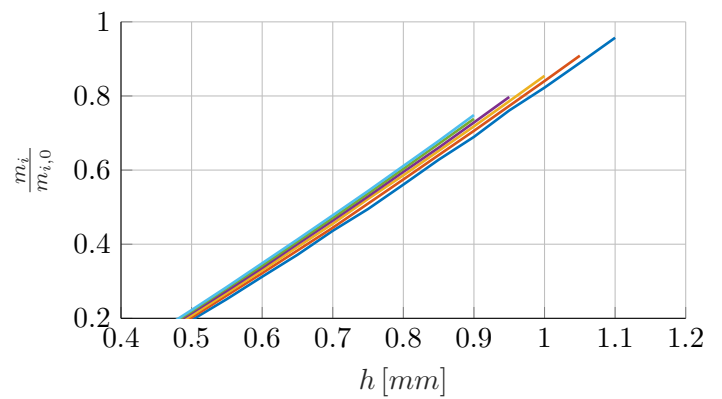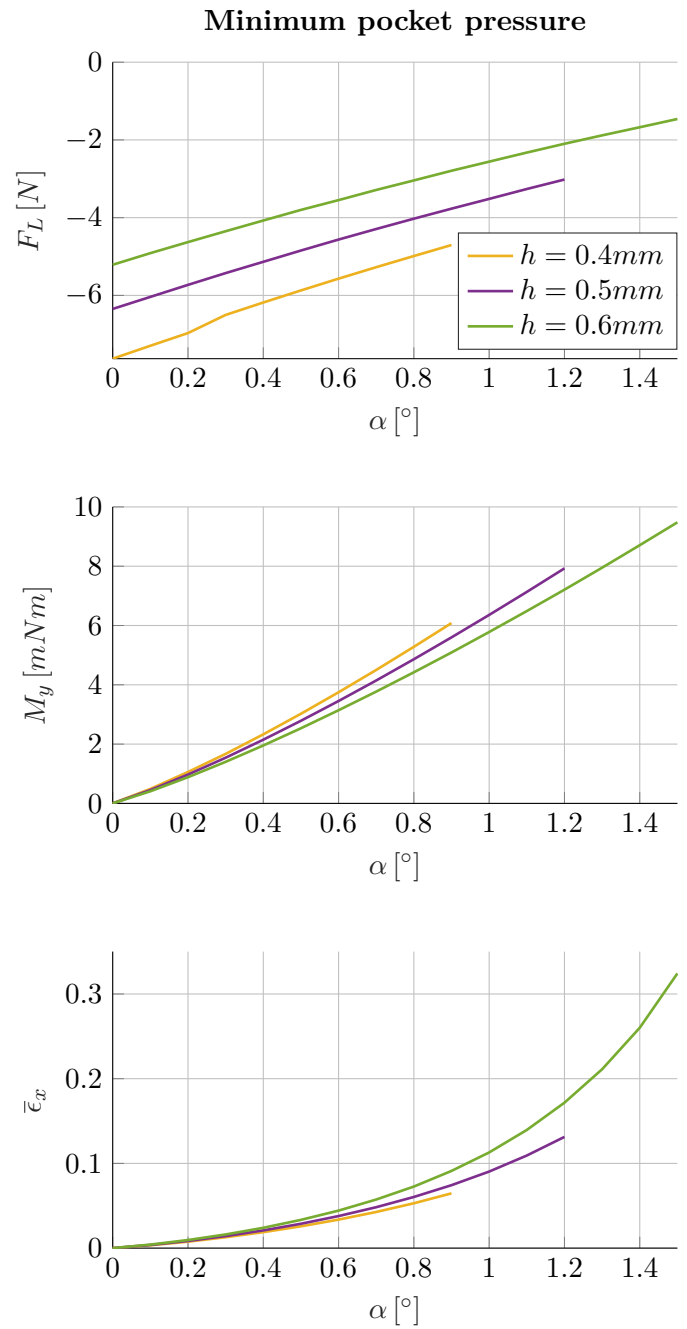
Figure A-8: This figure presents the load capacity, torque and eccentricity of the bearing for varying tilt angles and fly heights at minimum pocket pressure. The data corresponds to the data shown in Figure A-13, Figure A-14 and Chapter 2.
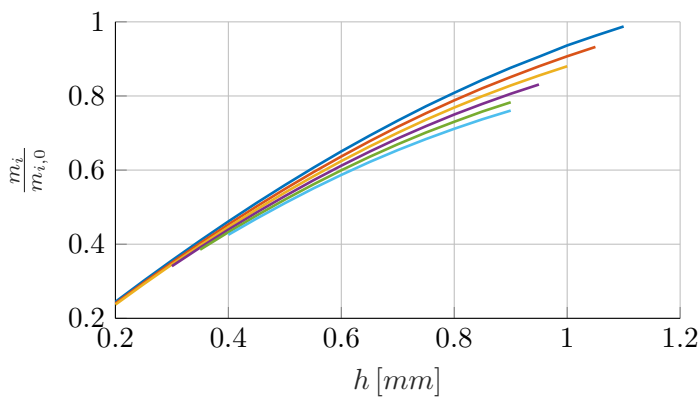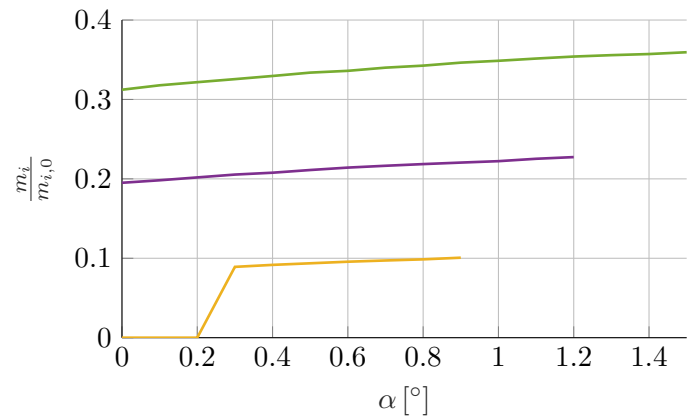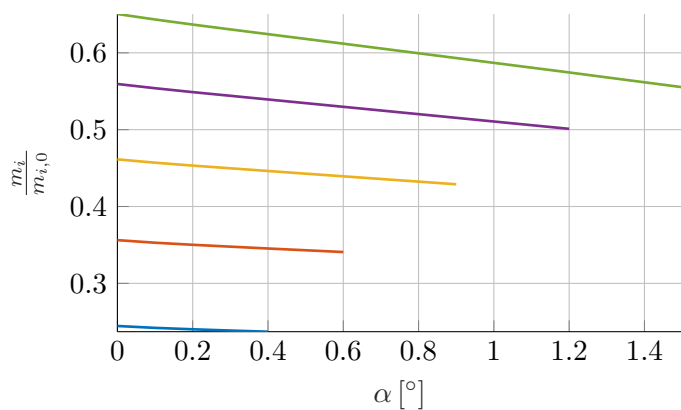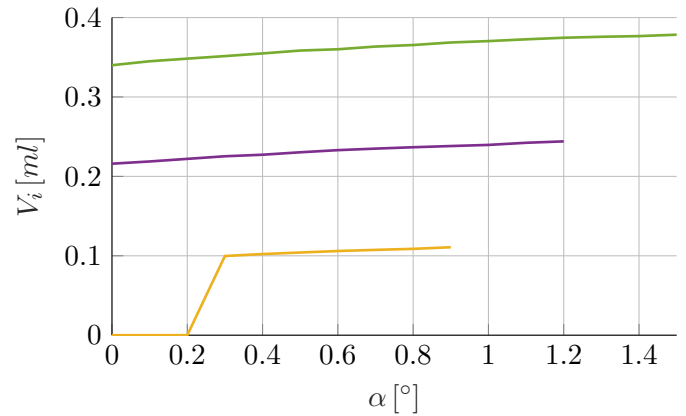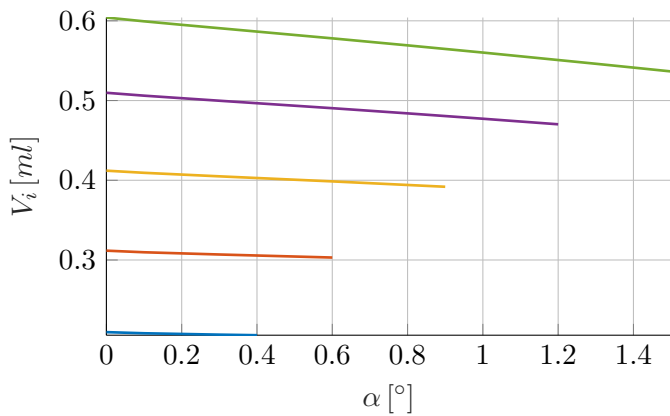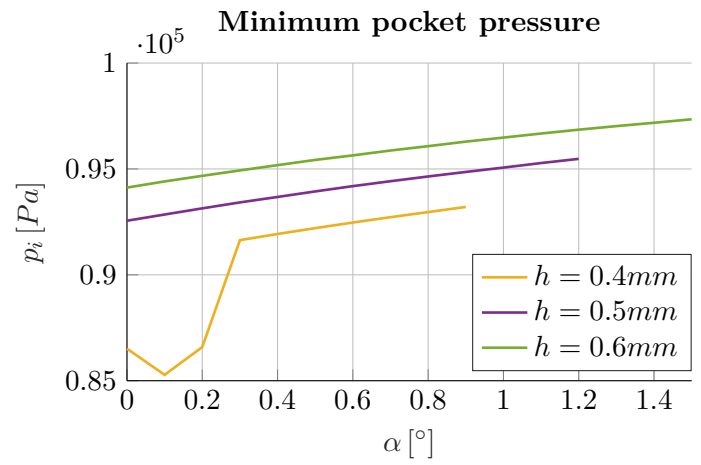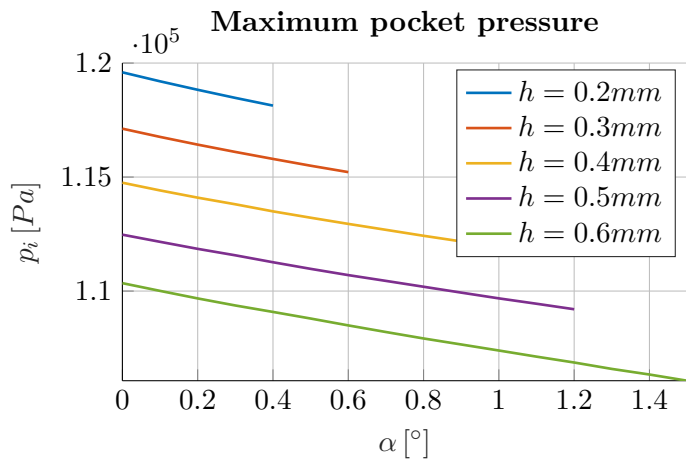
Figure A-9: This figure presents the pressure, volume and mass inside the pocket for varying tilt angles and fly heights at maximum pocket pressure. The data corresponds to the data shown in Figure A-11, Figure A-12 and Chapter 2.
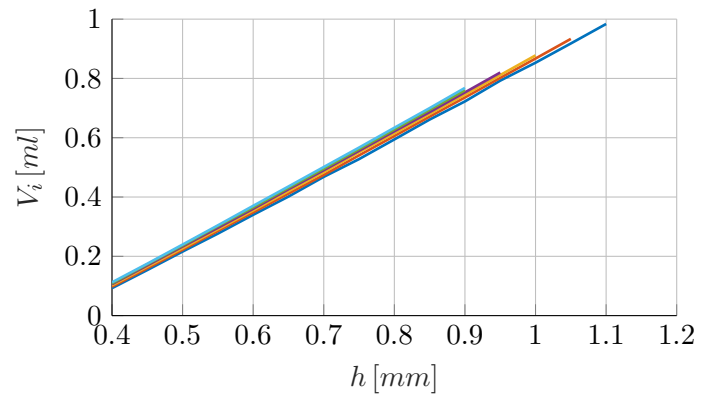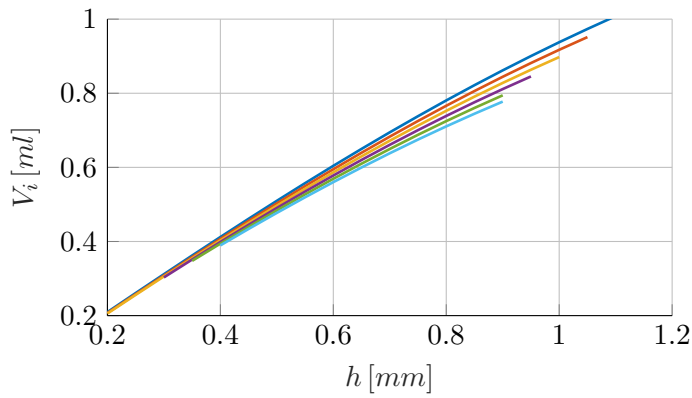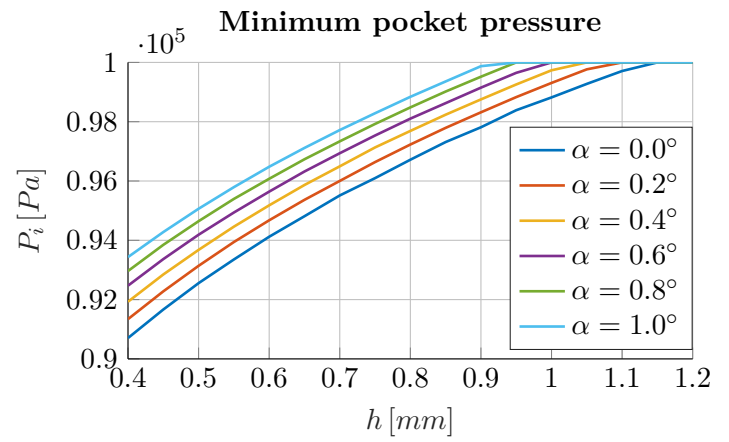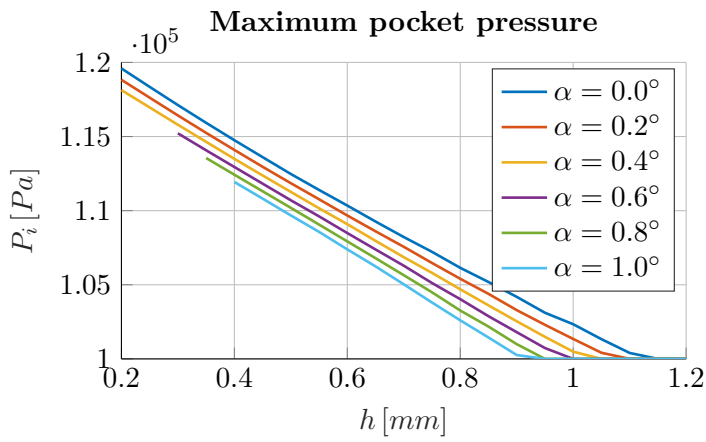
Figure A-10: This figure presents the pressure, volume and mass inside the pocket for varying tilt angles and fly heights at minimum pocket pressure. The data corresponds to the data shown in Figure A-13, Figure A-14 and Chapter 2.
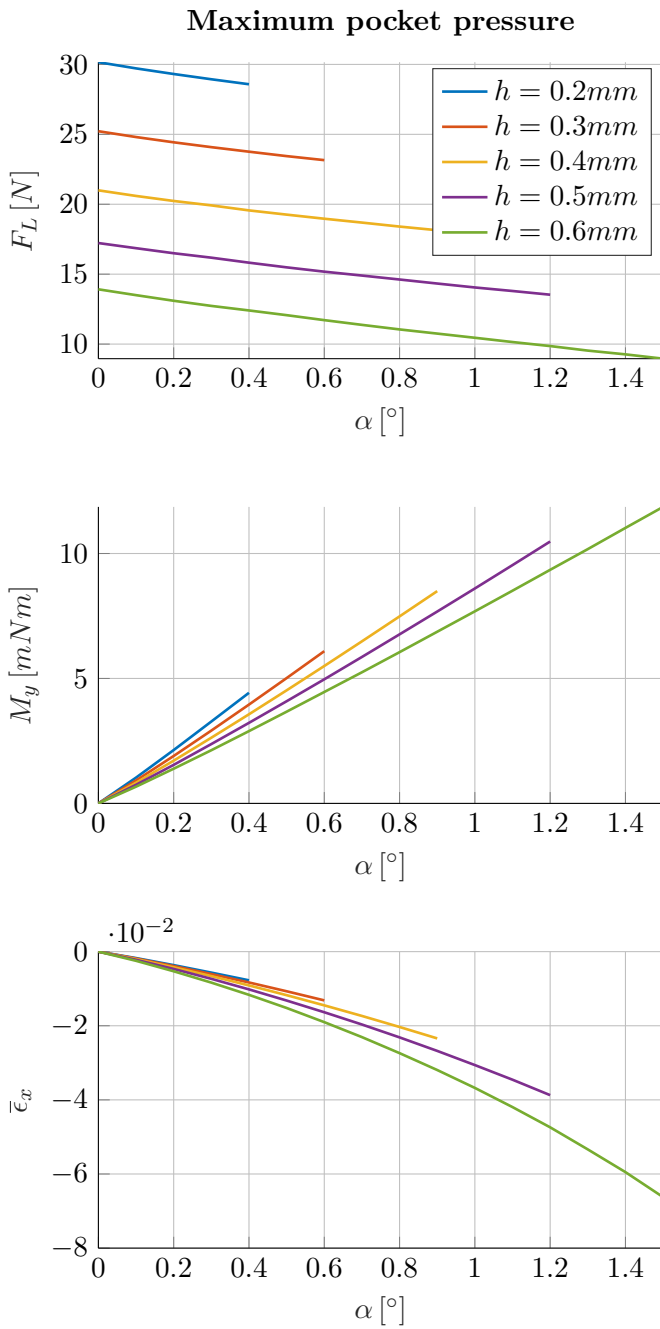
A-3   Tilted bearing: maximum pocket pressure

A-3-1   Pressure distribution
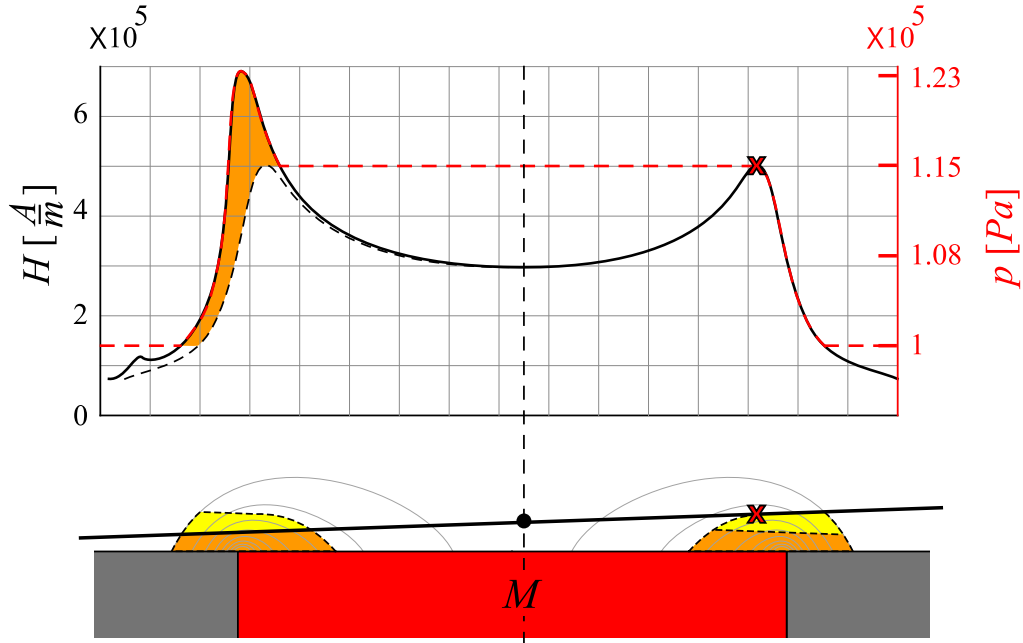
Figure A-11: This figure presents the cross-section of the tilted bearing at $\theta = 0°$ (Chapter 2) for maximum pressure inside the pocket. The top figure shows the pressure distribution acting on the plate (red) and the corresponding magnetic field (black).

A-3-2   Eccentricity
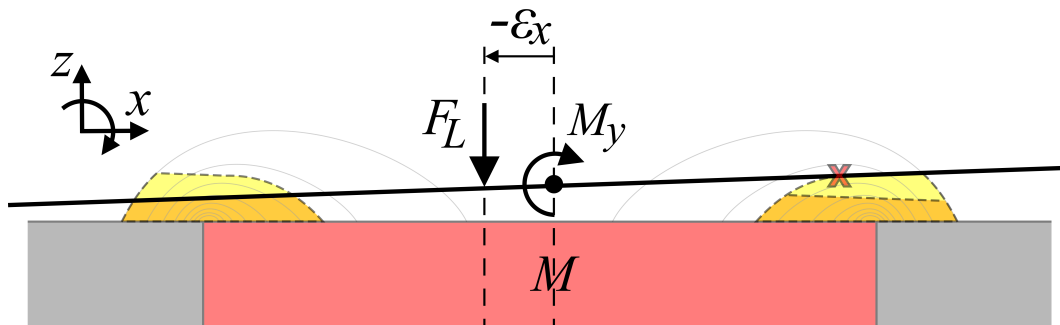
Figure A-12: This figure presents the cross-section of the tilted bearing at $\theta = 0°$ (Chapter 2) for maximum pressure inside the pocket. In the figure the resultant load capacity, torque and eccentricity are indicated in order to explain the data showed of this chapter.

A-4 Tilted bearing: minimum pocket pressure

A-4-1 Pressure distribution
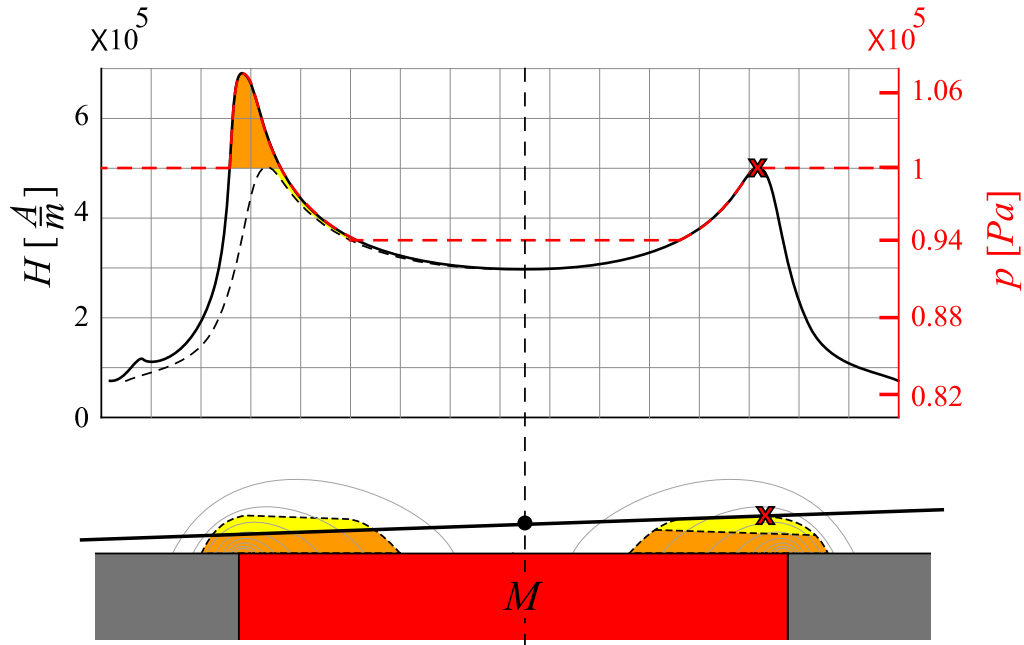
Figure A-13: This figure presents the cross-section of the tilted bearing at $\theta = 0°$ (Chapter 2) for minimum pressure inside the pocket. The top figure shows the pressure distribution acting on the plate (red) and the corresponding magnetic field (black).

A-4-2 Eccentricity
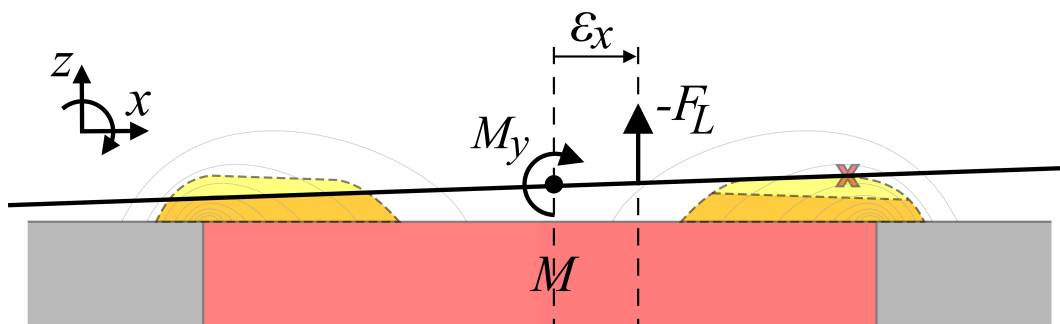
Figure A-14: This figure presents the cross-section of the tilted bearing at $\theta = 0°$ (Chapter 2) for minimum pressure inside the pocket. In the figure the resultant load capacity, torque and eccentricity are indicated in order to explain the data showed this chapter.

Additional figures paper: discussion

This section provides additional figures and information regarding the results shown in Chapter A. The additional results are presented in two different ways, since some characteristics of the bearing are better explained using one representation instead of the other. Moreover, the different representations can give different interesting insights in the behaviour of the bearing. Section A-1 shows the results with respect to the fly height, while Section A-2 shows the results with respect to the tilt angle. The load capacity, torque and eccentricity of the bearing will be discussed in the next sections.

B-1   Load capacity

Figure A-3 and Figure A-4 show the load capacity of the bearing with respect to the fly height. Figure A-7 and Figure A-8 show the load capacity with respect to the tilt angle. The behaviour of the load capacity will be explained using the scaled load capacities given in Figure A-1 and Figure A-2.

B-1-1   Discussion: maximum pocket pressure

It can be concluded from Figure A-1 that increasing the tilt decreases the load capacity of the bearing. At a fly height of $1mm$, the normalized load capacity significantly increases after which the increase gradually stagnates. For a tilt error of 0.6°, the load capacity of the bearing reduces approximately to 0.9 times the load capacity at perfect alignment.

Initially, the plate does not make contact with the ferrofluid. When the plate is lowered, at some fly height the plate makes initial contact. The height at which the plate makes the initial contact increases when the tilt angle increases. Note that a tilted plate has at that point already a small load capacity whilst the enclosed pocket is not established yet. (Load capacity due to the pressure inside the ferrofluid.) When the tilted plate has already a small load capacity, the aligned bearing has not, since there is still no contact. The result is that the scaled load capacity for maximum pocket pressure goes to infinity when approaching h_0, whereas the load capacity for minimum pressure goes to minus infinity. Moreover, due to tilt, the obtainable fly heights get limited. As an example, the lowest reachable fly height is approximately $0.4mm$ for a tilt angle of 1°.

B-1-2   Discussion: minimum pocket pressure

Figure A-2 shows the normalized load capacity for minimum pressure inside the pocket. The result is not much different from the normalized load for maximum pressure. Initially, the normalized load capacity significantly increases after which a constant value is reached, indicating the efficiency of the bearing for different tilt errors. The ferrofluid seal is as strong as its weakest link, which is the part furthest away from the magnet. Increasing the tilt

increases the distance to the magnet, which therefore diminishes the strength of the ferrofluid seal.

B-2 Torque

The positive tilt stiffness of the bearing showed in Chapter 2 is not entirely self-evident. Therefore, the observed behaviour will be explained and illustrated in this section by using the cross-section of the bearing and the corresponding pressure distribution (Figure A-11 and Figure A-13). The cross-section corresponds to $\theta = 0°$ in Chapter 2.

B-2-1 Discussion: maximum pocket pressure

Due to tilt, the pressure distribution that acts on the plate is asymmetric and results therefore in torque (Figure A-11). Chapter 2 explains how the pressure distribution is calculated. As discussed in the precious section, the strength of the seal is determined by its weakest link, which is denoted in Figure A-11 by the red x mark.

The torque is calculated by multiplying the pressure distribution that acts on the plate times its lever arm, and integrating it over the surface. The pressure distribution on the weaker (right) side is positive, therefore resulting in torque acting counter-clockwise. The pressure on the left side is also positive and results in torque acting clockwise. Summation results in the total torque. In order to visualize what happens, the pressure distribution of the weaker (right) side is mirrored and also displayed on the left side of the figure. The torques act in opposite directions, therefore partly neutralizing each other. The remainder results in torque acting on the plate. This resulting torque is indicated in orange in Figure A-11. Multiplying this remaining pressure distribution by its lever arm and integrating it, results in the total torque M_y.

The resulting torque acts opposite to the applied tilt for maximum pocket pressure. Decreasing the fly height increases the magnetic field intensity more on the already stronger side of the ferrofluid seal, therefore increasing the torque (Figure A-3 and Figure A-7). Moreover, increasing the tilt lowers the plate at the stronger side, increasing the pressure and torque even more. It can be concluded that the tilt stiffness of the bearing is positive for maximum pressure inside the pocket.

B-2-2 Discussion: minimum pocket pressure

The pressure distribution when the pressure inside the pocket is minimum, is presented in Figure A-11. Since the pressure inside the pocket is lower than the ambient pressure, the torque resulting from the right side of the bearing, acts in the clockwise direction. The pressure distribution on the left side is slightly more complex. The pressure inside the pocket is again lower than ambient pressure, therefore resulting in torque which acts counter-clockwise. However, the pressure inside the ferrofluid seal is partly lower (counter-clockwise torque) and partly higher (clockwise torque) than ambient pressure, therefore neutralizing each other partly. Summation results in the total torque. This is again visually expressed by mirroring the right side to the left side. The difference between the left and right pressure distribution (indicated in orange and yellow) results in the torque acting on the plate. The orange part results in a clockwise torque. The difference indicated in yellow also results in a torque acting in clockwise direction. In this part of the pressure distribution, both the pressure on the left side and right side are lower than ambient pressure, however the pressure on the left side is

higher than that on the left side. The right side "pulls" harder, thus the yellow part indicates a clockwise torque.

Increasing the tilt or decreasing the fly height increases the magnetic field intensity of the left seal again (Figure A-4 and Figure A-8). Therefore, the torque increases, resulting in a positive tilt stiffness. It can be concluded that the ferrofluid pocket bearing is self-aligning independent of the pressure inside the pocket. The torque always acts in opposite direction with respect to tilt.

B-3   Eccentricity

In this section, the tilt of the system and the resulting torque and load capacity will be presented, using a self-defined eccentricity (length scale). The eccentricity of the bearing is calculated according to Eq. (B-1). Next, the obtained eccentricity is scaled with respect to the radius of the magnet Eq. (B-2). The result is non-dimensional and indicates to what extent an off-center applied load can be handled by the bearing.

$$\epsilon_x = -\frac{M_y}{F_L} \tag{B-1}$$

$$\bar{\epsilon}_x = \frac{\epsilon_x}{R} \tag{B-2}$$

B-3-1   Discussion: maximum pocket pressure

Figure A-3 and Figure A-7 show the normalized eccentricities for the bearing with maximum pressure inside the pocket. At high fly heights, the air pocket is not yet enclosed by the seal but the plate does make partly contact with the ferrofluid seal. Therefore, the magnitude of the torque and load capacity are comparable, resulting in a normalized eccentricity nearing one. The off-center load can be applied almost at the edge of the magnet.

When the fly height is decreased, the load capacity significantly increases while the torque does not. This decreases the normalized eccentricity to almost zero for all tilt angles. Thus, the bearing can only handle a very small off-center applied load at lower fly heights. The negative sign indicates that the load is applied at a negative x coordinate (lower side of the tilted plate). Figure A-12 visually shows how the load capacity, torque and eccentricity relate to each other for maximum pressure inside the pocket.

B-3-2   Discussion: minimum pocket pressure

Figure A-4 and Figure A-8 show the normalized eccentricities for the bearing with minimum pressure inside the pocket. When the pocket is not yet completely enclosed, the load capacity and torque are both positive. Therefore, the eccentricity is nearing -1, as discussed in the previous section. When the pocket is completely enclosed, the torque remains positive but the load capacity becomes negative for minimum pocket pressure (pressure lower than ambient pressure). The eccentricity becomes positive. Figure A-14 visually shows how the load capacity, torque and eccentricity relate to each other for minimum pressure inside the pocket. Decreasing the fly height decreases the eccentricity again, resulting in an eccentricity of almost zero.

Appendix C

Performance tilted model

In this section, the performance of the tilted bearing model (Chapter 2) is presented. The performance is expressed in calculation time and relative error for varying mesh sizes (Physics-Controlled in COMSOL Multiphysics® [4]) and discretizations N. A mesh size of 1 resembles the "extremely fine" mesh size, while 9 presents the "extremely coarse" mesh size.

The average calculation time is given in Figure C-1. As expected, the time increases linearly with the number of discretizations. Moreover, the average calculation time also increases linearly for the mesh size except for a mesh size of 1. Then the calculation time doubles. The fminbnd algorithm in the Matlab® R2018a optimization toolbox [29], needs on average $\overline{N}_{ite} = 15.8 \pm 1.7(2\sigma)$ iterations to obtain the equilibrium position of the ferrofluid. Each iteration requires N calculations (number of discretizations).
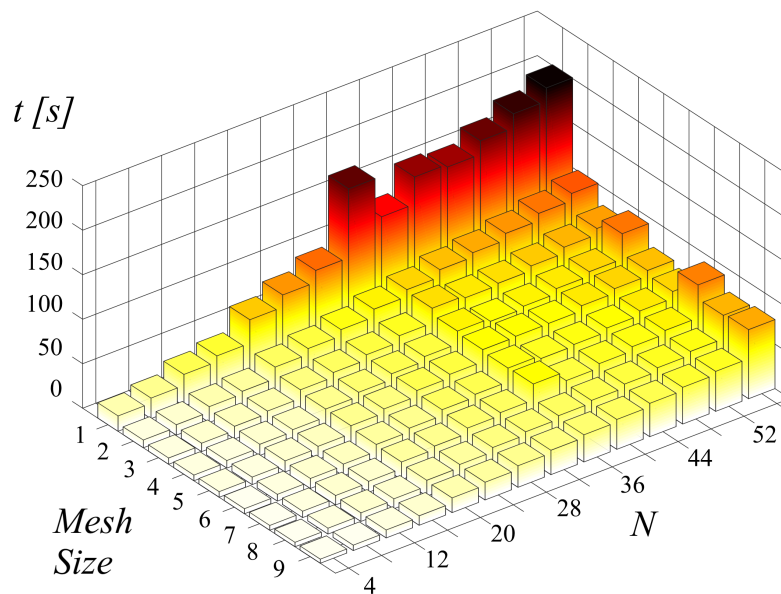
Figure C-1: This figure shows the average calculation time for different physics-controlled mesh sizes in COMSOL Multiphysics® and for different N (Chapter 2).

The torque of the bearing (M_y) showed to be the most sensitive to small variations in the calculated equilibrium position of the ferrofluid. Therefore, the relative error of M_y represent the total error of the calculation. Figure C-2 shows the relative error versus N. It can be concluded from the figure that the relative error is smaller than 0.5% when $N \geq 16$. Figure C-3 shows the error with respect to the mesh size. This figure shows that initially the error decreases when the mesh size is decreased. However, for a mesh size of 5 or below the error does not decrease any more. Since the calculation time increases when the mesh size decreases (Figure C-1), the optimum mesh size is found to be 5. To conclude, the calculations of the tilted bearing model will be performed with a physics-controlled mesh size of 5 and discretization of $N = 16$.
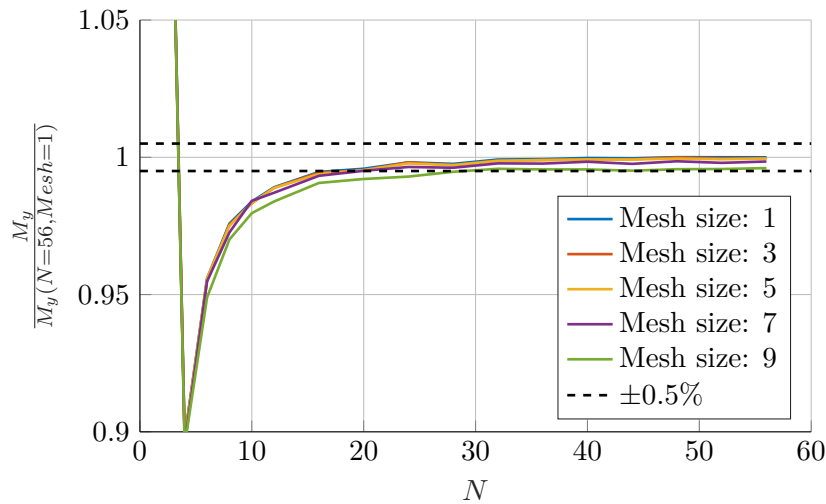
Figure C-2: This figure shows the relative error of M_y with respect to the number of discretizations N. The error is scaled with respect to the finest (and therefore assumed to be the most accurate) result, obtained using mesh size 1 and $N = 56$.
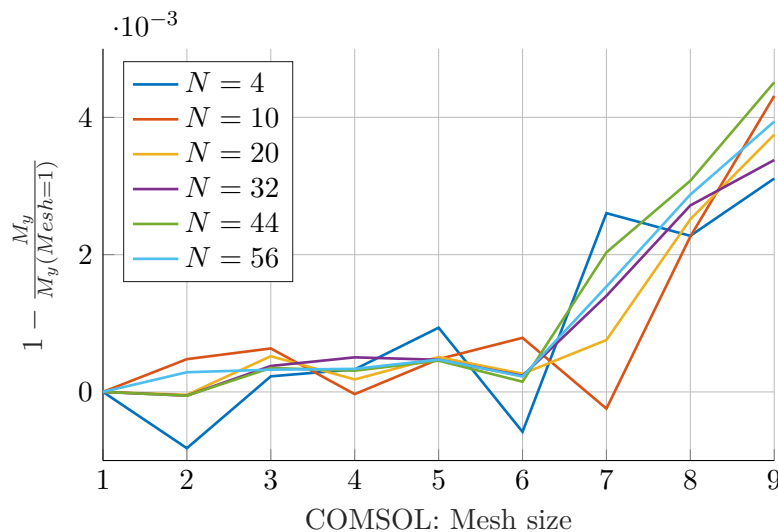
Figure C-3: This figure shows the relative error of M_y with respect to the mesh size. The error is scaled with respect to the result obtained using mesh size 1.

Appendix D

Laser triangulation measurements

The predicted stiffness of the ferrofluid bearing after almost all the air is pressed out of the pocket, is $\approx 0.5 \cdot 10^6 N/m$. Preliminary test results show that the stiffness of the test setup is approximately $\approx 2 \cdot 10^6 N/m$. Therefore, an additional laser triangulation sensor is implemented in order to check the displacement error caused by the limited stiffness of the testing machine. The tensile tester used in the measurements is the Zick/Roell Z005 and the added laser triangulation sensor is a Micro-Epsilon optoNCDT1402 (Chapter E).

The measuring range of the laser sensor starts at $20mm$ and ends at $25mm$. The values of the analog current output of the sensor that correspond to these two positions are $4mA$ and $20mA$. Next, the potential difference over a resistor of 511Ω, caused by the output current of the sensor, is sampled by a National Instruments USB-6211 between $-10V$ and $10V$, with a 16 bit ADC resolution. Using the measured potential and the value of the resistor, the current output of the sensor can be calculated using Ohm's Law. Then, using the specifications of the sensor, the current is converted to the displacement.

Due to the chosen value for the resistor, the potential difference over the resistor varies between $2.04V$ and $10.22V$. The analog input of the NI-DAQ saturates above $10V$. This effectively means that the laser sensor can measure displacements, ranging from $20mm$ to $24.9mm$, with a resolution of $0.187\mu m$. According to the data sheet, the force measurement of the Zwick has a relative accuracy of 0.21%, and a repeatability below 0.33%. The displacement has a repfeatability of $0.3\mu m$, and a accuracy of $0.6\mu m$.

Finally, the test setup can be seen in Figure D-1a. Note that the ferrofluid bearing is placed on top of an aluminium profile such that the head of the tensile tester is located in the measurable range of the laser triangulation sensor.

Initially, the head of the tensile tester is pressed into the test setup, meaning only the magnet and base plate without the presence of ferrofluid. This measurement is done in order to obtain both the stiffness of the test setup as well as to identify the location of the top surface of the magnet for both the tensile tester and laser sensor, h_0. Next, ferrofluid is added to the system and measurements are performed.

When the measurement starts, a single knock is given onto the aluminium head. This knock is detected by the tensile tester in the force measurement, see Figure D-1b. The small displacement of the aluminium head, caused by the knock, is also detected by the laser sensor, see Figure D-1d. Now, the data can be aligned in the time domain and the displacement measurements of the laser sensor and the tensile tester can be compared.

$$\epsilon = x_{laser} - x_{zwick} \tag{D-1}$$

(a)

(b)

(c)

(d)
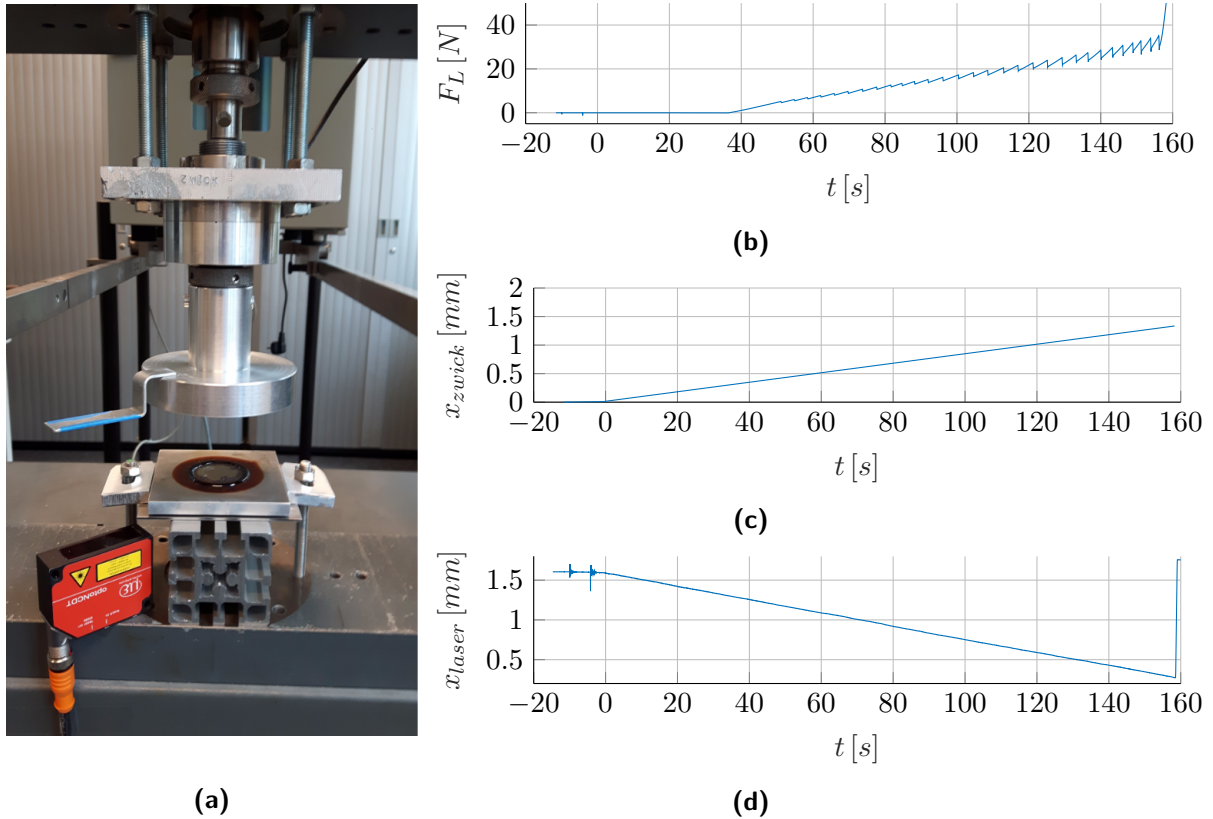
Figure D-1: This figure presents the test setup including the laser triangulation sensor in figure (a). Figure (b) shows the force measurement and figure (c) the displacement measurement during compression using the Zwick/Roell Z005. The additional displacement measurement using a laser triangulation sensor in combination with a NI DAQ is given in figure (d).
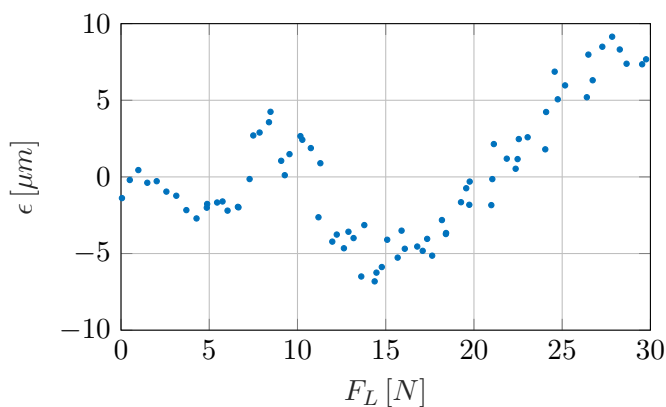
Figure D-2: The position error, the difference between the displacement measurements of the tensile testing machine and the laser triangulation sensor (Eq. (D-1)), versus the applied load.

The displacement error is defined in Eq. (D-1). The result of the measurement is given in Figure D-2. For an applied load of $30N$, the maximum displacement error stays below $10\mu m$. Therefore, it can be concluded that this error can be neglected with respect to the fly height of $\approx 1mm$ ($\leq 1\%$). It is important to note that the displayed error, is the error caused by the limited stiffness of the tensile tester. The combined stiffness of the magnet, the steel plate and the aluminium profile is still present and unknown, in both the measurements of the tensile tester and the laser sensor.

Appendix E

Data sheets

E-1   Zwick/Roell Z005

Kalibrierschein / *Calibration Certificate*

Kunde *Customer*	**Technische Universiteit Delft**	Ergebnisdatei *Result file*	**182823.kal**
Prüfer *Tester*	**Mohn**	Temperatur *Temperature*	**24.0 °C**
Kalibrierdatum *Date of calibration*	**22.07.2008**	AB-Nr. der Maschine *Machines AB no.*	**2152437**
Typ des Kraftaufnehmers *Type of load cell*	**KAF-TC**	Werk-Nr. der Maschine *Serial no. of the machine*	**182822**
Werk-Nr. Kraftaufnehmer *Load cells serial number*	**182823**	Anzeige *Display*	**PC**
Nennkraft *Nominal force*	**1000.000 N**	Auflösung a der Maschine *Machines resolution a*	**0.42% bei 0.2% FN**

Verwendete Gebrauchsnormale und Prüfgeräte:
Working standards and test devices used:

> **Belastungskörpersatz Nr.02**
> **Digitalkompensator DK 38, Nr. 53374**
> **Kraftaufnehmer 2kN, Nr. 102130042**

Wir bestätigen hiermit, daß der oben beschriebene Kraftaufnehmer kalibriert wurde.
Die gemessenen Werte der Kraftmesseinrichtung liegen innerhalb der zulässigen Abweichungen
nach DIN EN ISO 7500-1. Die jeweilige Messunsicherheit ist mit zweifacher Standardabweichung bei jeder
Stufe angegeben. Die Kraftmesseinrichtung kann in den geprüften Meßbereichen wie folgt eingesetzt werden:

We hereby confirm that the above named load cell has been calibrated.
The force measurement devices measured values are within the permissilble tolerances according to DIN EN ISO 7500-1
The measuring uncertainity is given at each step considered with a double standard deviation. The force
measurement device can be put to use as follows in the tested measurement ranges.

> **DIN EN ISO 7500-1 Klasse 1 (2.00 N ... 1.00 kN)**
> **DIN EN ISO 7500-1 Klasse 0.5 (10.00 N ... 1.00 kN)**

Für die Einhaltung der angemessenen Frist zur Wiederholung der Kalibrierung ist der Benutzer
verantwortlich. Wir verweisen auf die Norm DIN 51220 und auf die speziellen Prüf- und Kalibriernormen.

The user is responsible for keeping to an appropriate deadline for the repetition of calibration.
We draw standard DIN 51220, and the special test and calibration standards to you attention

Dies ist ein elektronisch erstelltes Dokument, welches ohne Unterschrift gültig ist
This is an electronically created documnet and is therefore valid without signature.

Ergebnisse Zug / results tensile :

wahrer Wert *real Value*	Maschinenanzeige *Machine display*	relative Anzeigeabweichung *rel. accuracy*	relative Wiederholpräzision *rel. repeatability*	relative Umkehrspanne *rel. reversibility*	relative Messunsicherheit *rel. uncertainity*
2.000 N	1.999 N	-0.05 %	0.24 %	-0.04 %	0.35 %
5.000 N	4.999 N	-0.02 %	0.05 %	-0.07 %	0.23 %
10.000 N	9.990 N	-0.10 %	0.03 %	-0.07 %	0.21 %
20.000 N	20.006 N	0.03 %	0.03 %	-0.02 %	0.20 %
50.000 N	50.015 N	0.03 %	0.01 %	-0.01 %	0.20 %
100.000 N	100.040 N	0.04 %	0.01 %	0.00 %	0.20 %
99.907 N	100.000 N	0.09 %	0.28 %	-0.39 %	0.20 %
199.980 N	200.000 N	0.01 %	0.39 %	-0.02 %	0.26 %
400.200 N	400.000 N	-0.05 %	0.09 %	0.06 %	0.12 %
599.920 N	600.000 N	0.01 %	0.02 %	0.03 %	0.12 %
799.830 N	800.000 N	0.02 %	0.09 %	-0.07 %	0.12 %
1.000 kN	1.000 kN	-0.01 %	0.07 %	-0.01 %	0.12 %

Ergebnisse Druck / results compression :

wahrer Wert *real Value*	Maschinenanzeige *Machine display*	relative Anzeigeabweichung *rel. accuracy*	relative Wiederholpräzision *rel. repeatability*	relative Umkehrspanne *rel. reversibility*	relative Messunsicherheit *rel. uncertainity*
2.000 N	2.004 N	0.21 %	0.33 %	-0.53 %	0.37 %
5.000 N	5.005 N	0.11 %	0.18 %	-0.18 %	0.25 %
10.000 N	10.009 N	0.09 %	0.06 %	-0.09 %	0.21 %
20.000 N	20.029 N	0.14 %	0.06 %	-0.03 %	0.21 %
50.000 N	50.023 N	0.05 %	0.04 %	0.01 %	0.20 %
100.000 N	100.020 N	0.02 %	0.02 %	0.01 %	0.20 %
100.400 N	100.000 N	-0.40 %	0.40 %	-0.06 %	0.27 %
200.180 N	200.000 N	-0.09 %	0.25 %	0.04 %	0.17 %
400.250 N	400.000 N	-0.06 %	0.11 %	0.10 %	0.12 %
600.040 N	600.000 N	-0.01 %	0.07 %	0.10 %	0.12 %
800.540 N	800.000 N	-0.07 %	0.01 %	-0.03 %	0.12 %
999.900 N	1.000 kN	0.01 %	0.04 %	0.05 %	0.12 %

E-2   Micro-Epsilon optoNCDT1402

Functional Principle, Technical Data

3.3   Technical Data ILD 1402-x

Model	ILD	1402-5	1402-10	1402-20	1402-50	1402-100	1402-200	1402-250VT	1402-400	1402-600
Measuring range	mm	5	10	20	50	100	200	250	400	600
Start of range	mm	20	20	30	45	50	60	100	200	200
Midrange	mm	22,5	25	40	70	100	160	225	400	500
End of range	mm	25	30	50	95	150	260	350	600	800
Linearity	μm	5 ... 9	5 ... 18	7 ... 36	12 ... 90	20 ... 180	40 ... 360	50 ... 1200	120 ... 2000	120 ... 3000
		≤ 0.18 % FSO						≤ 0.5 % FSO		
Resolution	Averaged over 64 values, μm	0.6	1	2	5	10	13	32	80	80
	dynamic, μm	1 ... 3	2 ... 5	5 ... 10	6 ... 25	12 ... 50	13 ... 100	32 ... 300	80 ... 480	80 ... 600
	1.5 kHz	0.02 ... 0.05 % FSO						0.02 ... 0.12 % FSO		
	digital	14 bit								
Measurement rate, programmable		1.5 kHz; 1 kHz; 750 Hz; 375 Hz; 50 Hz								
Light source		Semiconductor laser 1 mW, 670 nm (red)								
Laser class		Class 2 (II) acc. to IEC 60825-1: 2007								
Spot diameter	SMR, μm	110	110	210	1100	1400	2300	5000	2.6 x 5 mm	2.6 x 5 mm
	MR, μm	380	650	530	110	130	2200	5000	2.6 x 5 mm	2.6 x 5 mm
	EMR, μm	650	1200	830	1100	1400	2100	5000	2.6 x 5 mm	2.6 x 5 mm
Protection class		IP 67								
Vibration		15 g / 10 Hz ... 1 kHz						20 g / 10 Hz ... 1 kHz	15 g/ 10 Hz ... 1 kHz	
Shock		15 g / 6 ms (DIN EN 60068-2-29)								
Weight (without cable)		approx. 83 g						approx. 130 g		
Temperature stability		0.03 % FSO/°C					0.08 % FSO/°C			
Operation temperature		0 ... 50 °C								

Functional Principle, Technical Data

Model	ILD	1402-5	1402-10	1402-20	1402-50	1402-100	1402-200	1402-250VT	1402-400	1402-600
Storage temperature		-20 °C ... 70 °C								
Measurement value output	analog	4 ... 20 mA 12 bit (1 ... 5 V with cable PC 1402-3/U) or								
	digital	RS422								
Supply		11 ... 30 VDC, typical 24 VDC / 50 mA								
Controller		integral signal processor								
Elektromagnetic compatibility (EMC)		EN 61 326-1: 2006-10 DIN EN 55011: 2007-11 (Group 1, class B) EN 61000-6-2: 2006-03								

The specified data apply to a white, diffuse reflecting surface (Reference: Ceramic).
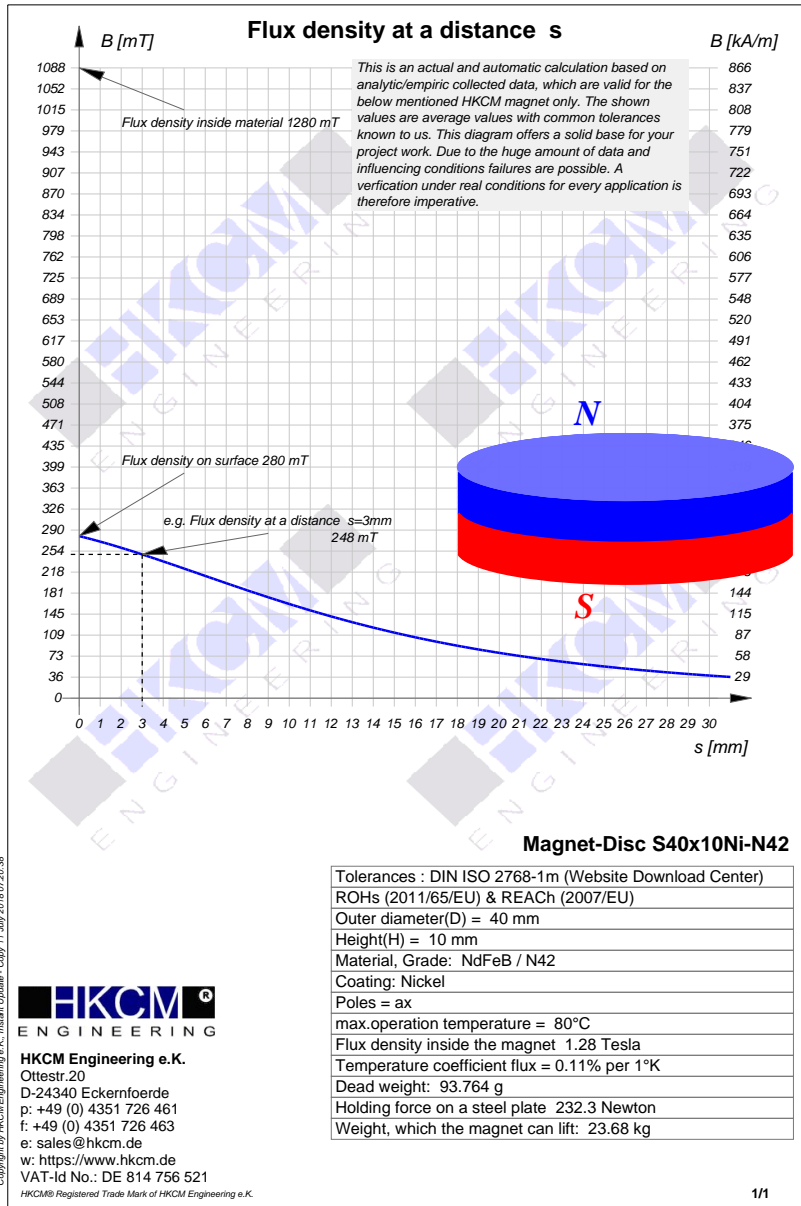FSO = Full Scale Output
SMR = Start of measuring range   MMR = Midrange   EMR = End of measuring range
ILD1402-250VT: 20 g, especially shock and vibration-resistant design for use on motor vehicles

E-3   HKCM 9961-835

Flux density at a distance s

This is an actual and automatic calculation based on analytic/empiric collected data, which are valid for the below mentioned HKCM magnet only. The shown values are average values with common tolerances known to us. This diagram offers a solid base for your project work. Due to the huge amount of data and influencing conditions failures are possible. A verfication under real conditions for every application is therefore imperative.

Flux density inside material 1280 mT

Flux density on surface 280 mT

e.g. Flux density at a distance s=3mm
248 mT

Magnet-Disc S40x10Ni-N42

Tolerances : DIN ISO 2768-1m (Website Download Center)	
ROHs (2011/65/EU) & REACh (2007/EU)	
Outer diameter(D) = 40 mm	
Height(H) = 10 mm	
Material, Grade: NdFeB / N42	
Coating: Nickel	
Poles = ax	
max.operation temperature = 80°C	
Flux density inside the magnet 1.28 Tesla	
Temperature coefficient flux = 0.11% per 1°K	
Dead weight: 93.764 g	
Holding force on a steel plate 232.3 Newton	
Weight, which the magnet can lift: 23.68 kg	

HKCM Engineering e.K.
Ottestr.20
D-24340 Eckernfoerde
p: +49 (0) 4351 726 461
f: +49 (0) 4351 726 463
e: sales@hkcm.de
w: https://www.hkcm.de
VAT-Id No.: DE 814 756 521
HKCM® Registered Trade Mark of HKCM Engineering e.K.

Copyright by HKCM Engineering e.K. Instant Update - Copy 11 July 2018 07:20:38

All calculations, diagrams and drawings are computed automatically and should not be used as the sole source of design data. The factors of your application may change these values considerably. All details are subject to alterations at any time.
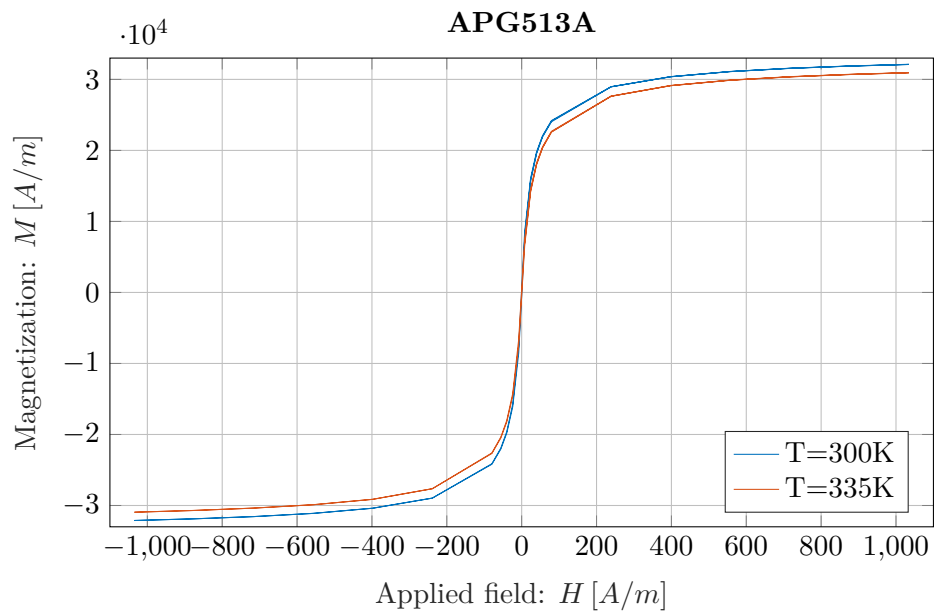
1/1

E-4 Ferrotec APG513A: MH Curve

Figure E-1: This figure shows the measured magnetization of the ferrofluid versus the applied field for two different temperatures.

Additional measurements: mass loss

F-1 Number of zig-zags

The load capacity of the ferrofluid bearing is measured for different velocities using a tensile testing machine. The stiffness of the test setup (Figure F-1), using the acrylate plate, is approximately $1.5 \cdot 10^6 N/m$ and the applied volume of ferrofluid is $0.28ml$ (Ferrotec APG513A). The results of the measurements for four different velocities are showed in Figure F-2. In this figure, the individual zig-zags are identified and the local stiffness of the bearing is calculated. Next, the number of zig-zags is given in Figure F-3 in a histogram. Moreover, the number of zig-zags is shown versus the velocity in a semi-logarithmic plot, Figure F-4.
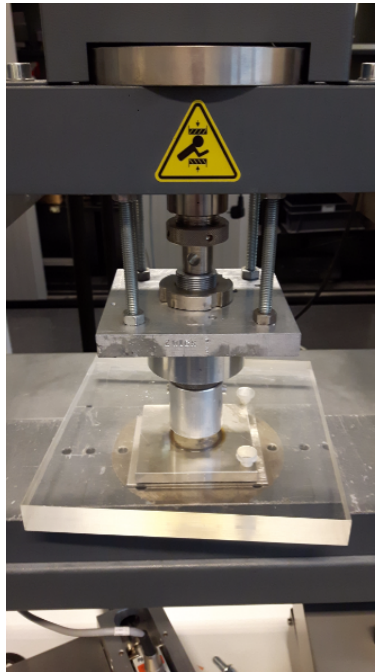

Figure F-1: This figure shows the test setup. The magnet, HKCM 9961-835, is placed on top of a steel base plate and is enclosed by an aluminium casing which prevents the ferrofluid from dripping. The test setup is used to see how the behaviour of the ferrofluid bearing is influenced by the velocity of the compression.
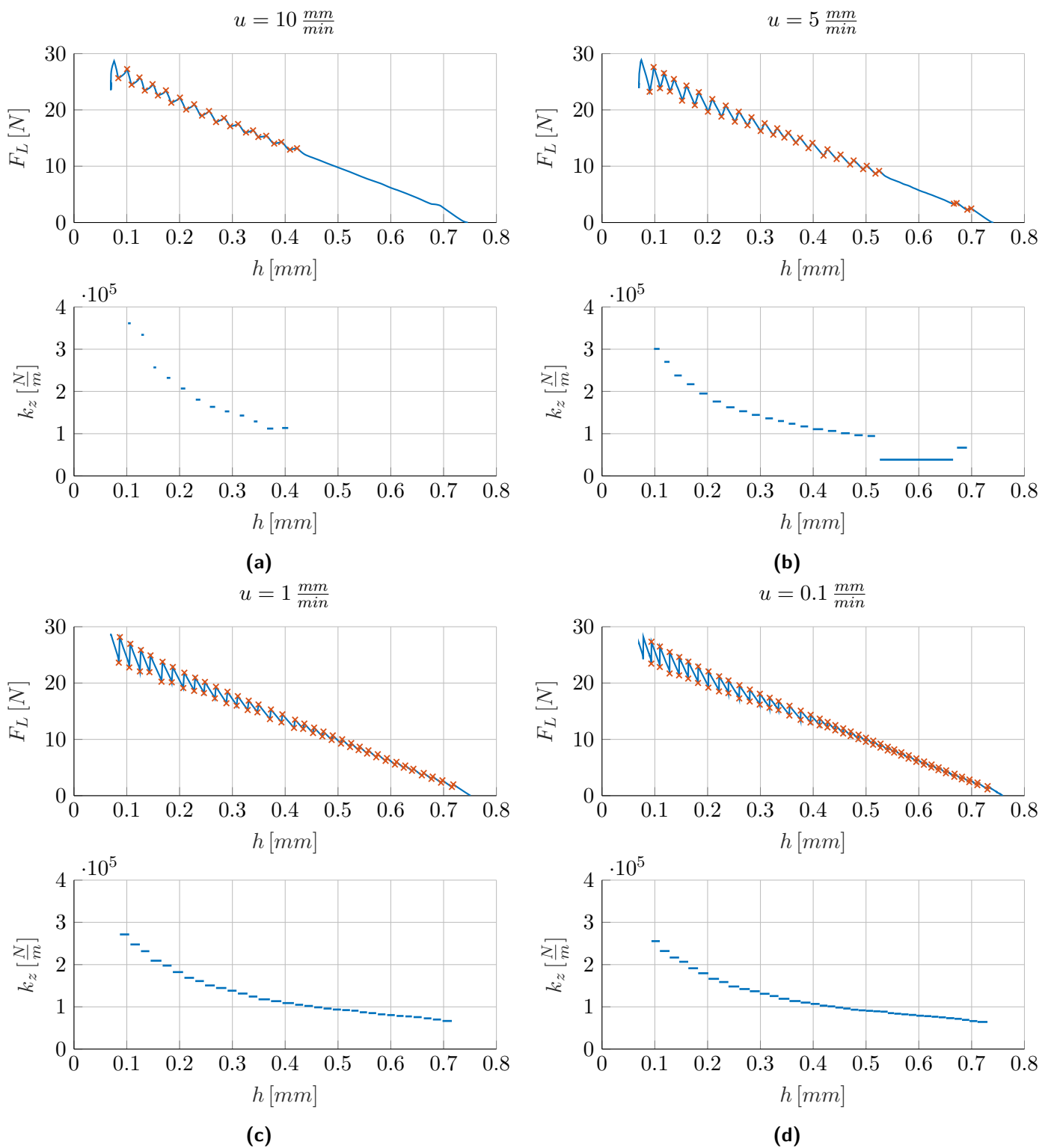
Figure F-2: This figure presents the measured load capacity and calculated stiffness of the ferrofluid bearing versus the fly height for different velocities.
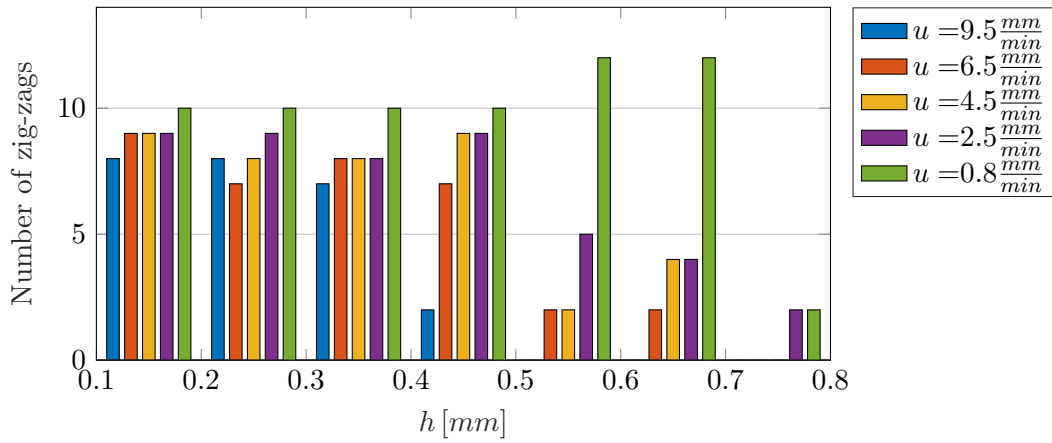
Figure F-3: This figure presents the number of zig-zags during compression of the bearing versus the fly height in a histogram.
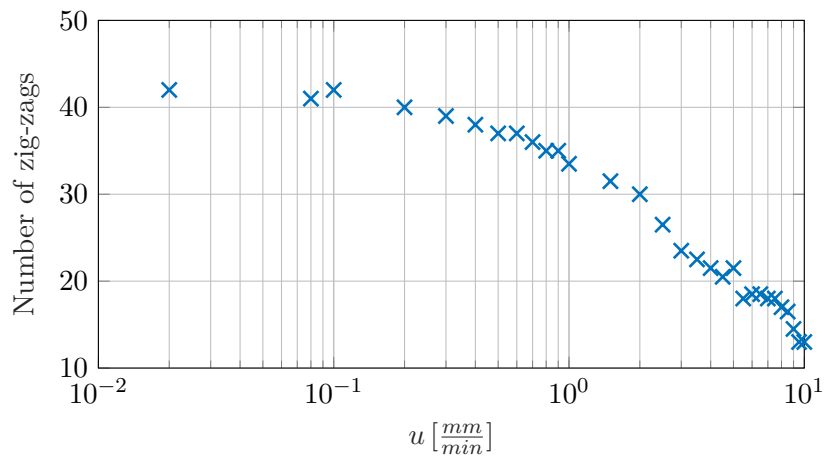
Figure F-4: The number of zig-zags is now presented with respect to the downwards velocity of the tensile testing machine. A semi-logarithmic scale is used for the horizontal axis.

F-2 Mass loss

Assuming that the mass inside the air pocket can be described by the ideal gas law, the mass loss for each zig-zag can be calculated according to Eq. (F-1). Both the pressure and the volume of the pocket change when mass is lost during a single zig-zag. However, Figure F-2 shows that the fly height does not change significantly before and after a zig-zag, namely $\Delta h_{zig-zag} \ll 0.01mm$ thus $\Delta h_{zig-zag} \ll h$. Therefore the change in volume of the pocket is negligible with respect to the total volume of the pocket. The volume of the pocket is approximated as a cylinder, $V_i \approx \pi r_i^2 h$. The other parameters in Eq. (F-1) are the universal gas constant $R = 8.314 \frac{J}{Kmol}$, the molar mass of air $M = 28.96 \frac{g}{mol}$ and the temperature $T = 293K$. Lastly, the pressure jump Δp is approximated by dividing the measured force jump ΔF, by the area of the bearing, assumed to be constant as $\pi (0.02)^2$.

$$\Delta m \approx \Delta p_i V_i \frac{M}{RT} \tag{F-1}$$

The calculated mass loss is showed in Figure F-5 for different fly heights and for a couple of compression velocities. Figure F-6 shows the calculated mass loss for all the performed measurements. The figure includes a boxplot for different height intervals. When the velocity of the tensile testing machine is sufficiently high, the zig-zag pattern found in the measurements is not nicely defined anymore, see Figure F-2. The mass loss seems to be continuous for those velocities. Therefore, the velocity range shown in Figure F-6 is reduced in figures Figure F-7 and Figure F-8, in order to gain more insight. Note that the ideal gas law assumes isothermal processes, which is not necessarily the case for higher velocities.

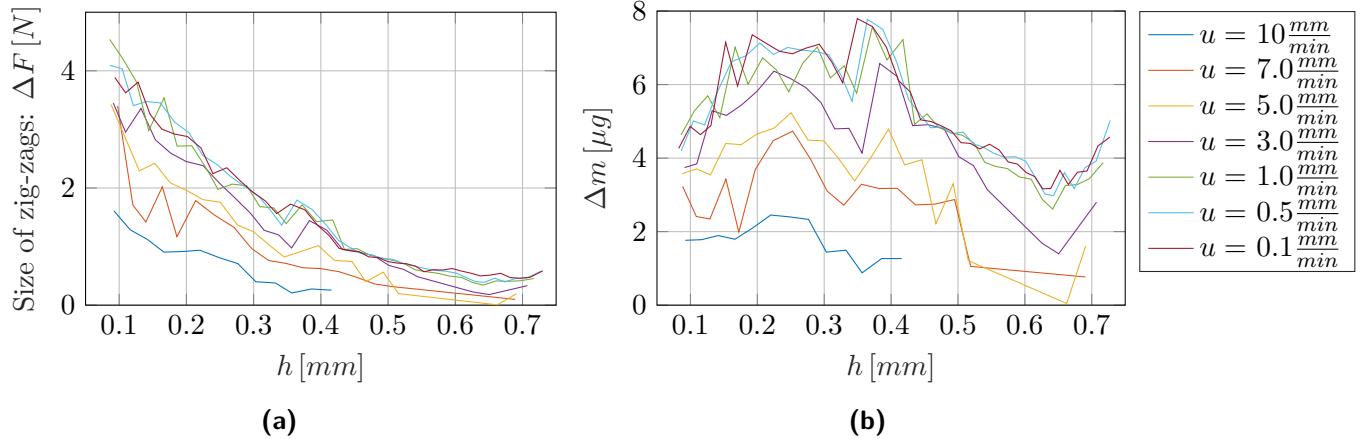**Figure F-5:** Figure (a) presents the change in load capacity due the zig-zags versus the fly height for different velocities. This jump in load capacity is used, in combination with the ideal gas law, in order to calculate the mass loss during compression. Figure (b) presents the mass loss versus the fly height.
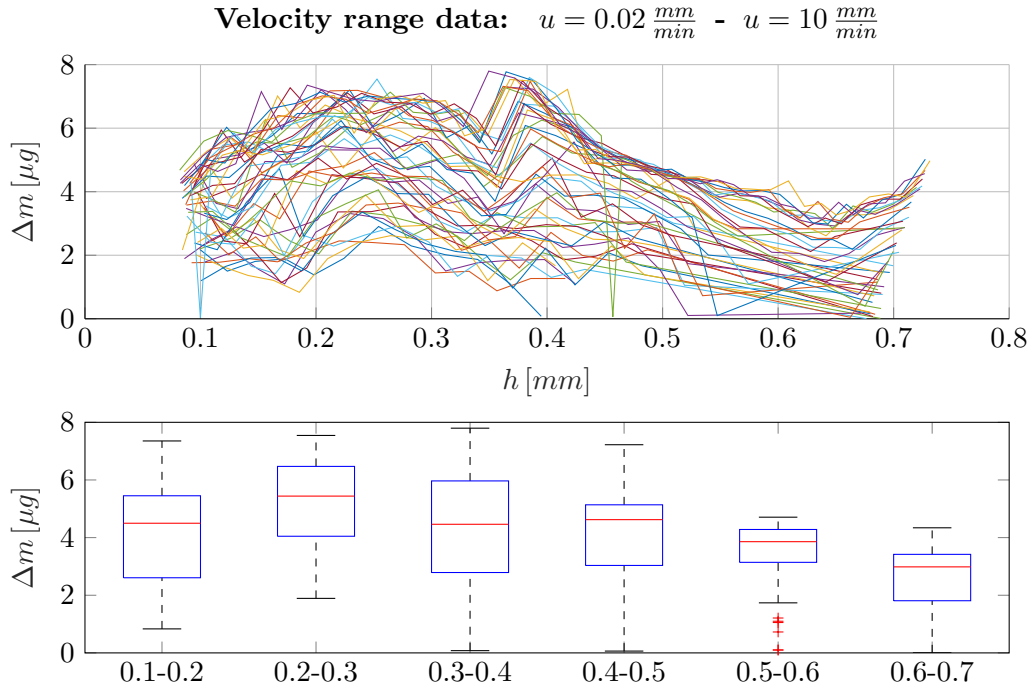
Figure F-6: The top figure presents the mass loss versus the fly height for different velocities, ranging from $0.02\frac{mm}{min}$ until $10\frac{mm}{min}$. The mass loss given in the top figure is presented in a boxplot in the bottom figure. In this figure, the central red line indicates the median, while the box indicates the 25th and 75th percentile. By default, the whiskers correspond approximately to 2.7σ in Matlab$^{®}$ R2018a, if the are distributed normally [28].

When the velocity of the tensile testing machine is sufficiently slow, the mass escaping out of the pocket seems to be constant from approximately $h = 0.2mm$ until $h = 0.4mm$, Figure F-8. Initially, less mass escapes out of the pocket, $h > 0.4mm$.

From this data, it cannot be concluded with certainty whether the mass of the escaping air is constant or its volume, or that neither one properly describes the observed behaviour. It is recommended for further research that instead of only measuring the load capacity of the bearing versus the fly height, the pressure inside the pocket gets also measured. Then, Δp does not have to approximated by dividing ΔF over a constant area. The area of the pocket is not constant but changes continuously during the measurement.

Figure F-7: The top figure presents the mass loss versus the fly height for different velocities, but this time the velocity range is narrowed, ranging from $0.02\frac{mm}{min}$ until $5mm\frac{mm}{min}$. The mass loss given in the top figure is shown in a boxplot in the bottom figure.
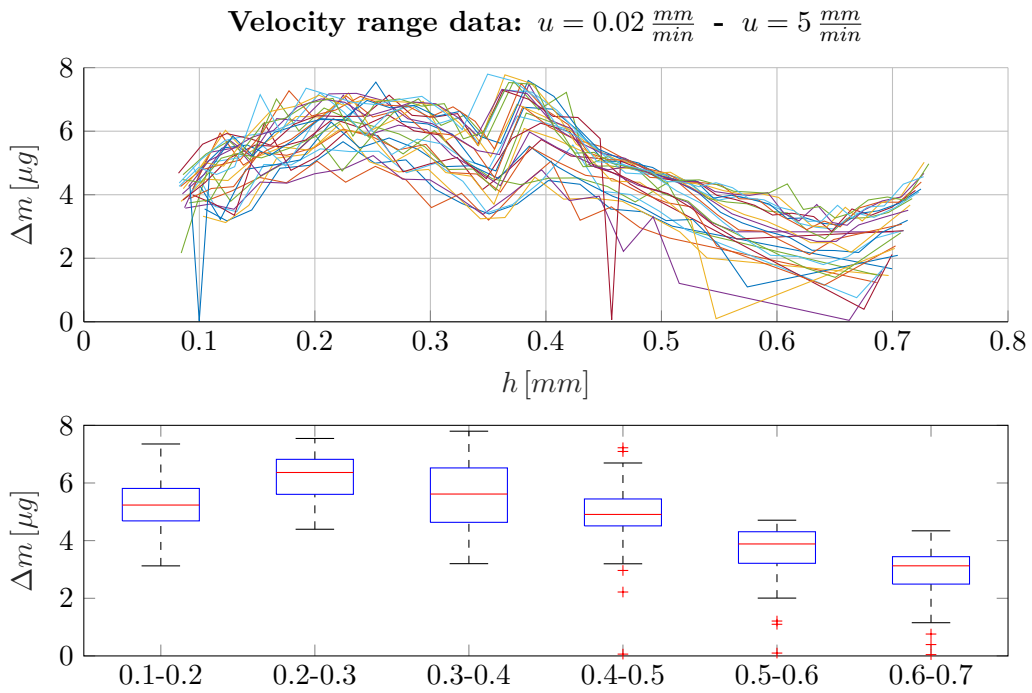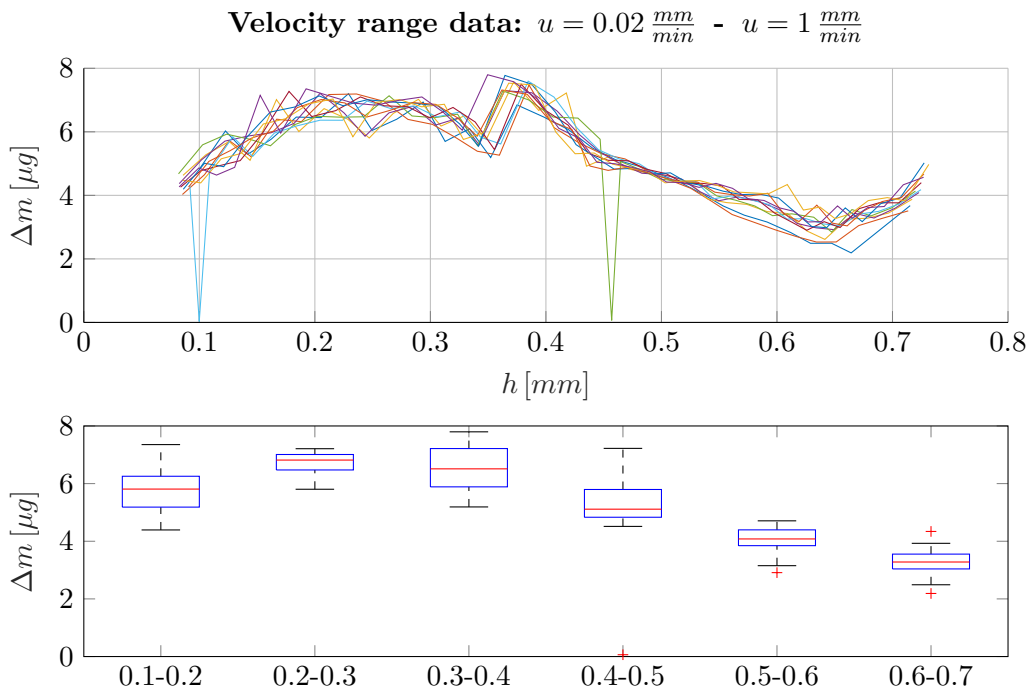

Figure F-8: The top figure presents the mass loss versus the fly height for different velocities, but this time the velocity range is even narrower, ranging this time from $0.02\frac{mm}{min}$ until $1mm\frac{mm}{min}$. The mass loss given in the top figure is shown in a boxplot in the bottom figure.

Appendix G

Ferrohydrodynamics

A ferrofluid is a colloidal suspension of nanometer sized particles ($3 - 15nm$). The magnetic particles, which are often covered with an atomic layer of dispersant, give the fluid paramagnetic properties [32]. To keep a ferrofluid colloidally stable, agglomeration of the magnetic nanoparticles and settling of the particles under the influence of gravity must be prevented. When the dimensions of the suspended particles are sufficiently small, the thermal energy (Brownian motion) of the particles can overcome the settling velocity determined by Stokes's formula [37]. Coating the magnetic particles prevents agglomeration. Ferrofluids can be categorized in two different groups according to their coating: ionic and surfaced. Stability in ionic coated ferrofluids is obtained using electrically charged nanoparticles. Commonly used particles are maghemites and ferrites. Surfaced coatings prevent agglomeration of particles by steric repulsion [39]. Ferrohydrodynamics became the established name for studying the hydrodynamics of these magnetic suspensions [40].

G-1 Ferrohydrodynamic Navier-Stokes equations

The pressure distribution inside a ferrofluid seal is derived from the ferrohydrodynamic Navier-Stokes equations for incompressible Newtonian magnetic fluids with constant viscosity, given in Eq. (G-1) [36][37]. The assumption of a Newtonian fluid is only valid when the particles in the colloidal suspension are sufficiently small, such that the surfactant's Van der Waals force [40] or the ionic coatings steric repulsion [39] prevents agglomeration of particles, which results in a fluid with constant viscosity. Moreover, the calculation of the magnetic body force (f_m), using only the magnitudes of the magnetization (M) and the gradient of the applied magnetic field (H), is only valid when the magnetization of the fluid is in the same direction as the applied magnetic field and when the fluid is electrically non-conducting [32].

$$\rho \left(\frac{\partial \underline{u}}{\partial t} + \underline{u} \cdot \nabla \underline{u} \right) = -\nabla p^* + \eta \nabla^2 \underline{u} + \rho \underline{g} + \underbrace{\mu_0 M \nabla H}_{f_m} \tag{G-1a}$$

$$\nabla \cdot \underline{u} = 0 \tag{G-1b}$$

Eq. (G-1) is a statement of conservation of mass and momentum. In these equations the dynamic viscosity is denoted by η, the density of the fluid by ρ, the velocity vector by $\underline{u}$, the composite pressure by p^*, the permeability of free space μ_0 and the gravitational acceleration by $\underline{g}$. Note that in the Navier-Stokes equations for magnetic fluids given by Rosensweig et al, the pressure, p, is replaced by a composite pressure, p^* (Eq. (G-2)) [37]. The total composite pressure is calculated by summation of the thermodynamic pressure found in the general Navier-Stokes equations ($p(\rho, T)$), the Magnetostrictive pressure (p_s) and the

fluid-magnetic pressure (p_m). The magnetostrictive pressure is related to a property of ferro-magnetic materials: magnetostriction. Magnetostriction is the volume change of a material due to magnetization and was first observed by Joule in 1842 [19]. Shliomis [40] published the ferrohydrodynamic Navier-Stokes equations without the magnetostrictive pressure and the fluid-magnetic pressure. Therefore, only the magnetic body force is added to the general Navier-Stokes equations ($p^* = p$).

$$p^* = p(\rho, T) + \underbrace{\mu_0 \int_0^H \upsilon \left(\frac{\partial M}{\partial \upsilon} \right)_{H,T} dM}_{p_s} + \underbrace{\mu_0 \int_0^H M dH}_{p_m} \tag{G-2}$$

G-2   Ferrohydrodynamic Bernoulli equation

The ferrohydrodynamic Navier-Stokes equations can be simplified to the ferrohydrodynamic Bernoulli equation by assuming that the flow is irrotational and the gravitational force constant [36]. Additional assumptions are that the applied magnetic field and the magnetization inside the magnetic fluid are collinear [32] and the nonlinear magnetic material has no hysteresis [18]. Lastly, it is assumed that the magnetization is temperature independent. This results in the time dependent Bernoulli equation for magnetic fluids, Eq. (G-3) [33] [37]. The Bernoulli equation is a statement of energy conservation.

$$-\rho \frac{\partial \phi}{\partial t} + p^* + \frac{1}{2}\rho u^2 + \rho g h - \mu_0 \int_0^H M dH = f(t) \tag{G-3}$$

G-3   Ferrohydrodynamic boundary condition

In order to complete the description for a magnetic fluids a proper boundary condition is needed. The ferryhydrodynamic boundary condition is given by Rozensweig in Ferrohydro-dynamics [37], Figure G-1 and Eq. (G-4). Note that this boundary condition is only valid in the absence of viscous forces. In Eq. (G-4), p^* is the composite pressure (Eq. (G-2)), p_c the capillary pressure, p_n the magnetic normal traction and p_0 the ambient pressure, assumed to be $10^5 Pa$. It is reasonable to assume that the ferrofluid is complete saturated $\boldsymbol{M_n} \approx M_s$.
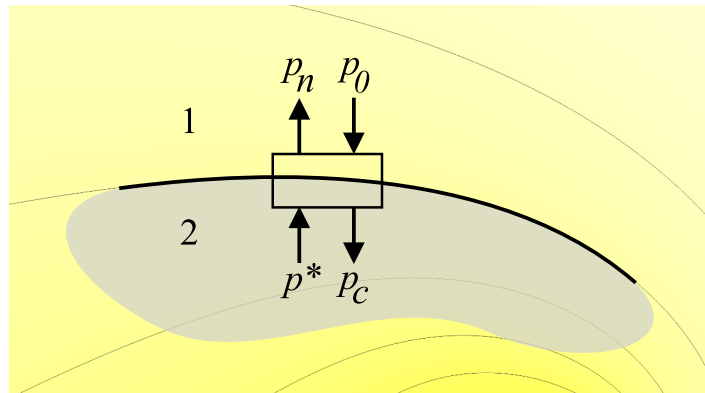

Figure G-1: The different forces acting at the interface between medium 1, non magnetizable, and interface 2, magnetizable.

$$p^* + \underbrace{\frac{\mu_o \boldsymbol{M_n}^2}{2}}_{p_n} = p_0 + \underbrace{\gamma \left(\frac{1}{R_1} + \frac{1}{R_2} \right)}_{p_c} \tag{G-4}$$

$$p^* + 2\pi \cdot 10^3 \sim 10^5 + 0.1 \left(\frac{1}{\overline{R}} \right) \tag{G-5}$$

The magnetic saturations of easily available ferrofluids range from $10kA/m$ until $100kA/m$. The surface tension between air and water is approximately $\gamma \sim 70mN/m$, so for ease of calculation, the surface tension is assumed to be $100mN/m$ (Eq. (G-5)) .

The pressure contribution of the magnetic surface traction for a ferrofluid with a magnetic saturation of $100kA/m$ is in the order of $\sim 5\%$ with respect to ambient pressure. The most common ferrofluids have a saturation of $\approx 30kA/m$. This results in a contribution of approximately 0.5%. The contribution due to surface tension remains below 10% if the radius of curvature $\overline{R}$ is $0.01mm$. Increasing the radius to $0.1mm$ reduces the pressure contribution to 1% with respect to p_0. Therefore, it can be concluded that in most cases, the pressure jump at the interface between ferrofluid and air can be neglected ($p^* \approx p_0$).

G-4   Ferrohydrodynamic instabilities

Two well known flow instabilities (in the absence of magnetic fluids and magnetic fields) are the Rayleigh–Taylor (Figure G-2) and Kelvin–Helmholtz (Figure G-3) instabilities [22]. Rosensweig modified these flow instabilities in Ferrohydrodynamics [37] such that they can be applied to magnetic fluids.

Figure G-2: This figure shows the Rayleigh–Taylor instability. *http://www.physicscentral.com/explore-/pictures/cup.cfm*

Figure G-3: This figure shows the Kelvin-Helmholtz instability in clouds. *http://earthsky.org/earth/kelvin-helmholzt-clouds*

The Kelvin–Helmholtz instability is an inertial instability at the interface between two horizontal and parallel velocity streams with different densities (Figure G-4). The result of the derivation is the stability criterion for the Kelvin-Helmholtz problem, Eq. (G-6). σ denotes the surface tension and H_y the applied magnetic field. Increasing the speed difference between the two streams facilitates the instability, while increasing the applied magnetic field accommodates stability. However, this depends on the direction of the applied magnetic field. A

magnetic field acting normal to the wave (uncoupled) does not stabilize the flow. A collinear applied magnetic field with respect to the wave direction (coupled) does stabilize the flow (Figure G-5) [37].
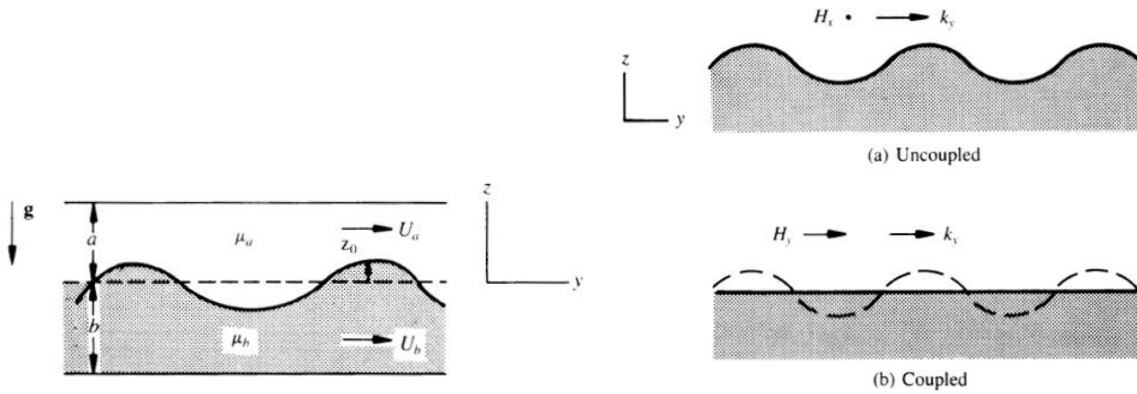

Figure G-4: This figure shows the different parameters used in the derivation of the instability criteria [37].

Figure G-5: This figure presents the surface deflection for two different applied magnetic fields. The top figure shows a tangential magnetic field acting perpendicular to the direction of wave propagation. The bottom figure shows a magnetic field collinear with the direction of the wave propagation [37].

$$(U_b - U_a)^2 > \frac{\rho_b + \rho_a}{\rho_b \rho_a} \left(2 \left(g(\rho_b - \rho_a)\sigma \right)^{1/2} + \frac{(\mu_a - \mu_b)^2 H_y^2}{\mu_a + \mu_b} \right) \tag{G-6}$$

Rosensweig [37] gives the dispersion relationship for the magnetic Rayleigh-Taylor problem as Eq. (G-7) for a tangential applied magnetic field. The stability for the Rayleigh-Taylor problem is given in Figure G-6 for magnetic and non-magnetic fluids. Increasing the magnetization of the ferrofluid increases the stability.

$$\omega^2 (\rho_a + \rho_b) = gk(\rho_b - \rho_a) + \sigma k^3 + k_y^2 \frac{\mu_0 M_0^2}{\chi + 2} \tag{G-7}$$
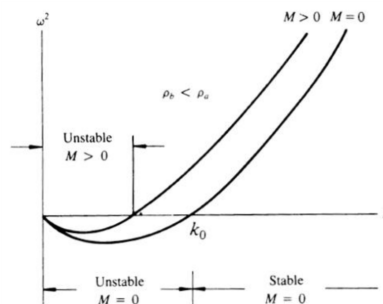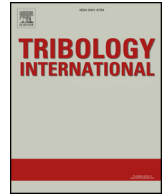

Figure G-6: This figure shows the Rayleigh–Taylor instability for magnetic fluids in the $\omega - k$ plane. Increasing the magnetization increases the stability [37].

Increasing the load capacity of planar ferrofluid bearings by the addition of ferromagnetic material

A.S.T. Boots, L.E. Krijgsman, B.J.M. de Ruiter, S.G.E. Lampaert[*], J.W. Spronck

Department of Precision and Microsystems Engineering, Delft University of Technology, Mekelweg 2, 2628CD, Delft, the Netherlands

ABSTRACT

Ferrofluid pocket bearings are a type of bearing that are able to carry a load using an air pocket encapsulated by a ferrofluid seal. Previously designed ferrofluid bearings show the great potential of the stick-slip-free and low viscous friction bearings, however until now the load capacity is limited. In this article a method is presented to increase the load capacity in a simple and cost effective way by the addition of ferromagnetic material around the magnet. First, a mathematical model of the bearing is presented and is validated by experiments using an axially magnetized ring magnet surrounded by two steel rings. The model is used to optimize the dimensions of the added ferromagnetic material for maximum load capacity. Depending on the fly height, the load capacity has been increased by a factor three to four by the addition of steel rings to the ferrofluid pocket bearing configuration.

1. Introduction

The kerosene based magnetic fluid or so called ferrofluid that NASA developed in the 1960s appeared to be interesting to apply in seals and bearings as shown by Rosensweig et al. in the 1970s [1–4]. A ferrofluid can be defined as a fluid with paramagnetic properties that are generated by being a colloidal suspension of small magnetic nanoparticles (10 nm) [5,6]. The application of an external magnetic field increases the pressure inside the fluid after which the fluid is capable of carrying loads [7–9], thus can act as an actuator [10–16] or seal [17–21]. Ferrofluid can be used to yield mechanisms that have complete absence of both stick slip and mechanical contact resulting respectively a potential high precision and high lifetime [7,8,22,23].

Because the fluid in ferrofluid bearings is contained by the presence of a magnetic field that is generated by for example a permanent magnet, no seals or active components are required. Therefore, a ferrofluid bearing is a passive, simple, and cost effective alternative to traditional bearings. Examples of these ferrofluid bearings can be found in literature, but despite the great potential, application is still very limited [7–9,24–29]. One reason for this is that the load capacity and stiffness is relatively limited. Lampaert et al. recently developed a mathematical model to describe the load and stiffness characteristics of ferrofluid bearings, which makes it now possible to design for maximum load capacity [7,8,22,23,26,30–33].

The load capacity of a ferrofluid bearing is created by the pressurized air pocket(s) encapsulated by the ferrofluid seals. The shape of the magnetic field and the number of air pockets between non-connected seals seem to be of great importance to the load capacity. The goal of this article is to increase the load capacity of ferrofluid bearings by the addition of ferromagnetic material.

The addition of ferromagnetic material, in this case steel, has the ability to concentrate the magnetic field generated by the permanent magnet and could therefore increase the load capacity [34,35]. Furthermore, steel could alter the shape of the magnetic field such that multiple air pockets can be created. Steel has a high magnetic saturation and a high relative permeability which makes this material suited for improving the load capacity.

First, a model is presented to calculate the load capacity of a ferrofluid double pocket bearing. This model is validated by experiments and will then be used to optimize the geometries of the steel rings. The acquired knowledge can be used as design rules for increasing the load capacity of planar ferrofluid bearings by the addition of ferromagnetic material.

2. Methods

First, an analytical model for the load capacity of a ferrofluid double pocket bearing is presented based on the available literature. Second, the four different bearing models, model A through D, are presented after which the FEM analysis, using COMSOL Multiphysics, is
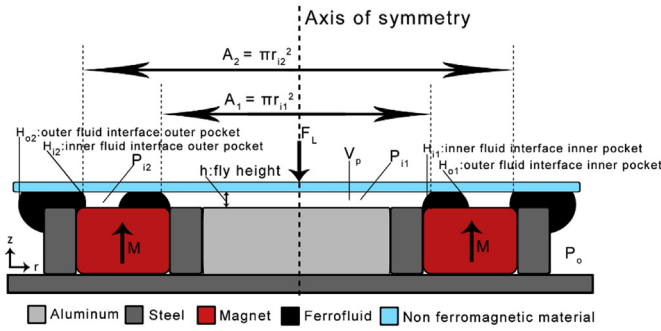

Fig. 1. This figure presents the cross section of the ferrofluid bearing with the defined parameters. The ring magnet is surrounded by two ferromagnetic rings, in this case steel, with an aluminum disk placed inside. The entire setup is mounted on a steel baseplate. Important parameters are the pressures and areas of the air pockets and the magnetic field intensities at the different fluid interfaces.

introduced to calculate the magnetic field intensities. These magnetic field intensities in combination with the analytical model are used to calculate the load capacity. Next, the experimental setup used for the validation of the described model is presented after which the optimizations of models A-D are described.

2.1. Analytical model

The analytical model for a ferrofluid single pocket bearing [8,9,24] is extended to a model predicting the load capacity of a ferrofluid double pocket bearing, schematically represented in Fig. 1. The Navier-Stokes equations for incompressible magnetic Newtonian fluids can be simplified to equation (1) assuming a stationary, low Reynolds number incompressible flow with a Newtonian fluid model. The relation presents the pressure gradient ∇p as the product of the magnetic permeability of vacuum μ_0, the magnetization strength of the fluid M_s and the magnetic field gradient ∇H.

$$\nabla p = \mu_0 M_s \nabla H \qquad 1$$

Application of the Fundamental theorem of calculus gives the relationship used for calculating the load capacity of the air pockets, equation (2).

$$F_{pocket} = \int_A (p_i - p_o)dA_{pocket} = \mu_0 M_S \, \Delta H \, A_{pocket} \qquad 2$$

Both the pressure inside the air pocket and the pressure inside the ferrofluid ring contribute to the total load capacity of the bearing. Although the load carrying contribution of the seal is relatively small in comparison to that off the pocket, it will be included in the calculation to get the most accurate prediction of the total load capacity. Equation (3) shows the approximation of the load capacity of the seal as described by Lampaert et al. [7].

$$F_{seal} = \int_A (p_s - p_0)dA_{seal} \approx \mu_0 M_S \, \Delta H \, \frac{A_{seal}}{3} \qquad 3$$

For a bearing configuration with two seals and two pockets the total load capacity is simply obtained by adding the load capacities of both pockets and both seals. Each contribution to the total load capacity is calculated by integrating the pressure difference over the area, as can be seen in equation (4). This is visually shown in Fig. 5, where the load capacities of the ferrofluid bearing for the magnet only and for the magnet with steel rings correspond to the orange and red surface respectively. The pressure distribution is a result of the magnetic field intensities of the fluid-air interfaces (H_{i1} H_{i2} H_{01} H_{02}), see Fig. 1. By integrating this pressure distribution, the total load capacity is calculated.

Implementation of a second ferrofluid seal has the advantage that the pressure can be increased twice, one time over each ferrofluid seal. It is important to note that the pressure contribution of the doughnut shaped second pocket, A_{p2}, as given in equation (4) can be rewritten to equation (5), in which the pressure contributions of both pockets act on a circular surface as defined in Fig. 1. To illustrate this, the pressure distribution which is given in Fig. 5 corresponds to the magnetic field intensities at the interfaces between ferrofluid and air, given in Fig. 4.

$$F_{load} = \int (p_{i1} - p_0)dA_{p1} + \int (p_{s1} - p_0)dA_{s1} + \int (p_{i2} - p_0)dA_{p2}$$
$$+ \int (p_{s2} - p_0)dA_{s2} \qquad 4$$

$$F_{load} \approx \mu_0 M_S \left((H_{i1} - H_{o1})\left(A_1 + \frac{A_{S1}}{3}\right) + (H_{i2} - H_{o2})\left(A_2 + \frac{A_{S2}}{3}\right) \right) \qquad 5$$
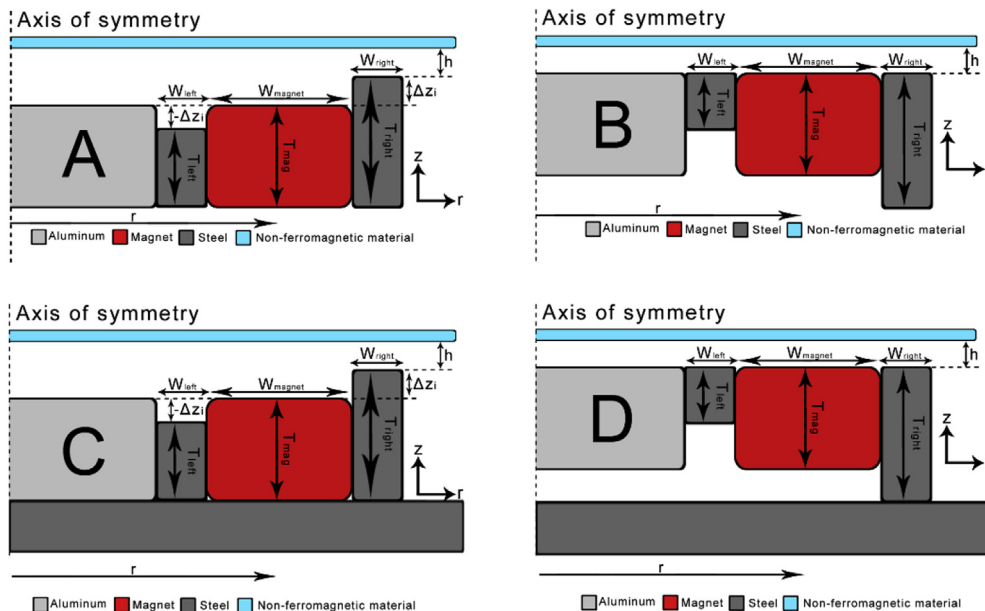

Fig. 2. This figure presents the four different bearing models and their design variables. In contrast to Model C and D, model A and B have no ferromagnetic baseplate. Model A and C are defined from bottom up and model B and D are defined from top down.

Table 1

This table presents a list of variables which are considered to be constant for the different bearing models A-D.

Optimization constants Optimization: Constants	
M_s	$= 35\,kA/m$
μ_0	$= 4\pi*10^{-7}N/A^2$
W_{mag}	$= 8.5mm$
T_{mag}	$= 6mm$
T_{base}	$= 3mm$
h_{fly}	$= 0.2mm$
$B_{saturation,steel}$	$= 2.4T$
M_{magnet}	$= 1.25T$
p_0	$= 10^5Pa$

2.2. Bearing models

There are four distinct bearing models presented in this section, which will be referred to as model A, model B, model C and model D (Fig. 2). In all the models the ring magnet is sandwiched between two steel rings with varying widths and thicknesses. Both steel rings are attached to the magnet such that no volume exists between the steel rings and magnet.

The variables which are considered to be constant during the optimization of the bearing models A-D can be found in Table 1.

In model A the rings are fixed with respect to the bottom surface of the magnet. The thickness of the steel rings is defined with T_{left} and T_{right} and the width of the steel rings is defined with W_{left} and W_{right}. An additional parameter Δz_i is defined in equation (6), in which T_i indicates the thickness of the steel rings for either the left or right side.

$$\Delta z_i = T_i - T_{mag} \qquad 6$$

It can be concluded from the results of the model presented in section 3.2 that the top surface of the steel rings has to be at equal height as the surface of the magnet such that no steel protrudes beyond the thickness of the magnet. Therefore, model B is introduced. The steel rings are now fixed with respect to the top surface of the magnet and extended downwards.

To investigate the influence of a ferromagnetic baseplate on the load capacity, model C and D are introduced. Model C and D correspond to model A and B respectively, however with a 3 mm steel plate added. The baseplate is directly attached underneath the lowest part of the ferrofluid bearing (Fig. 2).

2.3. FEM analysis and load calculation

The magnetic fields generated by the different bearing configurations are calculated using the numerical analyses package COMSOL 5.3. The magnetic field intensity at the different fluid-air interfaces (H_{i1} H_{i2} H_{01} H_{02}) have to be evaluated in order to calculate the total load capacity according to equation (5).

The low grade steel of the rings surrounding the magnet is modelled by using the BH curve from the soft iron (with losses) material in the COMSOL library. Fillets are constructed at all the corners to prevent singularities in the calculations [36]. The model and the result of a single simulation example can be seen in Fig. 3 and Fig. 4. This example corresponds to model C as defined in Fig. 2. The bearing models are parameterized and controlled by Matlab (2017b) using the Livelink toolbox to find an optimal geometry.

The distribution of the magnetic field given in Fig. 3 is evaluated along a horizontal line at a specified height above the highest surface of the bearing, the so called fly height as defined in Fig. 1. An example of this line evalutation is given in Fig. 4 and is used to extract the magnetic strengths of the different interfaces. The ferrofluid will position itself at maximum load such that the inner fluid interfaces H_{i1} and H_{i2} are located at the maximum field intensities thus the peak values of Fig. 4.
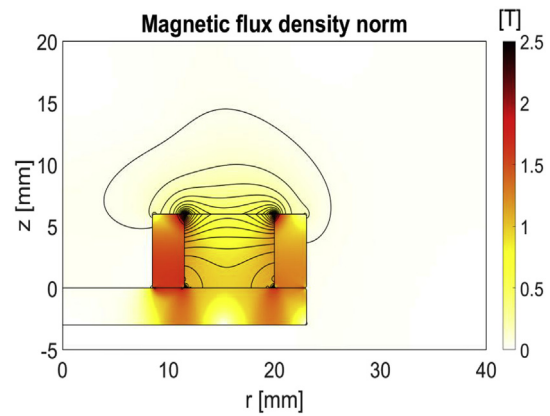

Fig. 3. This figure presents the distribution of the magnetic field expressed in Tesla for the bearing testing setup of model C consisting of the ring magnet, steel rings and baseplate. The magnet is modelled after HKCM 9963–58947 with an axial magnetization strength of 1.25 T. The magnetic behaviour of the steel rings and baseplate is modelled in COMSOL using the built-in BH-curve of soft iron.
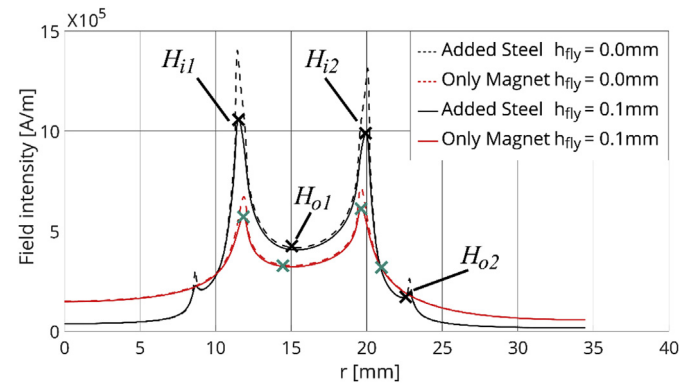

Fig. 4. This figure presents the results of the FEM analysis for the magnetic field intensities, at 2 different fly heights, for the ring magnet (40 mm × 23 mm X 6 mm) with and without the addition of 3 mm × 6 mm steel rings. The magnetic flux density of the magnet is 1.25 T.

H_{01} is evaluated at the valley between the peaks in the middle of the magnet at a fly height of zero. When the value of H_{01} is bigger than either H_{i1} or H_{i2}, one seal and one air pocket is created. This comes from the fact that the fluid flows to the outer interface when the peak at a certain fly height is lower than the lowest value of the field intensity at the magnet (h= 0). The load capacity is then calculated with only the first part of equation (5). When both peaks are higher than the lowest field intensity at the magnet, two seals are created and both terms in equation (5) are taken into account. H_{o2} is evaluated at the fluid interface of the outer seal for a certain fly height. When the flyheight decreases, the ferrofluid seal is pushed outwards. For the magnet only, the outer interface of the ferrofluid seal increases from a radial distance of 21 mm–21.2 mm for fly heights of 1 mm–0 mm respectively. When steel rings are added, the radial distance of the outer interface remains 21.5 mm for a fly height of 1 mm, but increases to the radial distance of the outer steel ring at a fly height of 0 mm due to the steel rings. These values are observed experimentally and are interpolated linearly.

The radial position of the different field intensities are used to calculate the areas of the seals and the pockets. Finally, the load capacity of the bearing is calculated by combining the different field intensities with the corresponding areas and substituting this in equation (5).

To summarize, the FEM model (Fig. 3) is used to calculate the magnetic field produced by the magnet. This field is then evaluated to obtain the field intensities (Fig. 4), which can be used to calculate the
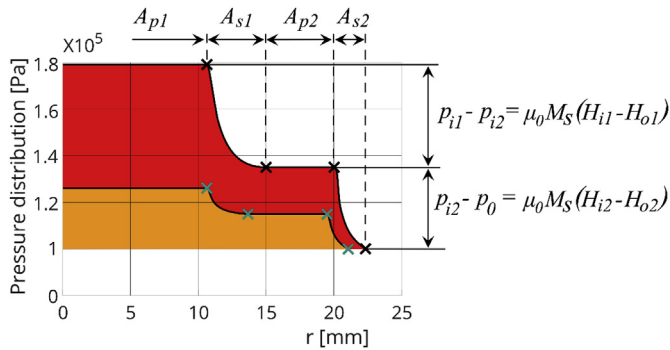
Fig. 5. This figure presents the pressure increase over the ferrofluid seals for both the magnet and the magnet with steel rings. The total load capacities for the magnet only and for the magnet with steel rings are indicated as the red and orange area resp. (For interpretation of the references to colour in this figure legend, the reader is referred to the Web version of this article.)

corresponding pressure distribution (Fig. 5) using the presented analytical model. Finally, the load capacity is obtained by integrating the pressure distribution of the area, indicated by the red area in the figure. Note that in Fig. 5 the pressure distribution and load capacity for the magnet only and for the magnet with steel rings are presented.

2.4. Experimental setup

The analytical model presented in section 2.1 is validated by comparing the predicted load capacity of the bearing with and without steel rings to the results of the measurements. Measurements are done to investigate the maximum load capacity of the bearing and validate the analytical model.

2.4.1. Load capacity

The maximum load capacity of the bearing with and without steel is measured using a tensile testing machine (Zwick/Roell Z005) capable of measuring the force over displacement. To prevent systematic errors, the machine is calibrated before measuring the load capacity. Each measurement is done three times to detect possible random errors. The velocity of the head of the testing machine is set to be 1 mm/min.

The bearing is mounted on top of a steel base plate, which corresponds to bearing model C (Fig. 2), and clamped on the table below the machine, see Fig. 6. Both the rings and the baseplate are made of low grade steel in the test setup, since the material is relatively cheap and has desirable ferromagnetic properties, which approximates the material used in the analytical model. There is assumed that the stiffness of the table is infinite with respect to that of the bearing. Moreover, the mounting is assumed to be rigid. Note that the volume inside the
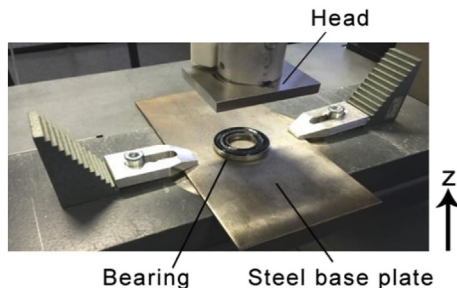

Fig. 6. This figure presents the bearing consisting of a ring magnet, two steel rings and ferrofluid. The ring magnet, HKCM 9963–58947 with dimensions 40 mm × 23 mm x6mm and a flux density of Bz = 1.25 T, is placed on a steel baseplate. This plate is clamped on the table and placed below the testing machine. 1 mL of ferrofluid is added to the bearing. The velocity of the head of the testing machine is set to be 1 mm/min.

magnet (and steel) in Fig. 6 is reduced by placing an aluminium cylinder inside. This is done in order to minimize the compressibility effect of air by reducing the volume of the inner air pocket [7]. Aluminium is chosen for its non-ferromagnetic properties, high stiffness and availability.

All the components are sealed and mounted with glue to prevent air leakage out of the two pockets. Then, 1 mL of FerroTec EFH1 is added. This amount of ferrofluid is redundant and can therefore create one or multiple air pockets and has a load carrying capacity up to fly heights of 1 mm.

The measurement of the load capacity starts just before the head of the testing machine touches the ferrofluid. No pressure can be build up across the seals at this point yet, because there are no separate air pockets and therefore no difference in magnetic field intensity across the ferrofluid seal ($\Delta H = 0$). The fly height is then decreased until the head of the testing machine starts pushing on the magnet itself. This indicates the end of the measurement of the load capacity.

2.5. Optimization

In this section the validated model, see results in section 3.1, will be used to optimize the geometry of the bearing models given in Fig. 2 for maximum load capacity. For the optimization, the fly height h is set to be 0.2 mm. The optimization of model A shows that the thickness of the steel rings should be equal to the thickness of the magnet, see results in section 3.2. Therefore, bearing model B is introduced. The configuration given in Fig. 2 of model B is optimized in a symmetric and asymmetric way. To investigate the influence of a ferromagnetic baseplate model C and D are introduced, as presented in section 2.2.

2.5.1. Optimization model A and C

The bearing models A and C presented in Fig. 2 will be optimized in both a symmetric and asymmetric configuration. The symmetric optimization is done in order to see the effect of the different variables on the load capacity of the bearing. Symmetric means in this case that the cross section of both steel rings have the same dimensions, thus $W_{left} = W_{right}$, $T_{left} = T_{right}$ and therefore $\Delta z_{left} = \Delta z_{right}$, as can be seen in Fig. 7. The design variables are normalized with respect to the dimensions of the magnet such that the results are easier to interpret. The normalizations are given in equations (7)–(9).

$$T_{ratio} = \frac{T_{steel}}{T_{mag}} \qquad\qquad 7$$

$$W_{ratio} = \frac{W_{steel}}{W_{mag}} \qquad\qquad 8$$

$$\Delta z_{ratio} = \frac{\Delta z}{T_{mag}} \qquad\qquad 9$$

This results in two design variables for the symmetric optimizations, namely: T_{ratio} and W_{ratio}. The design variables for the asymmetric
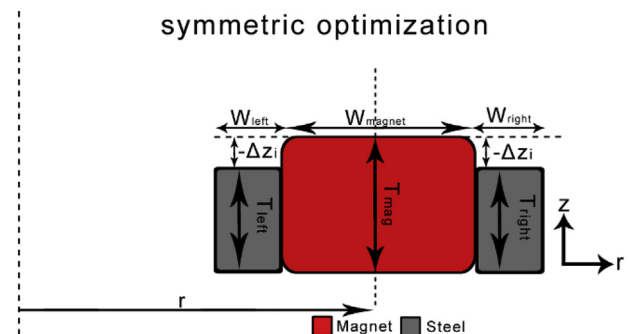

Fig. 7. This figure shows the variables for symmetric optimization and the cross sections of the steel rings.

optimizations for both models are: $T_{ratio-left}$, $W_{ratio-left}$, $T_{ratio-right}$, $W_{ratio-right}$. The Δz_{ratio} is introduced to investigate the height of the steel relative to the height of the magnet.

2.5.2. Optimization model B and D

The bearing models B and D, presented in Fig. 2, will be optimized in a symmetric and asymmetric way. The symmetric optimization is done in order to see the effect of the different variables on the load capacity of the bearing. Due to symmetry, $W_{left} = W_{right}$ and $T_{left} = T_{right}$. The design variables for the symmetric optimization of models B and D are reduced to: T_{ratio} and W_{ratio} and are defined in Fig. 7.

Finally, the asymmetric optimization is performed to see if introducing asymmetry in the system can further improve the load capacity. Note that all the different parameters are again normalized with respect to the magnet in the results. The design variables for the asymmetric optimization of models B and D are: $T_{ratio-left}$, $W_{ratio-left}$, $T_{ratio-right}$, $W_{ratio-right}$, as defined in Fig. 2.

2.5.3. Optimization algorithm

To find an optimum for the configurations described above, an algorithm is designed. The algorithm can be seen as a multi-point approximation method. It evaluates a certain preset subdomain of the design space. The optimal point of the subdomain is considered to be the midpoint of the next subdomain in the next cycle. The process can be seen in Fig. 8. In the asymmetric optimization of the steel rings, this results in a 4D subdomain, consisting of all the design variables. This algorithm solves the optimization problem and is convenient since the function evaluations ask a lot of computational effort.

A subdomain is built using its midpoint, the length of the subdomain and the number of samples. The side length of the subdomain is chosen such that the dimensions of steel increase from no steel rings up to the inner side of the magnet completely filled with steel. Then the subdomain is evaluated and the minimum value is determined. To achieve convergence, the size of the new subdomain must be smaller than that of the previous one. Therefore, the length of each side of the new trust region is scaled. Scaling (< 1) of the subdomain makes the algorithm converge to a certain optimum. The scaling number is determined iteratively by varying this number. A small scaling number makes the subdomain converge too fast and the optimal value is not found ($S < 0.4$). A larger scaling number result in more iterations, but the optimum is found ($0.4 < S < 0.1$).

3. Results

3.1. Load capacity

The load capacity has been analytically calculated and
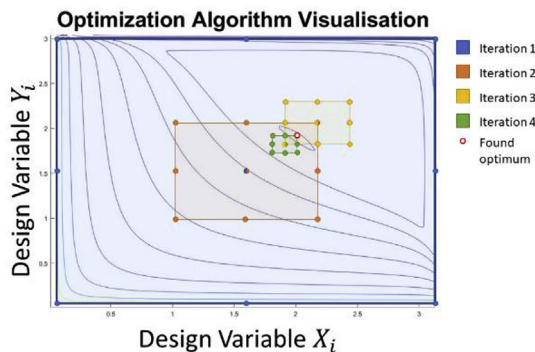

Fig. 8. This figure presents the way the optimization algorithm works. In the first step the entire domain is considered in which 9 points are evaluated. The best point will be the centre of the next iteration step in which the domain will be smaller. These steps will be repeated until an optimum is found.
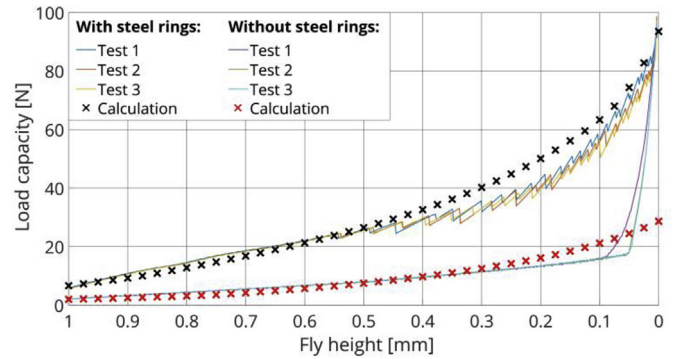

Fig. 9. This figure presents the load capacity predicted by the analytical model and measured by the testing machine versus different fly heights for the magnet only and the magnet with 3 mm wide inner and outer steel rings that have the same z-position as the magnet.

experimentally measured for both the single magnet and the magnet with steel rings for several fly heights. These results can be seen in Fig. 9. The results of the different experiments are indicated with continuous lines while the calculations are indicated with crosses.

Notable is that adding a 3 mm wide inner and outer ring of steel improves the load capacity of the bearing at fly height 0.2 mm with approximately a factor 4. For higher fly heights this factor ranges approximately from 3 to 4. This is a significant improvement compared to the ferrofluid pocket bearing without the steel rings. Also note the zigzag pattern in the measurements for the improved bearing at lower fly heights.

The overall behaviour of the load capacity of the improved bearing is predicted well by the calculations and both the model and measurements are in good accordance with each other.

3.2. Optimization

The results of the optimization of model A are given in Fig. 10. From this plot it can be concluded that the load capacity is the highest for $\Delta z = 0mm$ for all the different normalized widths of the steel rings. Note that the load capacity significantly decreases if Δz_{ratio} deviates from zero.

The results of the symmetric optimization of model B are given in Fig. 11, Figs. 12 and 13. Fig. 11 shows the load capacity for the two design variables in a single surface plot. Figs. 12 and 13 show side views or cut troughs of the surface plot in Fig. 11.

Fig. 13 shows that the T_{ratio} needs to be approximately 1.2 or higher. The load capacity decreases significantly when the T_{ratio} decreases. In combination with Fig. 13 this leads to the conclusion that for a
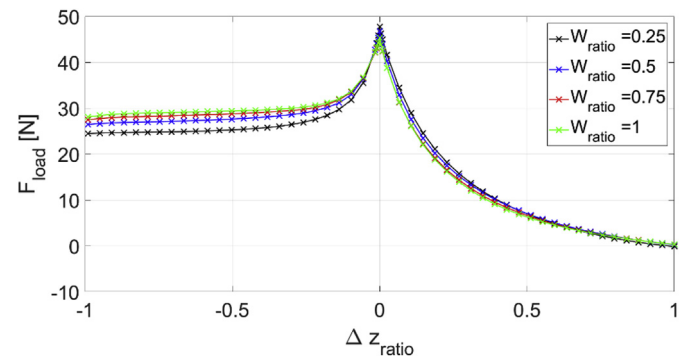

Fig. 10. This figure presents the load capacity of the ferrofluid bearing with additional steel rings for varying thicknesses and widths of the rings. These dimensions are normalized with respect to the thickness and width of the magnet.
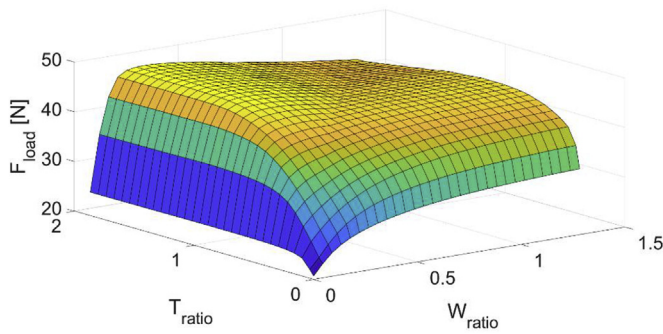
Fig. 11. This figure presents a surface plot of the load capacity of model B with varying dimension parameters H_{ratio} and W_{ratio}.
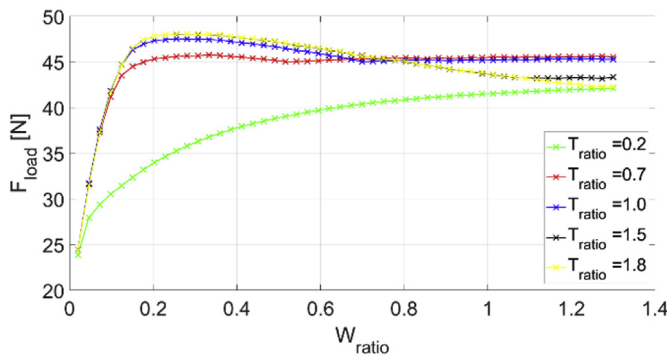

Fig. 12. This figure presents the load capacity of model B versus W_{ratio} for different H_{ratio}.
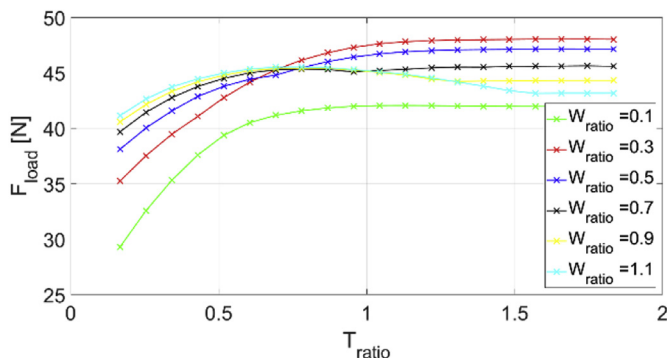

Fig. 13. This figure presents the load capacity of model B versus H_{ratio} for different W_{ratio}.

symmetric configuration of steel rings without baseplate the maximum load capacity of approximately 48N is achieved for $T_{ratio} \approx 1.8$ and $W_{ratio} \approx 0.26$.

The results of the symmetric and asymmetric optimization of model A, B, C and D are given in Table 2. It can be concluded that the addition of the ferromagnetic baseplate changes the optimal geometry of the added ferromagnetic rings as can be seen in Figure 14. Furthermore, when the baseplate is added, an additional 3 N ($\approx$ 6%) increase in load capacity can be obtained.

A visual representation of the optimized bearing configurations for the bearing models is given in Figure 14. The dimensions of the steel rings and the load capacities can be found in Table 2.

4. Discussion

4.1. Analytical model and measurements

Overall, the measurements show that the load capacity of the ferrofluid double pocket bearing is increased 3 to 4 times depending on the fly height by the addition of steel rings around the ring magnet. Addition of these ferromagnetic rings increases the difference in magnetic field intensities over the ferrofluid seal. This increase has the advantage that capillary effects can be overcome such that two air pockets are created. Both the increase in difference in field intensities and the addition of the second seal contribute to the total load capacity, leading to an increase of a factor 4.

The measured load capacity of the bearing with and the bearing without steel rings correspond well to the calculated load capacity. However, the calculations do slightly differ from the actual measurements for both models. From the results it can be seen that at lower fly heights the load capacity for both models is overestimated. This overestimation is probably due to the fact that capillary effects are not taken into account in the mathematical model. Moreover, these capillary effects increase when the fly height decreases.

Also for a magnet with steel rings, the load capacity is overestimated. It seems that the capillary effects are overcome and two seals are formed. However, for low fly heights, the ferrofluid is pushed outwards too far due to the steel rings and do not participate in the load capacity anymore. Therefore, the volume of effective ferrofluid decreases during the measurements, leading to an overestimation of the load capacity. When the amount of effective ferrofluid is overestimated, the realistic value of the H_{o1} is not the lowest value for the field intensity at the magnet and is therefore not located at the valley. The outer interface of the ferrofluid will be located at a higher field intensity, leading to a lower load capacity.

On top of that, the steel rings are modelled in COMSOL as soft iron. In reality, there will be a difference in material properties between the steel rings and the material used in the model. The overall behaviour/shape of the predicted load capacity of the bearing with steel does correspond well to the measurements, and therefore the model can be seen as valid and is used for optimization. It is likely that finding a better BH curve will reduce the overestimation of the load capacity. Another possible error in the FEM model is the applied radius of the fillets, which might also differ from the actual fillets of the steel rings and magnet used in the experimental setup. Note that in general the FEM model starts to become unreliable when the fly height is approaching zero. This is due to effects in the FEM analysis near boundaries and corners of the magnet.

When the fly height is decreased in the measurements, the assumed incompressible ferrofluid is pushed outwards. The fluid-air interfaces get displaced outwards, this increases the areas of the seals and changes the magnetic field intensities at the different interfaces. These effects are included in the analytical and numerical model. In the model, the most outer interface is assumed to linearly increasing from a radial distance of 21 mm–21.2 mm and 21 mm to the radial distance of the edge of the outer steel ring for the magnet only and the magnet with steel rings respectively. Implementation of a more realistic gradient in this outer interface will probably yield better results.

When the fly height is decreased the air pressure inside the pockets increases until the point that the seals cannot withstand the pressure anymore. Air escapes out of the pocket and causes the ripples or zig-zag pattern in the measurements in Fig. 9.

4.2. Optimization model A and C

When the W_{ratio} is (very) small there is simply very little steel added to the bearing resulting in that the influence of the steel on the magnetic field is almost negligible. To prevent instant saturation, the W_{ratio} has to be higher than a certain value. Approximately a W_{ratio} of 0.3

Table 2

This table presents the overview of the optimization of the load capacities for the different bearing models discussed in this article **without and with** baseplate.

Model		Design variables				Field intensities				Result
		$T_{ratio-left}$	$W_{ratio-left}$	$T_{ratio-right}$	$W_{ratio-right}$	$H_{i1}\left[\dfrac{\times 10^5}{A/m}\right]$	$H_{o1}\left[\dfrac{\times 10^5}{A/m}\right]$	$H_{i2}\left[\dfrac{\times 10^5}{A/m}\right]$	$H_{o2}\left[\dfrac{\times 10^5}{A/m}\right]$	**LOAD CAPACITY** [N]
A	Symmetric	1	0.27	1	0.27	8.268	3.652	7.581	1.486	47.29
	Asymmetric	1	0.24	1	0.29	8.238	3.648	7.585	1.417	47.65
B	Symmetric	1.8	0.26	1.8	0.26	8.53	3.708	7.692	1.547	48.06
	Asymmetric	1.71	0.27	1.71	0.31	8.500	3.702	7.700	1.5	48.31
C	Symmetric	1	0.37	1	0.37	8.835	4.225	8.198	1.420	51.19
	Asymmetric	1	0.35	1	0.37	8.822	4.224	8.203	1.420	51.20
D	Symmetric	1	0.37	1	0.37	8.835	4.225	8.198	1.420	51.19
	Asymmetric	1	0.35	1	0.37	8.822	4.224	8.203	1.420	51.20

balances complete magnetic saturation and diffusion of the magnetic field into the steel when the width of the steel rings becomes to large.

Regardless of the width of the steel rings, the thickness of the steel rings has to be equal to the thickness of the magnet to obtain the maximum load capacity (section 3.2). When the thickness of the steel rings is less than that of the magnet, the magnetic field is less concentrated at a fly height just above the magnet because the field lines have to travel a greater distance through the air to close the magnetic circuit using the steel. Also due to the low relative permeability of air, the magnetic field lines diffuse into the air, which lowers the load capacity. On the other hand, when the thicknesses of the ferromagnetic rings are higher than the magnet, the fly height is defined as the distance between the non-ferromagnetic plate and the top of the steel rings instead of the magnet (Fig. 2). The magnetic field will in this case be concentrated within the volume above the magnet and between the steel rings surrounding the magnet while the load capacity is determined by the fly height above the steel rings where the magnetic field is much weaker. Therefore, taking the thickness of the steel rings smaller than that of the magnet is less detrimental to the total load capacity of the ferrofluid bearings than taking the thickness too big.

Besides that, steel rings with the same thickness as the magnet have the advantage that the flat top prevents the ferrofluid from dripping down. In this way, the ferrofluid can be used in an optimal way since the ferrofluid seal is able to span a greater horizontal length which increases the load capacity since the difference in magnetic field increases between both interfaces ($\Delta H = H_i - H_0$).

4.3. Optimization model B and D: symmetric

When the T_{ratio} is (very) small there is simply very little steel added to the bearing resulting in that the influence of the steel on the magnetic field is almost negligible, see Fig. 12. The magnetic field has to travel through the air instead of the added steel. Therefore, increasing the thickness of the steel rings increases the load capacity significantly until a T_{ratio} of 1.2 is reached for the bearing without baseplate (model B). For a T_{ratio} of 1, the thickness of the steel rings and the magnet are equal. In this case, the magnetic field leaves the steel and has to make a 180° turn through the air to close the magnetic circuit. Steel rings which are slightly thicker than the magnet reduce this turn to 90°. Therefore a T_{ratio} of at least 1.2 results in the highest load capacity. Further increasing the thickness of the steel beyond a ratio of 1.2 has no influence on the load capacity since the magnetic field does not protrude into the added steel since this would increase the path by the magnetic field lines to close the magnetic circuit. When a baseplate is added below the bearing the thickness of the steel rings has to be equal to the thickness of the magnet.

This can be explained by looking at the magnetic properties of the added material. Once the width of the rings is too small, magnetic saturation of the rings occurs which can be seen in Fig. 12. After the ferromagnetic material is saturated, the magnetic field is not influenced by the material anymore. Therefore, the magnetic saturation of the ferromagnetic material limits the load capacity. Increasing the width increases the load capacity. However, when the width of the rings is too large, the field lines are not concentrated at the edges of the magnet where the ferrofluid will be placed, but distributed into the steel rings,
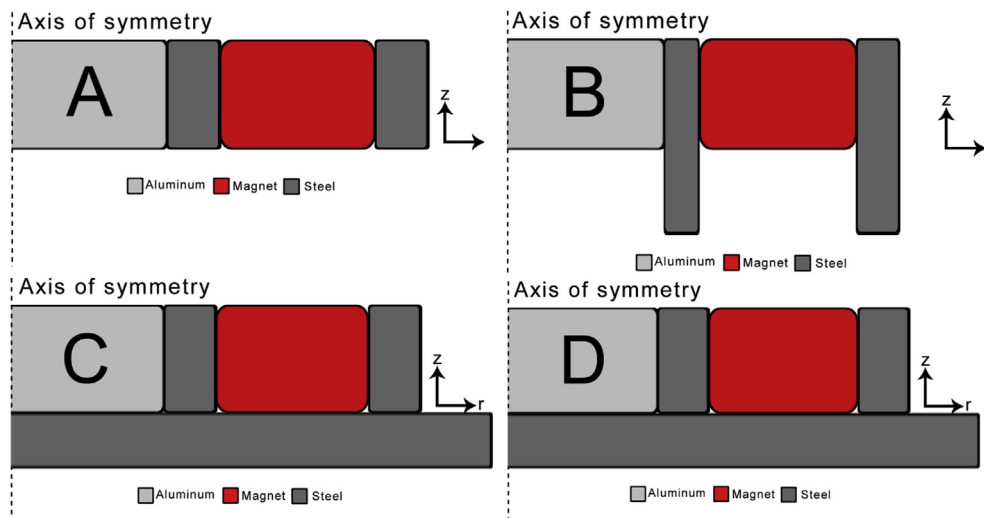

Fig. 14. This figure presents the optimal bearing configurations to achieve maximum load capacity for the ring magnet sandwiched between steel rings without being placed on top of a baseplate (model A and B) and placed on top of a baseplate (model C and D).

which decreases the load capacity. When the width of the rings is increased even further, the dispersion does not increase and therefore the load capacity remains constant which explain the behaviour in Fig. 12 for increasing widths of the steel rings.

Therefore, it can be concluded that the steel needs to have a certain minimum width to prevent magnetic saturation. The optimal width of the rings for the symmetric model B is $W_{ratio} = 0.26$ which balances the magnetic saturation and dispersion of the magnetic field. When a baseplate is added (Model D) the rings need to be a little bit wider (Table 2), namely $W_{ratio} \approx 0.37$. Note that when the inner ring is increased such that the magnet is completely filled with steel, the magnetic field is short circuited and the load capacity decreases.

4.4. Optimization model B and D: asymmetric

The optimal thickness of the rings in the asymmetric optimization of model B happens to be symmetric, namely $T_{ratio} = 1.71$ for the bearing without baseplate, see Table 2. The thickness of the rings exceeds the thickness of the magnet such that it is easier for the magnetic field to close the magnetic circuit. Only a turn of 90° is required for the magnetic field when it leaves the steel ring instead of a full 180° turn. When an additional ferromagnetic baseplate is added the optimal thickness of the rings is equal to the thickness of the magnet which is quite convenient when mounting the bearing. This way the entire magnet is surrounded by steel except for the top surface where the ferrofluid is placed. Besides that the addition of the baseplate changes the optimal thickness significantly such that the bearing can be mounted much more easily, the load capacity is increased by approximately $3N$ ($\approx 6\%$) therefore it is recommended to choose the thickness of the rings equal to the thickness of the magnet and to mount the bearing on a ferromagnetic baseplate.

The optimal width for the steel rings also depends on the presence of a baseplate. As earlier mentioned, a certain minimum value for the width is required to prevent magnetic saturation. If the width is too large the concentration of the magnetic field is decreased which decreases the load capacity but this effect is not as detrimental as the magnetic saturation of the steel. When a baseplate is present, the optimal widths of the steel rings is slightly bigger with respect to a bearing without baseplate, namely $W_{ratio} \approx 0.27$ (model A) & $W_{ratio} \approx 0.26$ (model B) versus $W_{ratio} \approx 0.37$ (model C) & $W_{ratio} \approx 0.37$ (model D) respectively. Introducing asymmetry into the system only increases the load capacity marginally (0.1%) and one can therefore argue whether it is worth the trouble to implement this in practice.

The load capacity can even be increased further if the strength of the magnet and the magnetic saturation of the ferromagnetic material are increased. A larger magnet (a larger T_{mag} or W_{mag}) has a bigger volume and therefore higher magnetic field intensities which increases the load capacity. This is not investigated in this article since it is not a cost effective way to increase the load capacity. Also, a stronger magnet results in an increase of the optimal width of the rings in order to prevent complete magnetic saturation. Increasing the magnetic saturation of the ferromagnetic material does exactly the opposite, namely resulting in a smaller optimal width. This comes from the fact that less material is needed to prevent saturation. Thus, choosing materials with better magnetic properties for the rings can increase the load capacity of the described ring magnet even more. However, using different ferromagnetic materials than steel could increase the costs, which makes the increase in load capacity by adding a ferromagnetic material less cost effective. These and many other possible improvements are not discussed in this article since the goal was to increase the load capacity of a ferrofluid bearing in a cheap and easy manner.

5. Conclusion

The experiments show that the model is in good accordance for the bearing with and without the ferromagnetic rings.

Overestimation of the load capacity is probably caused by capillary effects, an overestimation of the amount of effective ferrofluid and a mismatch between the modelled magnetic saturation and the actual material properties of the steel used in the test setup. The bearing furthermore shows excellent repeatability after an initial compression.

The addition of steel rings does not only increase the differences in field intensities, but also gives the opportunity to overcome the capillary effects and give rise to a second seal. Therefore, it can be concluded that the load capacity of the ferrofluid pocket bearing can be improved by the addition of steel rings up to a factor of 3–4, depending on the fly height and the dimensions of the steel.

Optimization shows that the maximum load capacity is reached if the thickness of the steel is equal to the thickness of the magnet and if the bearing is mounted on a ferromagnetic baseplate. Moreover, the optimal width depends on the magnetic saturation of the rings and the strength of the magnet. Ideally, the rings are on the verge of being completely saturated which optimally concentrates the magnetic field at the corners of the magnet. The optimal width of the steel for the ring magnet described in this report is approximately a third of the width of the magnet.

Acknowledgments

References

[1] Rosensweig R. Bearing arrangement with magnetic fluid defining bearing pads. 1971. 3 612 630.

[2] Rosensweig R. Magnetic fluid seals. 1971.

[3] Papell S. Low viscosity magnetic fluids obtained by the colloidal suspension of magnetic particles. 1965. 3 215 572.

[4] Rosensweig RE. Non-bursting ferrofluid seal. 2001. US6543782B1.

[5] Rosensweig RE. Ferrohydrodynamics. Dover Publications Inc; 2013.

[6] Rinaldi C, Chaves A, Elborai S, He X, Zahn M. Magnetic fluid rheology and flows. Curr Opin Colloid Interface Sci 2005;10:141–57. https://doi.org/10.1016/j.cocis.2005.07.004.

[7] Lampaert SGE, Spronck JW, van Ostayen RAJ. Load and stiffness of a planar ferrofluid pocket bearing. Proc Inst Mech Eng Part J J Eng Tribol 2017. https://doi.org/10.1177/1350650117739200. 135065011773920.

[8] Lampaert SGE, Fellinger BJ, Spronck JW, Ostayen RAJ Van. In-plane friction behaviour of a ferrofluid bearing. Precis Eng 2018https://doi.org/10.1016/j.precisioneng.2018.05.013.

[9] Lampaert SGE. Modelling and Design Principles of planar ferrofluid bearings. DSPE-Conference. 2016 2016.

[10] Cheng HC, Xu S, Liu Y, Levi S, Wu ST. Adaptive mechanical-wetting lens actuated by ferrofluids. Optic Commun 2011;284:2118–21. https://doi.org/10.1016/j.optcom.2010.12.073.

[11] Uhlmann E, Bayat N. High precision positioning with ferrofluids as an active medium. CIRP Ann - Manuf Technol 2006;55:415–8. https://doi.org/10.1016/S0007-8506(07)60448-X.

[12] Torres-Díaz I, Rinaldi C. Recent progress in ferrofluids research: novel applications of magnetically controllable and tunable fluids. Soft Matter 2014;10:8584–602. https://doi.org/10.1039/C4SM01308E.

[13] Sudo S, Takaki Y, Hashiguchi Y, Nishiyama H. Magnetic fluid devices for driving micro machines. JSME Int J Ser B 2005;48:464–70. https://doi.org/10.1299/jsmeb.48.464.

[14] Olaru R, Petrescu C, Hertanu R. A novel double-action actuator based on ferrofluid and permanent magnets. J Intell Mater Syst Struct 2012;23:1623–30. https://doi.org/10.1177/1045389X12449916.

[15] Liu Q, Alazemi SF, Daqaq MF, Li G. A ferrofluid based energy harvester: computational modeling, analysis, and experimental validation. J Magn Magn Mater 2018;449:105–18. https://doi.org/10.1016/j.jmmm.2017.09.064.

[16] Jayhooni SMH, Assadsangabi B, Takahata K. A stepping micromotor based on ferrofluid bearing for side-viewing microendoscope applications. Sensors Actuators, A Phys 2018;269:258–68. https://doi.org/10.1016/j.sna.2017.11.020.

[17] Mitamura Y, Takahashi S, Amari S, Okamoto E, Murabayashi S, Nishimura I. A magnetic fluid seal for rotary blood pumps: effects of seal structure on long-term performance in liquid. J Artif Organs 2011. https://doi.org/10.1007/s10047-010-0526-8.

[18] Ravaud R, Lemarquand G, Lemarquand V. Mechanical properties of ferrofluid applications: centering effect and capacity of a seal. Tribol Int 2010. https://doi.org/10.1016/j.triboint.2009.04.050.

[19] Yang R, Hou H, Wang Y, Fu L. Sensors and Actuators B : Chemical Micro-magnetofluidics in microfluidic systems : A review vol. 224. 2016. p. 1–15.

[20] Potma OGR. To. Designs for rotary shaft fluid seals in an aqueous environment

using ferroflui vol. 98. 2017.

[21] Urreta H, Aguirre G, Kuzhir P, Lopez de Lacalle LN. Seals based on magnetic fluids for high precision spindles of machine tools. Int J Precis Eng Manuf 2018. https://doi.org/10.1007/s12541-018-0060-9.

[22] Lampaert SGE, Spronck JW, van Ostayen RAJ, Café M. (2 + 4) DOF precision motion stage with ferrofluid bearings department of precision and microsystems engineering delft university of technology. 5–8. 2014.

[23] Café M. Nanometer precision six degrees of freedom planar motion stage with ferrofluid bearings. Technical University Delft; 2014.

[24] Lampaert SGE. Planar ferrofluid bearings modelling and design principles. Technical University Delft; 2015.

[25] Lampaert SGE, Spronck JW, van Ostayen RAJ. Hydrostatic bearing with MR texturing. B abstr 16th ger ferrofluid work. 2017. p. 94–5.

[26] Lampaert SGE, Spronck JW, van Ostayen RAJ. Load & stiffness of a planar ferrofluid pocket bearing S.G.E. 17th nord symp Tribol 2016. https://doi.org/10.1017/CBO9781107415324.004.

[27] Lampaert SGE, Spronck JW, van Ostayen RAJ. Virtual textured hybrid bearings. 44th Leeds-Lyon Symp. Tribol 2017;30:84.

[28] Millet G, Hubert A. Design of a 3 DOF displacement stage based on ferrofluids. Actuators 2006;06:656–9.

[29] Alvarez-Aguirre A, Mok G, HosseinNia SH, Spronck J. Performance improvement of optical mouse sensors: application in a precision planar stage. 2016 int conf manip autom robot small scales, MARSS. 2016 2016. https://doi.org/10.1109/MARSS.2016.7561698.

[30] Mok G. The design of a planar precision stage using cost effective optical mouse sensors. Technical University Delft; 2015.

[31] Lampaert SGE, Spronck JW, van Ostayen RAJ. Friction and trail formation of a planar ferrofluid bearing. Leeds-Lyon Symp. 2016. p. 4. 2016.

[32] Lampaert SGE, Spronck JW, van Ostayen RAJ, Habib H. Planar Positioning Stage with a PSD sensor and ferrofluid bearings. DSPE-Conference 2016:57–61. 2016.

[33] Van Veen S. Planar ferrofluid bearings for pecision stages. Technical University Delft; 2013.

[34] Olaru R, Petrescu C, Arcire A. Maximizing the magnetic force generated by an actuator with non-magnetic body in a ferrofluid pre-magnetized by permanent magnets. Int Rev Electr Eng 2013;8:904–11.

[35] Arcire A, Olaru R, Petrescu C. Study of the influence of ferromagnetic material on the characteristics of an actuator based on ferrofluid and permanent magnets. EPE 2012 - Proc 2012 Int Conf Expo Electr Power Eng 2012. p. 776–80. https://doi.org/10.1109/ICEPE.2012.6463838.

[36] Andersson L. Fillet away your electromagnetic field singularities. 2014.

Overview of bearings

A bearing or guidance system can be described as: a mechanism to accommodate for the specific displacement of an object in an accurate, precise and safe manner, by constraining possible motion in the other directions. Ideally, the bearing is infinitely compliant in the targeted directions of motion, also called the (independent) degrees of freedom, and infinitely stiff in all the other constrained directions.

The most efficient way to constrain a bodies motion is to constrain only the minimum number of independent degrees of freedom. Such a system is called exactly constrained. The resulting motion freedom in the other directions is called: degrees of freedom (DOF). A system is over-constrained when there are redundant constraints present in the system. Over-constraining can serve a specific purpose, for example to increase the load capacity and stiffness, however an over-constrained system is more sensitive to for example fabrication errors and thermal loads [42].

Table I-1 shows a couple of "daily life" examples of mechanisms categorized according to their DOF. For example, a 2 DOF system that consists of two translations can be used for positioning a sample under the microscope. In contrast, the end effector of a SCARA robot moves in the same plane, but uses 2 rotational joints to accommodate for the displacement [8]. Both systems have the capability of planar positioning, but the overall performance of the systems will be different due to the design choices made by the engineer.

Table I-1: "Daily-life" mechanism with their degrees of freedom.

Number of DOF	DOF	Application
1 DOF	x	Inkjet printer, sliding door, speaker coil, drawer
	ϕ	Bicycle hub, door hinge, scissors, laptop hinge
2 DOF	x, y	Microscope
	θ, ϕ	Drive train car
2+ DOF	x, y, ψ	Microscope stage
	x, y, z	3D printer
	θ, ϕ, ψ	Off road vehicle (Spherical/Heim joint)
	x, y, z, θ, ϕ, ψ	(Airplane) simulator

Of the many design options available for further research, there is chosen to focus on the interface/connection between the moving and stationary part of a bearing. One possible categorization for the different interfaces, based on basic working principles, is showed below. The subdivision of the contactless interface is based on the physical cause of the electromagnetic effect, either a specific type of Reluctance force (types 1-4) or Lorentz force (5-8) [1]. Multiple stages and mechanisms developed at the TU Delft are included in the categorization.

Each branch of the categorization presented below will be discussed in more detail in the next sections, in order to give a brief overview of the advantages and disadvantages of the different bearing types. **Only the expanding solid contact will not be further elaborated since no information was found on this topic.**

I-1 Solid: rolling contacts

The earliest forms of rolling contact bearings can be traced back to classical civilizations such as the Celts, Chinese and Greeks. However, some of the most impressive examples of the development of ball and roller bearings are found among the Romans, in particular the Lake Nemi findings at the end of the 19th century and begin of the 20th. Among the 3 shipwrecks, dated around 40AD, the remains of trunnion-mounted bronze balls were found, resembling ball thrust bearings, and wooden rollers within wooden rings, today known as taper roller thrust bearings, see figure I-1 [9].

The earliest known evidence of thinking in terms of degrees of freedom for (mechanical) systems was probably written by Leonardo Da Vinci in Codex Matrix I around 1500AD: "three balls under the spindle are better than four, because three balls are by necessity certainly always touched, while using four there would be a danger that one of them is left untouched" [9]. Moreover, he noticed that the individual parts of the ball bearing need to be able to move freely in order to reduce the friction significantly, otherwise the friction can even increase. Figure I-2 shows a drawing made by Da Vinci in which modern day ball bearings can be recognized.

Interface between stationary and moving part
```
├── Solid
│     ├── Rolling
│     ├── Sliding
│     ├── Expanding
│     └── Compliance      [3] [10] [11] [12] [38] [44]
├── Fluid
│     ├── Liquid
│     │     └── Ferrofluid/Magnetic Fluid  [12] [45] [46]
│     └── Gas      [16][21]
├── Contactless
│     └── (Electro) Magnetic effects [1]
│           ├── Reluctance force (Types 1-4) [31]
│           └── Lorentz force (Types 5-8)
└── Hybrid (Examples:)
      ├── Air Foil + Magnetic
      ├── Spiral Groove + Magnetic
      ├── Dual Stage : Air Bearing + Compliance [20]
      └── Spiral Groove + External pressure
```

Since then, different types of rolling contact bearings (table I-2) have been developed for a variety of applications, each with its own performance and characteristics. For example, a disadvantage of a linear precision guide is the limited stroke length. In comparison, recirculating ball bearings makes "infinite" stroke lengths possible, however the recirculation of the balls introduces small vibrations into the system [43]. The amplitude of the impulses caused by the collision of the balls with the rail, can be reduced by using a lubricant with a higher viscosity, but this again will lead to more viscous heating [35]. The Eigenmodes of the bearing are not influenced by the recirculating elements, only by the stiffness [17] [34].
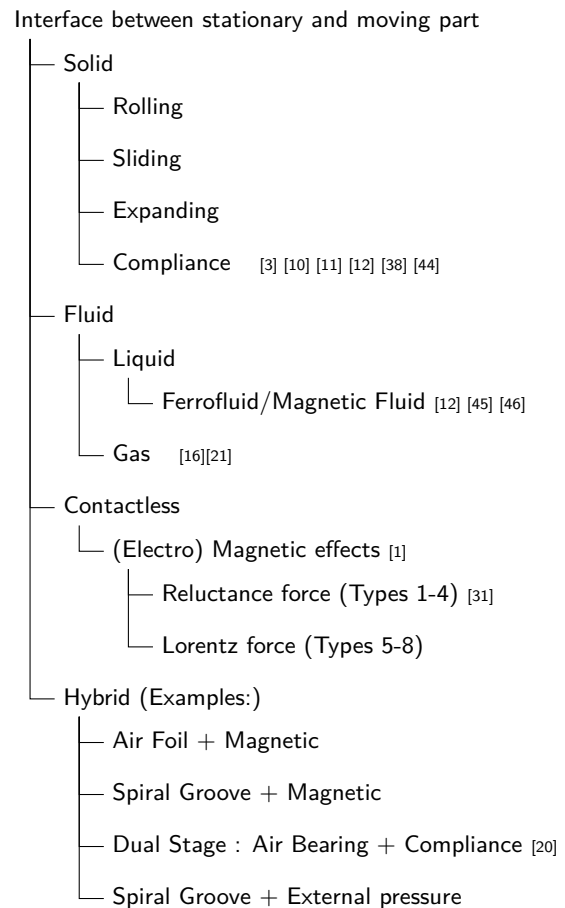
Figure I-1: Part of the Lake Nemi Findings: the remains of trunnion mounted bronze balls [7].
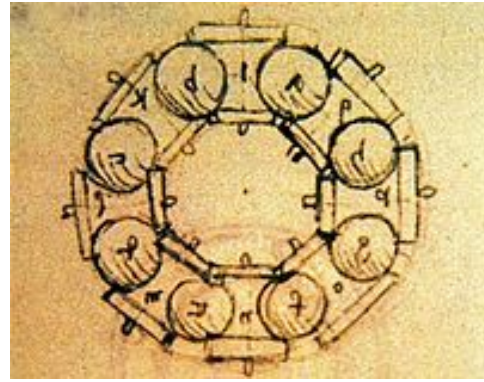

Figure I-2: Drawing by Leonardo Da Vinci [27].

Other characteristics of rolling contact bearings are: stick-slip, possible backlash and friction. The amplitude of stick-slip can be reduced by either increasing the damping or stiffness. Stick-slip can also be completely suppressed by applying a high enough preload. The operating temperature of rolling contact bearings is most of the time limited by the type of lubricant used, due to frictional heating. Different bearing designs, for example using ceramic balls, other lubricants or decreasing the total friction, allow for higher operating temperatures [43]. In general, the advantages and disadvantages for rolling contacts are: [42] [43]

Advantages

+ Extensive knowledge base (through years of application and development)
+ High stiffness
+ High load capacitiy
+ Safe when maximum force is exceeded (plastic deformation if hot hardened)
+ Easy to buy ("off the shelf") and therefore relatively cheap

Disadvantages

- Stick-slip and Microslip
- Backlash (without preload)
- Lubrication needed
- Overconstrained
- Spin and creep
- Friction/Mechanical contact:
* Heat development
* Wear and tear
* Vibrations and sound development

Table I-2: An overview of different bearing types [43].

Rolling Bearings	**Sliding Bearings**	**Fluid Bearings**	**Magnetic Bearings**
Ball Bearings	Plastic bearings	Yournal bearings	Active magnetic bearings
Roller Bearings	Metallic bearings	Michell bearings	Passive magnetic bearings
Deep groove ball	Jewel bearings	EP bearings	
Angular contact	Injection molded	Foil bearings	**Hybrid Bearings**
Self aligning	Standard bushings	Plain	Foil − magnetic
Cylindrical	Machining	Spiral groove	S.g. − magnetic
Tapered	PA,POM UHMWPE	Lemon bore	S.g. − E.P.
Needle	Solid, Porous	Gas bearings	
Rotary	Bronze, leaded bronze	Oil bearings	**Flexures**
Linear	Rotary	Magnetic fluid bearings	Leaf spring
	Linear		Monolithic

I-2 Solid: sliding contact

Sliding contact bearings, sometimes called plain journal bearings, are the most basic bearings available. Table I-2 shows different variations. The solid contact between the sliding surfaces results in wear and tear over time and faulty material choices can even lead to adhesion between the surfaces. Therefore, these cost-effective bearings are commonly used in less critical applications, since wear results in radial play.

Solid contact bearings are implemented in an ingenious way in the Maeslantkering in Rotterdam. Multiple specially developed solid polymer pads were placed inside the large ball and socket joint, which lifted the total weight of the structure, namely $350MN$. The stress on the pads succeeded the yield strength of the polymers, which resulted that the polymer pads acted as fluid bearings [41]. In general, the advantages and disadvantages of sliding contact bearings are: [43].

Advantages
+ Simple
+ Cheap

Disadvantages
- Friction (heating)
- Wear
- Radial play
- Adhesive effects
- Pressure and velocity dependency (PV value)

I-3 Solid: compliance

An example of a high precision, repeatable, compact and monolithic compliant mechanism can be found in the Zenith DEFY LAB watch, which is at the moment of writing the most accurate watch in the world, with only a variation of $\pm 0.5s$ over 48 hours (figure I-3). The compliant timekeeping mechanism is made out of a piece of monocrystalline silicon coated with a layer of silicon oxide. The process of Deep Reactive Ion Etching (or DRIE) is used to produce the part. The entire watch consist only of 148 parts which is a significant decrease in total components [14].

Figure I-3: The monolithic time-keeping mechanism found in the watch by Zenith DEFY LAB [14].
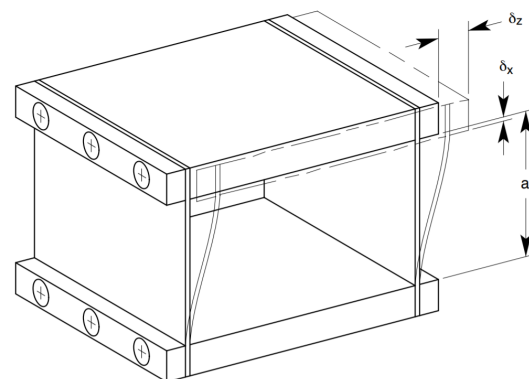

Figure I-4: Parallel flexure mechanism for a linear degree of freedom system [13].

Besides the complex timekeeping mechanism, compliant mechanisms can be as simple as two parallel mounted flexures, resulting in a linear degree of freedom system (figure I-4). (Note that this particular system is overconstrained in the vertical direction.) A horizontal displacement δ_z results in a parasitic motion in the vertical direction δ_x. One solution is to mirror the flexures such that the parasitic motion will disappear due to symmetry. However, this means overconstraining the system even more, which also increases the stiffness in the degree of freedom [13]. Due to the parasitic motion and loss of stiffness, most compliant mechanism are limited to a small range of motion. In general, the advantages and disadvantages of compliant mechanism are: [6] [11] [15] [42].

Advantages
+ Almost no friction, play or hysteresis
+ Easy to fabricate and assemble and therefore cheap
+ No maintenance needed
+ No contamination possible
+ No lubrication (clean operation, medical semicon or vacuum)
+ Can be used on very small scale (monolithic fabrication)
+ High resolution possible
+ Zero stiffness designs possible

Disadvantages
- Nonlinear behaviour
- Buckling
- Generally small range of motion
* Large stroke flexure mechanism do exist, but have a small workspace to footprint area [11]

I-4 Fluid: gas bearings

In comparison to the rolling and sliding contact bearings, fluid bearings have the advantage that the running surfaces do not make physical contact. The surfaces are separated by a fluid film, which can be either a liquid or a gas depending on the application. There are two distinct types of gas bearings, namely aerodynamic and aerostatic. Aerodynamic bearings rely on the (rotational) velocity of the surfaces to create a stable fluid film, whereas aerostatic bearings rely on the injection of an externally pressurized supply of gas. Gas bearings are mainly found in high precision and high speed application due to the low viscosity, low heat development and low (or absent) friction, see table I-3. The advantages and disadvantages of gas bearings are: [43].

Advantages
+ Air does not contaminate environment, so no seals required
+ Low friction
+ High speed
+ No mechanical contact (no wear)
+ High precision: Absence of friction results in accurate motion control
+ High operating temperatures (gas lubrication)
+ No stick-slip
+ No backlash

Disadvantages
- Compressibility: behaviour gets more complicated
- Aerodynamic instability (pneumatic hammer)
- Supply pressure
- Small load capacity (w.r.t. liquid or ball bearings)
- High flow rate required
- Flow rate vs. film thickness. Relatively small film thickness is required
- Anti seizure + corrosion
- Start-up phase for aerodynamic bearings
- Minor damping due to compressibility

I-5 Fluid: liquid bearings

Like gas bearings, liquid bearings can be hydrodynamic or hydrostatic. Advantages such as the high load capacity and stiffness make liquid bearings suitable for high precision production

Table I-3: Friction coefficients (μ) for different bearing types [43].

Slide bearing, hydrodynamic	0.003...0.04
Slide bearing, sinter bronze, oil lubricated	0.04...0.07
Slide bearings, solid bronze, grease lub	0.07...0.12
Polymer slide bearing, polyamide, dry	0.2...0.3
Polymer bearing, composite, dry	0.05...0.15
Ball bearings	0.001...0.0015
Roller bearings	0.0018
Needle bearings	0.0045
Air bearings, pressurized	0.0
Hydrostatic bearings	0.001...0.002 (viscous shearing)

machines. However, a big disadvantage is that the load capacity of externally pressurized bearings (liquid and gas) is dependent on the reliability of the source (pump). In contrast, the biggest advantage of hydro/aerodynamic bearings is that they are passive, meaning no external source or control is needed. However, full film lubrication is not established at low (rotational) velocities, resulting in wear in the start-up phase. Other advantages and disadvantages are: [43].

Advantages
+ Highest bearing stiffness and smoothness
+ No play
+ Only viscous friction
+ No stick-slip
+ No backlash
+ Better damping (relative to air bearings)
+ No mechanical contact (no wear)

Disadvantages
- Sealing needed
- Start-up phase for hydrodynamic bearings
- Thermal heating for high speed/shear rate applications
- Corrosion

I-6   Contactless: reluctance and Lorentz force (types 1-8)

According to Earnshaw's Theorem it is impossible for a object to be suspended in a stable equilibrium by only the means of magnetic or electrostatic forces. All passive magnetic bearings are at least unstable in one direction. Stable equilibrium can be obtained by actively controlling the magnetic field (active magnetic bearings). Mechanical components could also be added to the system to reach stability, an example can be adding a bearing for axial stabilization of the passive magnetic bearing. However, the added mechanical contact reduces the advantage of contactless suspension [26].

Contactless suspension can be subdivided into electromagnetic effects caused by Reluctance forces (types 1-4) and Lorentz forces (types 5-8) [1]. In general the advantages and disadvantages of contactless bearing systems are: [43].

Advantages
+ No mechanical contact (no wear)
+ Can be used in vacuum
+ High operating temperatures possible
+ High speed applications

Disadvantages
- High frequency control system needed
- Complex
- Expensive
- Load capacity similar to air bearings

I-7   Hybrid

Different bearings can be combined into a single hybrid bearing, in order to take advantage of the different bearing characteristics. An example of a hybrid bearing is the combination of an externally pressured bearing (aerotatic) and a spiral groove bearing (aerodynamic). The bearings complement each other, at low operating speeds the load capacity is obtained by the aerostatic bearing (active), while at high speeds the aerodynamic bearing generates the load capacity (passive).

A general overview of advantages and disadvantages cannot be given since many different combinations are possible with each their own characteristics. Moreover, the goal of designing hybrid bearings is to mitigate the biggest disadvantages of one bearing by implementing the other bearing. Some examples of hybrid bearings are:

(1) Magnetic fluid + hydrodynamic bearing: hydrodynamically lubricated bearings need sealing to prevent contamination. The advantage of using magnetic fluid is that the fluid can be held in place by a permanent magnet or (electro)magnet, when designed properly. (2) Magnetic + aerodynamic bearing: The magnetic bearing provides stability at low speeds, since full film lubrication is not yet established by the hydrodynamic bearing. At high frequencies the active magnetic bearing can become unstable, at which point the aerodynamic bearing is stable [43].

I-8   Conclusion

This chapter presented a categorization for bearings based on the interface between the moving and stationary part: solid, fluid, contactless and hybrids. Each type of bearing has its own characteristics, performance and limitations. The specific application therefore determines which bearings are the most suitable. Take for example a traditional microscopy stage with only planar degrees of freedom (x,y,optional: ϕ). For this application, rolling or sliding contact bearings can be used, but also compliant mechanism [6] [11] [44], air bearing [21] [47] [48] or recent developed ferrofluid stages [5] [12] [30] [45]. However when 6DOF positioning is needed, traditional rolling contact systems become bulky, since the DOF are obtained by stacking multiple bearings. Then using magnetic levitations [31] might be an option, but note that this system is much more complex, computational expensive and costly. It can be concluded that currently the state-of-the-art is the single mover, found in the ferrofluid stages or air bearings.

The wide variety of bearings available gives the engineer a vast amount of design options. The application determines which bearings types are applicable. Examples of important requirements when designing are: cost, system dimensions, stiffness, load capacity and accuracy. At last, the only thing that remains is the challenge for the engineer to find the "best" suitable bearing for their specific application according to their expert opinion.

Until now only the bearing function is considered and the propulsion function is neglected. However the propulsion can be an integrated part of the single mover bearing when using magnetic or fluid bearings [47]. Screw spindles or power screws are an example of combining both functions in a more "traditional" type of rolling or sliding contact bearing.

Bibliography

[1]   Hannes Bleuler. "A Survey of Magnetic Levitation and Magnetic Bearing Types." In: *JSME international journal. Ser. 3, Vibration, control engineering, engineering for industry* 35.3 (1992), pp. 335–342. ISSN: 0914-8825. DOI: 10.1299/jsmec1988.35.335. URL: http://joi.jlc.jst.go.jp/JST.Journalarchive/jsmec1988/35.335?from=CrossRef.

[2]   A.S.T. Boots et al. "Increasing the load capacity of planar ferrofluid bearings by the addition of ferromagnetic material". In: *Tribology International* 129 (2019). ISSN: 0301679X. DOI: 10.1016/j.triboint.2018.07.048.

[3]   R. Bruinen. "sign and analysis of a flexure based 3-DOF micro positioner". MSc Thesis. Technical University Delft, 2011.

[4]   COMSOL. *COMSOL Multiphysics.* 2018. URL: https://www.comsol.com/documentation.

[5]   Max; Café. "Nanometer precision Six Degrees of Freedom Planar Motion Stage with Ferrofluid Bearings". MSc thesis. 2014.

[6]   Kee Bong Choi and Doo Hyeong Kim. "Monolithic parallel linear compliant mechanism for two axes ultraprecision linear motion". In: *Review of Scientific Instruments* 77.6 (2006). ISSN: 00346748. DOI: 10.1063/1.2207368.

[7]   *Classical Wisdom Daily.* 2017. URL: http://classicalwisdom.com/caligulas-contribution/.

[8]   M. Taylan Das and L. Canan Dülger. "Mathematical modelling, simulation and experimental verification of a scara robot". In: *Simulation Modelling Practice and Theory* 13.3 (2005), pp. 257–271. ISSN: 1569190X. DOI: 10.1016/j.simpat.2004.11.004.

[9]   Duncan Dowson and Bernard J. Hamrock. "History of ball bearings". In: *NASA Technical MEmorandum* February.81689 (1981).

[10]   Gerard Dunning. "Design of a zero stiffness six degrees of freedom compliant precision stage". MSc Thesis. Technical University Delft, 2011.

[11]   K.G.P. Folkersma et al. "A 2-DOF Large Stroke Flexure Based Positioning Mechanism". In: *Volume 4: 36th Mechanisms and Robotics Conference, Parts A and B* December 2015 (2012), p. 221. DOI: 10.1115/DETC2012-70377. URL: http://proceedings.asmedigitalcollection.asme.org/proceeding.aspx?doi=10.1115/DETC2012-70377.

[12]   Haris Habib. "Design of a three Degrees of Freedom planar precision stage using a single Position Sensitive Detector". MSc Thesis. Technical University Delft, 2015.

[13]   Layton C. Hale. "Principles and techniques for desiging precision machines ." In: *Dissertation* (1999).

[14]   Hodinkee. *Introducing: The Zenith Defy Lab, With A Revolutionary New Oscillator System (Exclusive Live Photos).* URL: https://www.hodinkee.com/articles/zenith-defy-lab-oscillator-introducing (visited on 11/15/2017).

[15] J.B. Hopkins. "On the use of Freedom Constraint Topologies". In: *Mikroniek* 5 (2015).

[16] X. Huang. "Actuation System Design for a 3 DoF ContactlessWafer Stage". MSc Thesis. Technical University Delft, 2016.

[17] Jui Pin Hung. "Load effect on the vibration characteristics of a stage with rolling guides". In: *Journal of Mechanical Science and Technology* 23.1 (2009), pp. 89–99. DOI: 10.1007/s12206-008-0925-4.

[18] Zou Jibin and Lu Yongping. "Numerical Calculations for Ferrofluid Seals". In: *IEEE Transactions on Magnetics* 28.6 (1992), pp. 3367–3371. ISSN: 19410069. DOI: 10.1109/20.179812.

[19] J.P. Joule. "On the Effects of Magnetism upon the Dimensions of Iron and Steel Bars". In: *The London, Edinburgh, and Dublin Philosophical Magazine and Journal of Science* 30.Third Series: 76–87 (), pp. 225–241.

[20] B.J. Joziasse. "Nanometer precision scanning dual stage with reduced Joule heating in the fine stage actuator". MSc Thesis. Technical University Delft, 2017.

[21] J.J.M. Karregat. "Design of an Air Actuator with Deformable Geometry for planar actuation of large substrates J.J.M." MSc Thesis. Technical University Delft, 2014.

[22] Pijush K. Kundu, Ira M. Cohen, and David R. Dowling. "Chapter 11 – Instability". In: *Fluid Mechanics*. 2016. ISBN: 9780124059351. DOI: 10.1016/B978-0-12-405935-1.00011-3.

[23] S.G.E. Lampaert. "Planar Ferrofluid Bearings Modelling and Design Principles". MSc Thesis. Technical University Delft, 2015.

[24] S.G.E. Lampaert, J.W. Spronck, and R.A.J. van Ostayen. "Load and stiffness of a planar ferrofluid pocket bearing". In: *Proceedings of the Institution of Mechanical Engineers, Part J: Journal of Engineering Tribology* (2017), p. 135065011773920. ISSN: 1350-6501. DOI: 10.1177/1350650117739200. URL: http://journals.sagepub.com/doi/10.1177/1350650117739200.

[25] S.G.E. Lampaert et al. "In-plane friction behaviour of a ferrofluid bearing". In: *Precision Engineering* October (2017). ISSN: 01416359. DOI: 10.1016/j.precisioneng.2018.05.013.

[26] Torbjörn a. Lembke. "Design and Analysis of a Novel Low Loss Homopolar Electrodynamic Bearing". PhD thesis. KTH Electrical Engineering, 2005, pp. 1–24. ISBN: 9171780327.

[27] *Leonardo da Vinci's Ball Bearing*. 2017. URL: http://www.leonardodavincisinventions.com/mechanical-inventions/leonardo-da-vinci-ball-bearing/.

[28] MathWorks. *Box plot - MATLAB boxplot - MathWorks Benelux*. URL: https://nl.mathworks.com/help/stats/boxplot.html (visited on 07/16/2018).

[29] MathWorks. *MATLAB*. Natick, Massachusetts. URL: https://nl.mathworks.com/help/?s{_}tid=hp{_}ff{_}l{_}doc.

[30] Gihin Mok. "The design of a planar precision stage using cost effective optical mouse sensors". MSc Thesis. Technical University Delft, 2015, p. 107.

[31] A.M. Mulder. "Design of a 6-DoF Miniature Maglev Positioning Stage for Application in Haptic Micromanipulation". MSc Thesis. Technical University Delft, 2016, pp. 5–7.

[32] Joseph L. Neuringer and Ronald E. Rosensweig. "Ferrohydrodynamics". In: *Physics of Fluids* 7.12 (1964), pp. 1927–1937. ISSN: 10706631. DOI: 10.1063/1.1711103.

[33] Stefan Odenbach. *Colloidal magnetic fluids: basics, development and application of ferrofluids*. 763. 2009, p. 430. ISBN: 9783540853862\r3540853863. DOI: 10.1007/978-3-540-85387-9Lecture.

[34] Hiroyuki Ohta and Eiji Hayashi. "Vibration of linear guideway type recirculating linear ball bearings". In: *Journal of Sound and Vibration* 235.5 (2000), pp. 847–861. ISSN: 0022460X. DOI: 10.1006/jsvi.2000.2950.

[35]   Hiroyuki Ohta et al. "Effects of Grease Types on Vibration and Acoustic Emission of De-
        fective Linear-Guideway Type Recirculating Ball Bearings". In: *Journal of Tribology* 133.2
        (2011), p. 021102. ISSN: 07424787. DOI: 10.1115/1.4003302. URL: http://tribology.
        asmedigitalcollection.asme.org/article.aspx?articleid=1468674.

[36]   R.E. Rosensweig. "Magnetic fluids". In: *Annual Review of Fluid Mechanics* 19 (1987), pp. 437–
        461. ISSN: 0038-5670. DOI: 10.1146/annurev.fl.19.010187.002253. URL: https://doi.org/
        10.1146/annurev.fl.19.010187.002253.

[37]   Ronald E. R.E. Rosensweig. *Ferrohydrodynamics*. Dover Publications Inc, 2013, p. 368. ISBN:
        0486783006/9780486783000.

[38]   A.G.P.I. Scheerhoorn. "Design of a linear guide for an optical fiber used in pressure sensitive
        spectroscopy using a compliant rolling mechanism". MSc Thesis. Technical University Delft,
        2016.

[39]   C. Scherer and A.M. Figueiredo Neto. "Ferrofluids: Properties and Applications". In: *Brazilian
        Journal of Physics* 35.3A (2005), pp. 718–727. ISSN: 1678-4448. DOI: http://dx.doi.org/10.
        1590/S0103-97332005000400018.

[40]   M. I. Shliomis. "Magnetic Fluids". In: *Sov. Phys. Usp.* 17.March 1974 (1974), p. 153.

[41]   S K Sinha and B J Briscoe. *Polymer Tribology*. World Scientific, 2009.

[42]   H Soemers. *Design Principles for precision mechanisms*. T-Pointprint, 2011. ISBN: 978-90-365-
        3103-0.

[43]   A Van Beek. *Advanced engineering design: lifetime performance and reliability*. fifth. 2012. ISBN:
        978-90-810406-1-7. URL: http://www.tribology-abc.com.

[44]   J. Van Koppen. "Mechatronic design of a 2 DOF scan stage inside a Scanning Electron Micro-
        scope". MSc Thesis. Technical University Delft, 2013.

[45]   Len Van Moorsel. "A planar precision stage using a single image sensor". MSc Thesis. Technical
        University Delft, 2017.

[46]   Simon Van Veen. "Planar Ferrofluid Bearings for Pecision Stages (MSc thesis)". MSc Thesis.
        Technical University Delft, 2013, p. 121.

[47]   Phuc Hong Vuong. "Air-Based Contactless Actuation System for Thin Substrates". PhD thesis.
        Technical University Delft, 2016. ISBN: 9789461867148.

[48]   Jasper Wesselingh. "Contactless positioning using an active air film". PhD thesis. Technical
        University Delft, 2011.